POLITECNICO DI MILANO

DIPARTIMENTO DI MATEMATICA "F. BRIOSCHI"

DOTTORATO DI RICERCA IN "METODI E MODELLI MATEMATICI PER L'INGEGNERIA"

Mathematical and numerical modelling of the evolution of mixtures of sand in aeolian dunes

Ph.D. candidate
Matteo Pischiutta
matr. 738627

Advisors:
    Prof. Luca Formaggia
    Prof. Fabio Nobile
Tutor:
    Prof. Luca Formaggia
Supervisor of the Doctoral Program:
    Prof. Paolo Biscari

2012 – XXIV CICLO

Abstract

The morphodynamic of desert sand dunes is due to two distinct physical mechanisms: the effect of the wind blowing on the sand surface which produces a flux of jumping sand grains said "in saltation", and the spontaneous generation of avalanches if the slope of the sand surface is steeper than the angle of repose. Given the long time scale to observe effective movement of a dune and the difficult reproducibility in wind tunnel, in the last decade mathematical modelling and numerical simulation of sand dune evolution have become an important subject of research. In the existing literature, the modelling is often based on a conservation equation for the mass of sand formulated by balancing the temporal variation of sand surface elevation with the divergence of the saltation and avalanches sand fluxes. The saltation flux is hence written in term of the shear stress exerted by the wind on the sand surface, whereas the avalanche flux depends on the local slope of the sand surface.

In this Ph.D. thesis we are interested in building a model for dune evolution when the bulk sediment is a mixture of sands with different characteristics. In particular, we consider sands which can be distinguished only by their appearance, but which have the same physical characteristics such as diameter and density. Hence we will refer to "marked" and "clean" sediments. The interest in the evolution of the concentration of marked sediment is motivated by the industrial problem of remote sensing for hydrocarbon microseepage. In particular situations, the light hydrocarbons can in fact seep through the seal rock of the reservoir, and hence rise to the Earth surface. This hydrocarbon microseepage can induce geochemical and geophysical alterations in the sedimentary column, and the superficial footprint of these anomalies can be further detected with remote sensing techniques. Supposing that the microseepage induced alteration is adsorbed at the sand grain level, in deserts with moving dunes the superficial footprint of the reservoir can be dispersed by the transport of sediments induced by the wind.

In this work, the derivation of the complete three dimensional model of the evolution of mixtures of sands in aeolian dunes is accomplished by first assuming that sediment exchange between sand surface and superficial transport fluxes (for both the saltation and the avalanche dynamics) is limited in a superficial layer of finite depth, called "active layer". On the one hand, this allows us to consider the substrate under the active layer as a zone where the concentration of marked sand is stored in depositional processes

and remains unvaried since this zone is not involved in superficial transport processes. On the other hand, the concentration of marked sand in the active layer depends on the local balance between the mass of marked sand entrained from the surface and the mass of marked sand deposited from the superficial fluxes.

Hence, the mathematical model for dune evolution has been completely reformulated by expressing the temporal variation of sand surface elevation in term of the balance between the entrainment and deposition rates due to saltation and avalanches, instead than using the divergence of the sand fluxes as usually made so far in the aeolian literature.

We hence provide the constitutive relationship for the new variables introduced in the system. The entrainment and deposition rates due to the saltation dynamics are derived from the model of impact rate available in the literature by introducing a probability of rebound of the impacting grain. For the avalanche mechanism, we assume that erosion occurs only if the slope exceeds the angle of repose, and introduce a probabilistic step length for avalanching grains which links the deposition rate to the upward entrainment rate. We also provide a possible characterization of the new parameters added to the system by fitting our model to experimental data existing in the literature.

Concerning the numerical simulation of the problem, at each time step we subsequently perform the update of the saltation and avalanche sub–model. For the saltation dynamic, we calculate the wind field on the sand surface with a computationally efficient analytical theory of logarithmic boundary layer perturbation. Hence the system of conservation laws with source terms which describes the mass and momentum conservation of marked and cleaned sand in the saltation layer is discretized with the conservative finite volume method, taking into account the source terms with an operator splitting technique. The results of sand dune evolution obtained with our formulation agrees well in term of dune shapes and velocities with those encountered in the literature. However, the new formulation offers the possibility for a differential evolution of sand dunes made up of a mixture of sands. Amongst the possible applications of our formulation, we can investigate the problem of dune collision from an original point of view. In fact, by assuming that one dune is made of marked sand, we can observe the evolution of the whole sedimentary structure during the collision.

In the case of evolution of two dimensional dunes, we also provide a simplified formulation where the entrainment rate is written in function of the shear stress exerted by the wind on the sand surface, while the deposition rate is linked to the upwind entrainment rate by assuming that the step length of a saltating grain is probabilistic with a given density function. Under some simple but physically based hypothesis, we show the mathematical equivalence of this formulation with a simplified model encountered

in the literature. Hence this new formulation constitutes a great simplification of the problem with limited drawbacks, and it allows us to approach some large scale problems with affordable computational costs. In particular, we couple the system with a model of generation of marked sand due to hydrocarbon microseepage, and simulate the dispersions of the superficial footprint of the reservoir for large temporal and spatial scales.

Acknowledgements

Contents

1

Introduction

Approximatively 30% of the Earth's land surface is formed by desert, arid lands with less than 250 mm of rainfall per year. According to this definition, the biggest desert of the world is ... the Antarctica. However, we are here interested in sand desert. Sand covers about 20% of Earth's deserts; the biggest sand deserts of the world are the Sahara (Fig.1.1) and the Arabian desert.
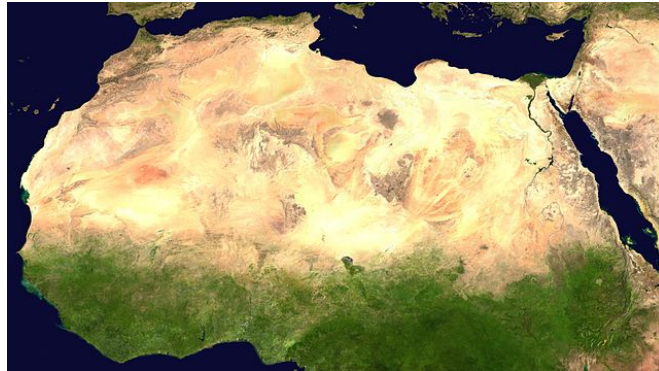
Figure 1.1: The biggest sand desert of the world: the Sahara.

In these regions the action of the wind mobilizes and transport the sand grains, generating sand dunes. The movement of sand dunes can produce some important troubles to human installations like cultivations, streets an even whole cities, see Fig.1.2.
Given the long time scale to observe effective movement of a dune and the difficult reproducibility in wind tunnel, in the last decade mathematical modelling and numerical simulation of sand dune evolution have become an important subject of research. In this Ph.D. thesis work we intend to contribute to the scientific community by formulating an original model for the evolution of sand dunes formed by a mixture of sands with different characteristics. In this Chapter we first outline the main features of sand transport and dune movement, then we describe the state of the art of the mathematical models of sand dune evolution, finally motivate our work and outline the arguments discussed in this work.
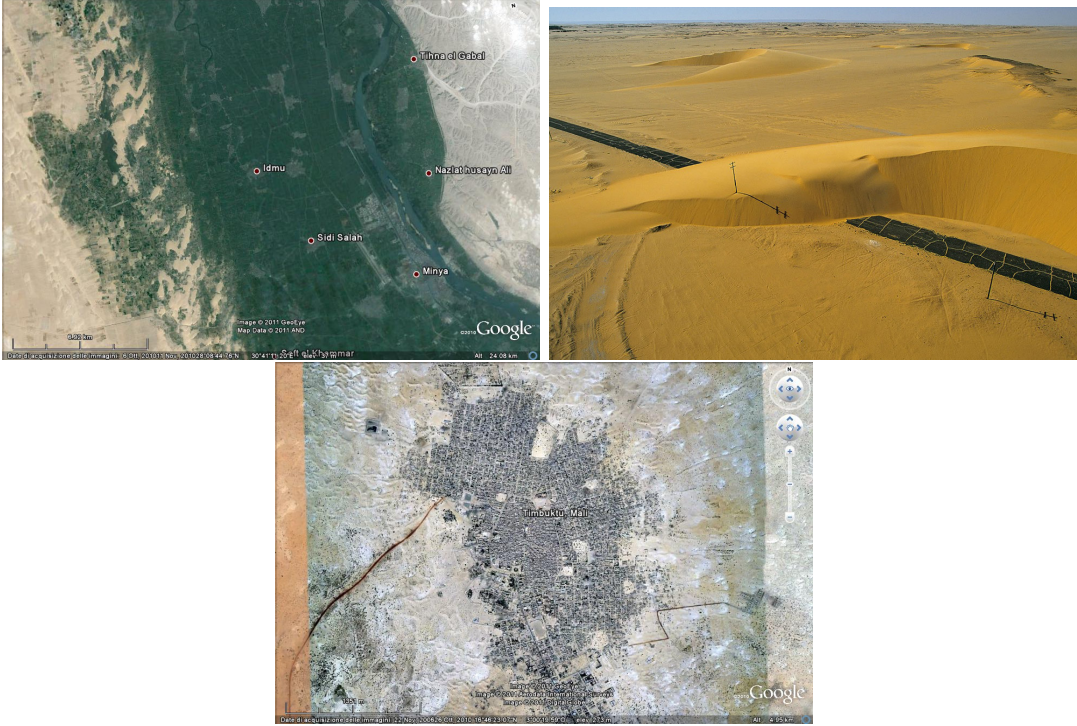
Figure 1.2: Sand dunes invading cultivations and streets in Egypt and surrounding Timbuctu in Mali.

1.1 Sand transport and dune movement

In this Section we present the main characteristics of sand dune movement and morphology. In particular we subdivide the Section into three main parts: in the first we analyse the modes of transport of sand, then in the second part we provide an accurate description of the threshold for entrainment of sand and in the last part we describe the main possible shapes of dunes.

1.1.1 Modes of transport of sand

Two principal parameters are mainly involved in sand transportation: the grain weight and the friction velocity. The grain weight could be assimilated to grain size (or diameter, d) if a constant sand density is assumed (e.g. a quartz crystal, SiO_2 has a density of $\rho_{sand} = 2650\,\mathrm{Kg/m^3}$). The friction velocity u_* is strictly related to the intensity of the wind and is defined as:

$$u_* = \sqrt{\frac{\tau}{\rho_{air}}}$$

where τ is shear stress at the ground surface; u_* has the dimension of velocity but it is actually a measure of shear stress.

Bagnold (1941) proposed three different modes of sand transport (see Fig.1.3):

Creep or bed load: sand grains roll or slide without loosing contact with the surface.

Saltation: sand grains move by a series of small jumps in the range $10^{-2} - 10^{-1}$ m. Saltation is due at first to the direct wind drag and secondly to the impact of other saltating grains.

Suspension: sand grains are lifted by the flow and cover large distances before regaining contact with the surface.
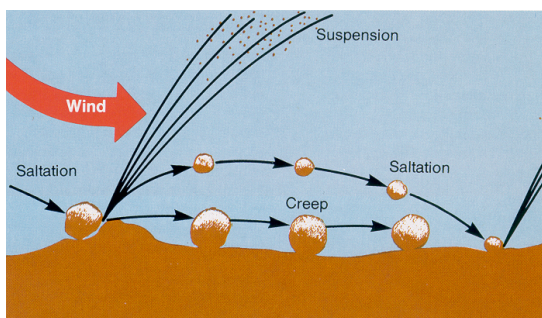
Figure 1.3: A schematic representation of the three different type of sand transport induced by the wind (creep, saltation and suspension).

A grain is maintained in suspension by a turbulent airflow when the vertical fluctuating velocity component of the flow (w') exceeds the settling velocity of the grain (w_f). A good estimate of w' is given by the friction velocity u_* (Pye & Tsoar, 1990) while w_f is modeled as the terminal velocity of a sphere falling in a viscous fluid by its own weight due to gravity (known as Stokes terminal velocity or Stokes settling velocity) and is given by:

$$w_f = \frac{\rho_{sand} g}{18 \mu_{air}} d^2$$

where ρ_{sand} is the mass density of the sand (kg/m^3), g is the gravitational acceleration (m/s^2), μ_{air} is the dynamic viscosity of air (Ns/m^2) and d is the grain diameter in m. Pure suspension transport happens when the grain settling velocity is very small respect to the friction velocity, *i.e.* when $w_f/u_* \ll 1$. On the contrary, creep transport and saltation happens when the vertical velocity components have no significant effect on grains trajectories; this occurs when $w_f/u_* \gg 1$. When the ratio w_f/u_* is near the value of 1, an intermediate transport type occurs named modified saltation (Hunt & Nalpanis, 1985; Nalpanis, 1985) *i.e.* sand grains develop random trajectories between saltation and suspension. In Fig.1.4 a subdivision of the different modes of sand transport is depicted as theoretically determined by Nalpanis (1985).

Typical wind storms are characterized by friction velocities in the range $0.18 \, \text{m/s} \leq u_* \leq 0.6 \, \text{m/s}$; with these velocities grains of $0.1 - 0.3$mm in diameter are subject to saltation generating sand dunes, grains smaller than $0.1 \, \text{mm}$ are subject to suspension and are carried for large distances, grains larger than $0.3 \, \text{mm}$ move principally by rolling and remain concentrated in residual sand sheets. So, the mechanism mainly involved
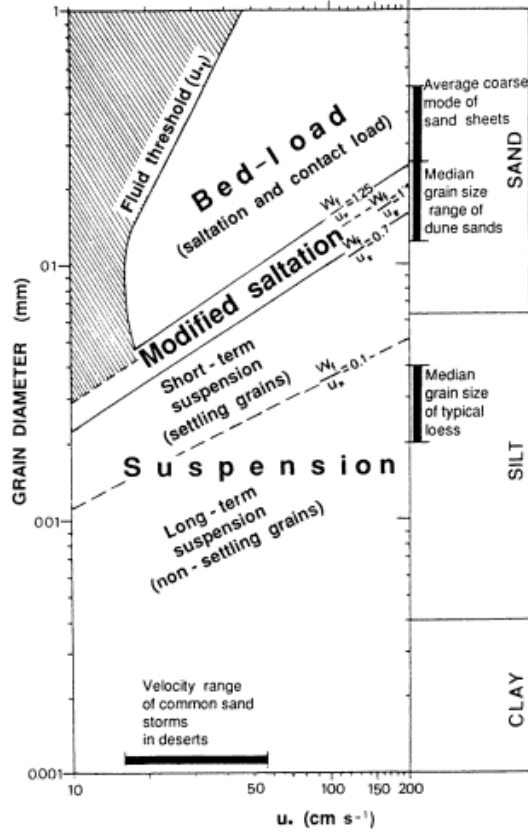
Figure 1.4: Modes of transport of quartz grains at different friction velocities u_* and grain diameter (Pye & Tsoar, 1990).

in dune generation and movement is the saltation transport; this is the mechanism principally investigated in this Ph.D. work.

1.1.2 The threshold for entrainment

The first description of sand saltation during wind transport was provided by Joly (1904) and Owens (1927). Bagnold (1936) and subsequently Chepil (1945) photographically demonstrated the characteristic trajectory of saltating grains. This phenomenon was extensively studied using wind tunnels, numerical models and field approaches (Bagnold, 1936, 1941; Owen, 1964; Anderson & Haff, 1988; Willetts & Rice, 1988; Jensen & Sørensen, 1986; Ungar & Haff, 1987; Werner & Haff, 1988). All these studies demonstrated that saltation is a complex phenomenon influenced by several factors, including grain size and wind velocity.

In detail, the phenomenon could be described by writing an equation for the balance of force over the grain. Wind flowing on a sand grain on an horizontal surface exerts two forces: a drag force F_d acting horizontally and a lift force F_l acting vertically in the

upwards direction. Opposed forces acting on the grain are the inertial force and the gravity force (F_g) which acts opposite to the lift force. To produce a sand movement the drag and lift forces on the grain must exceed the gravity. In detail, we could consider a surface covered by loose sands of uniform size: grains on the upper part of the surface are free to move upwards and at the same time are constrained in the horizontal direction by adjacent grains. The point of contact between adjacent grains behaves as a pivot around which rotational movement may take place (see Fig.1.5). The momentum balance equation could be written as:

$$F_d(d/2)\cos(\Phi) = (F_g - F_l)(d/2)\sin(\Phi)$$

where Φ is the angle at the center of grain gravity between the pivot and F_g. Expressing the aerodynamic forces using experimental relations, it is possible to find a critical surface shear stress τ_{ta} and a related critical friction velocity u_{*ta} above which some grains begin to move. For example Pye & Tsoar (1990) derived the following relations for the threshold shear stress:

$$\frac{\tau_{ta}}{(\rho_{sand} - \rho_{air})gd} = \frac{2}{3\beta}\left(\frac{\sin\Phi}{(\cos\Phi + c\sin\Phi)}\right) \qquad \text{and} \qquad u_{*ta} = \sqrt{\frac{\tau_{ta}}{\rho_{air}}}, \qquad (1.1)$$

where β is a shape coefficient (Bagnold, 1941) and Φ could be considered as a parameter of packing arrangement of the grain. Using typical values for the parameters involved in Eq.(1.1) a value of $u_{*ta} = 0.25\,\text{m/s}$ could be found for a sand grain with diameter equal to $0.25\,\text{mm}$.
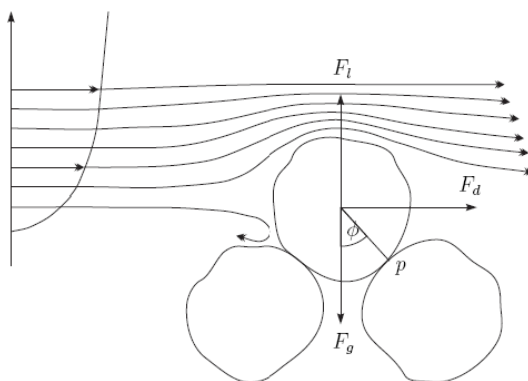
Figure 1.5: Schematic diagram showing the forces acting on a sand grain by the wind (Pye & Tsoar, 1990).

When a saltating grain impacts onto other grains on the surface, the hit grains may in turn raise, even if the wind shear velocity is lower than the threshold velocity u_{*ta}. Hence we define a lower threshold velocity u_{*t} named "impact threshold velocity" associated to an impact threshold shear stress τ_t. The value of u_{*t} is determined by empirical relations (*e.g.* $u_{*t} = u_{*ta}/\sqrt{2}$ in (Pye & Tsoar, 1990)).

Hence, the saltation transport is characterized by a first direct aerodynamic entrainment, *i.e.* to initiate saltation some grains have to be entrained directly by the air. At this point the low number of directly entrained grains give rise to a chain reaction in which a larger number of grains are ejected by the impacting grains. The sustained grains are then accelerated by the wind along their trajectory by the drag aerodynamic force. This is called the splash process, which involves the interactions between surface and impacting grain. Finally, the momentum transferred from the air to the grains leads in turn to a modification of the air velocity profile near the surface causing an auto-regulation mechanism which leads the saltation dynamics to an equilibrium state. For a detailed description of the phenomena and numerous citations of experimental results we refer to (Pye & Tsoar, 1990).

1.1.3 Shape of dunes

Principal parameters linked to dune movement and hence to dune morphology are the availability of sand and the variability of wind direction.

When the wind is nearly unidirectional the dunes are classified as barchan, barchanoids and transverse dunes. Barchans are present where the sand supply is limited and are characterized by a typical crescent moon shape, with convex windward face and steep, concave downwind face rounded by two wings. This is the classic dune shape. Barchanoids form when there is a larger sand supply and are composed by several joined barchan dunes. The transverse dunes usually form when there is an abundant supply of sand and are characterized by a ridge perpendicular to the wind direction.

When the wind blows in two non opposite directions the resulting dunes are linear with the crest straight along the wind mean direction, while when the wind blows in opposite directions dunes are of transverse type: their crests form a right angle with the wind direction.

When the wind variability and the sand supply are very high the resulting dunes are classified as star dunes and are characterized by elaborate shapes with more sinuous ridges radiating out from a central peak of sand. See Fig.1.6 for a representation of this type of dunes.

 Usually a dune is composed by a windward side and a downwind side. The former is the side where the sand grains are transported by the wind and is characterized by a gradually varying surface slope. The latter is the side where the wind shear stress is not able to transport the sand grains, which are hence deposited. On this face, when the slope exceeds the angle of repose, sand avalanches spontaneously arise. This relaxation process leads to a slope nearly constant and equal to the angle of repose, which for typical desert sand is 34°.

1.2 Current literature

In this section a short excursus in the current literature on the numerical modelling of sand dune evolution will be presented. Two main approaches could be distinguished:

(a) Barchan

(b) Linear

(c) Barchanoid/Transverse

(d) Star

Figure 1.6: Typical dune shapes.

continuum modelling or cellular automaton (CA). The continuum model is based on the search of a mathematical expression of sand mass transport (Anderson, 1987; Sauermann *et al.*, 2001). Then, the rate of change of local sand bed elevation is obtained from the divergence of the sediment flux.

In a CA model instead, the involved physical processes as erosion and deposition are modeled by time-dependent stochastic interaction rules between nearest-neighbors of a grid (Werner, 1995).

In the following we present a short description of the main continuum and cellular automaton models for dunes.

1.2.1 Continuum model

The pioneering works on the development of continuum models of aeolian dunes date back to the eighties (Wippermann & Gross, 1986; Zeman & Jensen, 1988; Stam, 1997; van Dijk *et al.*, 1999). None of these models was able to reproduce the movement of a barchan dune but they provided the basis for the next work of Sauermann *et al.* (2001) and Kroy *et al.* (2002) which has been further improved and validated by many authors in recent years (Sauermann *et al.*, 2003; Durán *et al.*, 2010). Continuum models are characterized by three principal ingredients: the modelling of the wind field over the

dune, the modelling of the saltation flux and the modelling of the avalanches.

Modeling the wind field Many authors (Wiggs, 2001; Parsons *et al.*, 2004; Herrmann *et al.*, 2005; Schatz & Herrmann, 2006; Livingstone *et al.*, 2007; Joubert *et al.*, 2012) approached wind field modelling by solving the Navier-Stokes equations of the turbulent wind over barchans and transverse dunes using computational fluid dynamics (CFD) packages. Although this approach has been useful to understand the flow patterns at the dune lee, it is too computationally expensive to be used to obtain a three-dimensional dune model. Only Ortiz & Smolarkiewicz (2006, 2009) simulated a complete three-dimensional dune with a highly efficient CFD code which exploit time-dependent curvilinear coordinates.

A less computationally expensive approach uses an analytical model to calculate the average turbulent wind shear stress field over the sand terrain. This model has been developed in several years (Jackson & Hunt, 1975; Hunt *et al.*, 1988; Weng *et al.*, 1991), and has been extensively used in dune models (Stam, 1997; Kroy *et al.*, 2002; Andreotti *et al.*, 2002b). The idea is to compute the Fourier-transformed components of the shear stress perturbation in the directions longitudinal and transverse to the wind, to obtain an expression for the (perturbed) shear stress. This analytical model works only for smooth heaps and gentle slopes and it does not apply for a dune with a slip face. Zeman & Jensen (1988) improved the method by introducing a separation bubble at the dune lee, which comprises the area of recirculating flow.

Modelling the saltation flux A continuum dune model requires an equation for the mass flux. For the mass flux modelling many authors (Wippermann & Gross, 1986; Zeman & Jensen, 1988; Stam, 1997) tried to use an equation for the saturated flux, although the flux upwind of a barchan dune is definitely below the saturated value (Fryberger *et al.*, 1984; Wiggs *et al.*, 1996). For this reason this strategy leads to unphysical results as demonstrated by Wiggs *et al.* (1996) and van Dijk *et al.* (1999). Sauermann *et al.* (2001) proposed a continuum model which takes into account the transients of the flux towards the saturated value. The set of saltating grains is modelled as a thin fluid-like layer moving on the top of a steady bed. The flux is calculated from the average density and velocity of grains jumping with a mean saltation trajectory. The spatial evolution of the average height-integrated mass flux over the sand bed is computed by solving a charge equation for the growth of the number of sand grains in the saltation flux, in a formulation that precludes flux growth over the unerodible surface. In their formulation a characteristic length is introduced to incorporate the exponential growth of the flux due to the cascade process inherent to the splash events (Andreotti *et al.*, 2010).

Modelling avalanches When the local slope exceeds the angle of repose of the sand, the surface relaxes through avalanches in the direction of the steepest descent. This phenomenon has a time scale much smaller than the dune evolution and could be considered as an instantaneous phenomenon that acts like a constraint on the maximum

admitted slope of the surface (Prigozhin, 1993, 1996; Aronsson *et al.*, 1996; Prigozhin & Zaltzman, 2001; Caboussat & Glowinski, 2009). An avalanches model of relatively fast convergence was proposed by Durán *et al.* (2010).

1.2.2   Cellular automation model

The cellular-automaton model for aeolian dunes was introduced for the first time by Werner (1995). He modelled the sand surface as sand slabs which are moved by the wind. In the algorithm a slab is chosen randomly on the surface and is moved downwind to a new grid place typically 5 grid steps away (Werner, 1995). Then the slab could be deposited with a probability p_d if the site where it arrives has no sand or with a probability p_s if the site has at least a one slab (usually $p_d < p_s$ in consistence with experimental observations, (Gordon & Neuman, 2009)). If no deposition occurs, the slab moves again in the direction of the wind to reach a new grid place until a deposition occurs. The process is executed again for another slab and so on. In this model the wind strength and power can be adjusted varying the path length and the probability of depositions. Moreover the model accounts for avalanches: if the slope becomes larger than $34°$ the slab are moved in the direction of the steepest descent until the slope goes back to an acceptable value. Finally, a shadow zone is introduced downwind : slabs entering there are deposited.

Many authors studied Werner's model (Werner & Kocurek, 1997, 1999; Kocurek & Ewing, 2005; Eastwood *et al.*, 2011) and improved it (Momiji *et al.*, 2000; Bishop *et al.*, 2002) to reach more realistic dune modeling. For example Momiji *et al.* (2000) added the condition of no erosion within shadow zones and Bishop *et al.* (2002) added a phenomenological non-linear equation for the transport length to account for the wind speed-up effect on the windward side of the dunes.

Recently, efforts have been made to include a physical modelling of the sand flux and the wind profile in the CA models. For example, Zheng *et al.* (2009) introduced in the model a wind friction velocity that increased linearly with the surface height; Pelletier (2009) coupled the Werner's model to a generalized version of the boundary layer flow model by Jackson & Hunt (1975). Narteau *et al.* (2009) and Zhang *et al.* (2010) solved the Navier-Stokes equations for the turbulent fluid with a three-dimensional lattice gas cellular automaton model (LGCA) coupling the resultant model to a probabilistic sand transport model.

1.3   Aim of our research

In this thesis work, we will develop a mathematical model for the evolution of dunes composed by a mixture of sands with different characteristics. In particular, we consider sands which can be distinguished only by their appearance, such as their colour, but which have the same physical properties such as diameter and density. These kind of sediments, known in the literature as "tracers" sediment, have been widely used in fluvial and beach sediment transport experimental studies and theoretical modelling

(Ingle, 1966; Parker, 1991; Armanini, 1995; Parker *et al.*, 2000; Hassan & Ergenzinger, 2005; Blom & Parker, 2004; Bradley *et al.*, 2010; Ganti *et al.*, 2010) , but relatively few authors have used them to monitor aeolian transport in the field (Berg, 1983; Tsoar & Yaalon, 1983; Cabrera & Alonso, 2010) or in wind tunnel (Willetts & Rice, 1988; Barndorff-Nielsen & Christiansen, 1988; Sørensen, 1988).

1.3.1 Remote sensing for hydrocarbon microseepage

This work has been funded by ENI S.p.A. as part of a wider research project started in November 2008 and finished in November 2010 called *"Analisi multidisciplinare di dati telerilevati con sensori ottici per l'individuazione di fenomeni di microseepage d'idrocarburi riconducibili alla presenza di giacimenti profondi"*, involving six Departments of Politecnico di Milano.

This work is mainly based on three hypothesis:

1. light hydrocarbons can seep through the seal rock of the reservoir, and hence rise to the Earth surface;

2. this hydrocarbon microseepage induces geochemical and/or geophysical alteration in the sedimentary column;

3. we can detect this superficial anomalies with remote sensing techniques.

If all these hypothesis hold, then the *remote sensing for hydrocarbon microseepage* may constitute in the future an easier and costless solution for the oil/gas exploration problem.

But what would happen in looking for microseepage in the deserts, where the wind moves the sediments creating sand dunes?

In other words: supposing that the microseepage induced alteration is adsorbed at the sand grain level; how will the superficial footprint of the reservoir be modified by the effect of the wind?

These are the questions that we try to answer in this Ph.D. thesis work. To this aim, we develop an original mathematical modelling of the dispersion of marked sand during the evolution of aeolian dunes.

1.4 Outline

In Chapter 2 the existing continuum modelling for saltation flux is critically reviewed and investigated. Chapter 3 is the core of this Ph.D. thesis, where the mathematical modelling for marked sand dispersion in aeolian dune will be developed and explained. In Chapter 4 we will describe the numerical methods for the simulation of the system, providing also some numerical simulations. In Chapter 5 we introduce a simplified version of the marked sand dispersion model suitable for two dimensional dune evolution, and we provide also some applications to interesting cases such as dune collision and remote sensing for hydrocarbon microseepage. Finally, some conclusions and suggestions for the following of this work will be given in Chapter 6.

2

Aeolian sand transport

In this Chapter, we present the continuum sand transport model that we have developed in this thesis work, starting from the model originally proposed in (Sauermann *et al.*, 2001). To avoid complicated notations, we restrict the exposition to a two dimensional domain that can be seen as a vertical slice aligned with the wind direction of a three dimensional system. In the following, x and z are the horizontal and vertical coordinates, $\mathbf{V} = (V(z), 0)$ is the wind velocity and $\mathbf{U} = (U_x(z), U_z(z))$ is the velocity vector of a characteristic sand grain, see Fig.2.1.
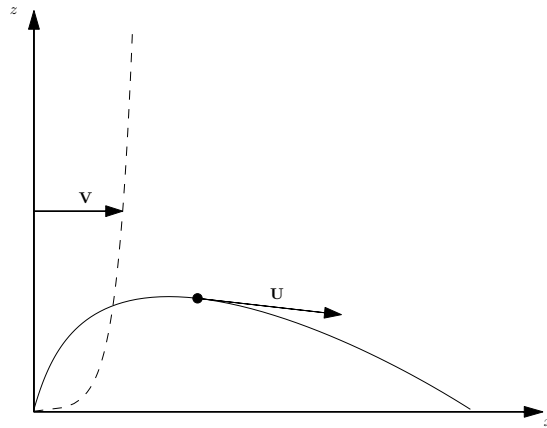
Figure 2.1: Trajectory of a sand grain - The trajectory of a sand grain, characterized by its velocity $\mathbf{U}$, is determined by the drag force exerted by the logarithmic wind profile $\mathbf{V}(z)$.

We aim at describing the flux of sand in saltation as a thin layer of sand grains which, transported by the wind, moves over an immobile sand bed. In particular, we will make the hypothesis that all grains in the saltation flux have identical trajectories. This idealized situation is called uniform saltation, and has been first proposed in (Bagnold,

1941) and adopted in several following models (Owen, 1964), since the most important aspects of the bulk dynamic behaviour of saltating particles, such as the momentum exchange between particle and flow, can be explained simply and qualitatively by considering the motion of a single particle with a characteristic trajectory. Furthermore, we can integrate over the vertical coordinate and use the scalar quantities $\rho(x,t)$ and $u(x,t)$ to describe respectively the total mass of sand in saltation over a surface of unit area (Kg/m^2) and the mean horizontal velocity (m/s) of the sand grains. The sand flux $q(x,t)$ is then given by $q = \rho u$.

2.1 Grain trajectory description

The sand transport is driven by the wind. Consider a fully developed turbulent wind over a flat surface. The standard turbulent closure relates the air shear stress τ to the velocity gradient $\partial_z V$:

$$\frac{\partial V}{\partial \ln z} = \frac{1}{\kappa}\sqrt{\frac{\tau}{\rho_{air}}} \qquad (2.1)$$

where ρ_{air} is the density of air and $\kappa \simeq 0.4$ is the Von Kárman constant. For a steady and uniform boundary layer, the shear stress τ is constant and equal to τ_∞, the shear stress far from the bed. This gives the well known logarithmic velocity profile:

$$V_0(z) = \frac{u_*}{\kappa}\ln\frac{z}{z_0} \qquad (2.2)$$

where the shear velocity u_* is by definition $u_* = \sqrt{\tau_\infty/\rho_{air}}$ and z_0 is the roughness of the surface, where $V_0(z_0) = 0$. If the flat surface is composed by "glued" grains of typical size d, it turns out that the velocity vanishes at a distance rd from the sand bed. The rescaled bed roughness r is found to be of the order of $1/30$ (Bagnold, 1941). A wind of sufficient strength can dislodge and entrain sand grains. Once the grain are dislodged, they are submitted to the gravity and to the fluid drag force. The drag force on a spherical particle of diameter d is

$$\mathbf{F}_{drag} = \frac{1}{2}\rho_{air}C_D\frac{\pi d^2}{4}(\mathbf{V}-\mathbf{U})|\mathbf{V}-\mathbf{U}| \qquad (2.3)$$

where $\mathbf{V} = (V,0)$ and $\mathbf{U} = (U_x, U_z)$ are the wind and the sand grain velocity vectors and the drag coefficient C_D depends on the shape of the grain, but not on the Reynolds number, because we are assuming a fully turbulent regime. Dividing by the mass m of a sand grain with diameter d and density ρ_{sand}, that is $m = \frac{4}{3}\pi\left(\frac{d}{2}\right)^3\rho_{sand}$, we obtain the drag acceleration which leads to the standard following formulation for the description of sand grain trajectory:

$$\begin{cases} \dfrac{\mathrm{d}\mathbf{U}}{\mathrm{d}t} &= \mathbf{g} + \dfrac{3}{4}C_D\dfrac{\rho_{air}}{\rho_{sand}}\dfrac{|\mathbf{V}-\mathbf{U}|(\mathbf{V}-\mathbf{U})}{d}, \\ \mathbf{U}(0) &= (U_{x0}, U_{z0}) \end{cases}$$

In the vertical direction, the motion is dominated by gravity. It immediately follows, as for a free parabolic flight, that the flight time T and the height of bounce z_m depend on the vertical launch speed U_{z0} as:

$$T = \frac{2U_{z0}}{g}, \qquad z_m = \frac{U_{z0}^2}{2g} \tag{2.4}$$

while the horizontal displacement –the saltation length– is of the order of the flight time T times the mean horizontal velocity u:

$$l = u\frac{2U_{z0}}{g}. \tag{2.5}$$

In the presence of saltating grain near the ground, the grains extract momentum from the air. Thus, in the saltation layer the total shear stress τ is divided into the air-borne shear stress τ_a and the shear stress carried by the grains, the grain-borne shear stress τ_g:

$$\tau = \tau_a(z) + \tau_g(z) = \tau_\infty. \tag{2.6}$$

Since the sand grains are accelerated by the wind, at a given height z they have a smaller horizontal velocity $U_x^\uparrow$ when they go up than when they come down again ($U_x^\downarrow$). We call Φ the mass of sand which impact a unit area of the sand bed per unit time; it is related to the horizontal mass flux q integrated along the vertical and to the mean saltation length l:

$$\Phi = \frac{q}{l} = \frac{\rho}{T}.$$

The momentum transferred to this mass of sand is by definition the grain-borne shear stress τ_g and is equal to the mass flux Φ times the velocity difference $U_x^\downarrow - U_x^\uparrow$

$$\tau_g(z) = \Phi\left(U_x^\downarrow(z) - U_x^\uparrow(z)\right) = \Phi\Delta U_x(z). \tag{2.7}$$

From now on, using the subscript 0 to indicate the values at $z = z_0$, we restrict the analysis to the grain-borne shear stress at the surface τ_{g0}, as it is a fundamental quantity which also gives the momentum transfer from the grains to the bed during the impacts. Inserting Eq.(2.5) in Eq.(2.7) we obtain

$$\tau_{g0} = \frac{\rho g}{2}\frac{\Delta U_{x0}}{U_{z0}} \tag{2.8}$$

At this point, following (Sauermann *et al.*, 2001), considering that $U_{x0}^\downarrow \gg U_{x0}^\uparrow$, we note that the velocity difference $\Delta U_{x0} \simeq U_{x0}^\downarrow$. The simplest possibility to describe the splash function, that is the joint probability density function of the velocities after impact given the impact velocity, is to take the vertical ejection velocity U_{z0} proportional to the horizontal impact velocity $U_{x0}^\downarrow$, or:

$$U_{z0} = \alpha\Delta U_{x0} \tag{2.9}$$

were $\alpha < 1$ is the first model parameter that represents the loss of momentum during the impact. With this simple model, Eq.(2.8) reduces to

$$\tau_{g0} = \frac{\rho g}{2\alpha} \tag{2.10}$$

2.2 A continuum model for saltation flux

The saltation layer exchanges sediments with the bed, so the mass conservation equation includes a source term which represents the erosion rate:

$$\frac{\partial \rho}{\partial t} + \frac{\partial}{\partial x}(\rho u) = \Gamma, \tag{2.11}$$

where Γ is defined as the difference between the mass of grains leaving the surface and the mass of grains impacting onto it, per unit area and time.

The momentum conservation equation includes external volumetric forces acting on the sand grains

$$\rho \left(\frac{\partial u}{\partial t} + u \frac{\partial u}{\partial x} \right) = f_{drag} + f_{bed}, \tag{2.12}$$

where f_{drag} is the wind drag force which accelerates the grains, f_{bed} is the friction force representing the lost of momentum of sand grains impacting to the ground. In the next subsections we will detail the modelling of the terms Γ, f_{drag}, f_{bed} and present a closed model in Sect.2.2.3.

2.2.1 Erosion rate

The erosion rate Γ is linked to two distinct phenomena: on the one hand, we have a collisional erosion rate Γ_i representing the balance between the number of impacting and splashed grains, on the other hand we have the mass of sand directly entrained by the wind Γ_a. The collisional erosion rate Γ_i can be defined as:

$$\Gamma_i = \Phi(n - 1),$$

where Φ is the impact rate, *i.e.* the mass of sand which impact on a unit area in unit time, and n is the average number of grains leaving the surface per each grain impacting on it. To be more precise, Φn is the ascending flux that counts the mass of sand grains that leave a unit surface in unit time with positive vertical velocity.

The air-borne shear stress is reduced if the number of grains in the saltation layer increases. At saturation, the number of grains leaving the surface equals the number of impacting grains ($n = 1$), and, according to Owen's hypothesis (1964), the air-borne shear stress at the bed τ_{a0} is just large enough to sustain saltation. We define a threshold shear stress τ_t which can be written as a function of a threshold shear velocity u_{*t}: $\tau_t = \rho_{air} u_{*t}^2$.

When $\tau_{a0} > \tau_t$, the chain reaction is sustained and the number of grains leaving the surface increases ($n > 1$), whereas for $\tau_{a0} < \tau_t$ the chain reaction cannot be maintained

and saltation is suppressed ($n < 1$). Hence, we can model this physical mechanism writing n as a function $n(\tau_{a0}/\tau_t)$ with $n(1) = 1$. The first order Taylor series expansion for n around the threshold leads to the following functional expression:

$$n\left(\frac{\tau_{a0}}{\tau_t}\right) \cong 1 + \left.\frac{\mathrm{d}n}{\mathrm{d}\left(\tau_{a0}/\tau_t\right)}\right|_{\tau_{a0}=\tau_t} \left(\frac{\tau_{a0} - \tau_t}{\tau_t}\right) = 1 + \tilde{\gamma}\left(\frac{\tau - \tau_{g0} - \tau_t}{\tau_t}\right), \qquad (2.13)$$

where $\tilde{\gamma} = \mathrm{d}n/\,\mathrm{d}(\tau_{a0}/\tau_t)$ is a model parameter which determines how fast the system reacts to perturbation of the equilibrium state.

We use now the modelling of the impaction rate Φ and the surface grain-borne shear stress τ_{g0} given in Sect.2.1, and model the erosion rate in the form:

$$\Gamma_i = \frac{\rho}{T}\left(\tilde{\gamma}\frac{\tau - \tau_{g0} - \tau_t}{\tau_t}\right) = \frac{\rho}{T}\tilde{\gamma}\frac{\tau - \tau_t}{\tau_t}\left(1 - \frac{\tau_{g0}}{\tau - \tau_t}\right).$$

Now we have to determine the flight time $T = 2U_{z0}/g$; we can use the hypothesis of Eq.(2.9)

$$T = \frac{2\alpha\Delta U_{x0}}{g}$$

and finally hypothesize that the velocity difference ΔU_{x0} is proportional to the mean velocity u

$$\Delta U_{x0} = \frac{u}{r}, \qquad (2.14)$$

where r is a new parameter of the model. Using Eq.(2.10), we finally obtain the closed form:

$$\Gamma_i = r\tilde{\gamma}\frac{g}{2\alpha}\frac{\tau - \tau_t}{\tau_t}\frac{\rho}{u}\left(1 - \frac{g}{2\alpha}\frac{1}{(\tau - \tau_t)}\rho\right). \qquad (2.15)$$

Up to now, we only discussed the erosion rate due to collisions with impacting grains. Direct aerodynamic entrainment of grains is possible if the air shear stress is greater than the aerodynamic threshold $\tau_{ta} > \tau_t$. The sand grains entrained by the air are extremely important to start saltation, *e.g.* at the boundary between a zone without sand and a zone covered with sand. However, if there is a sufficiently large number of grains in the saltation flux, the direct aerodynamic entrainment becomes negligible and grains are ejected by collisions only. Following (Anderson, 1991; Sauermann *et al.*, 2001), the aerodynamic entrainment is a strictly positive quantity proportional to the difference between the air born shear stress at the ground τ_{a0} and the aerodynamic threshold τ_{ta}

$$\Gamma_a = \gamma_a \max\left(\frac{\tau_{a0}}{\tau_{ta}} - 1, 0\right), \qquad (2.16)$$

where γ_a is a model parameter defining the strength of erosion rate for aerodynamic entrainment.

2.2.2 Forces

In the following we specify the volumetric forces acting on the saltation layer which appear in Eq.(2.12). Saltating grains lose part of their momentum to the ground during the impact; this physical mechanism is taken into account by including a friction force acting on the saltation layer f_{bed}. Following the notation of Section 2.1, the friction force is:

$$f_{bed} = \Phi \left(U_{x0}^{\uparrow} - U_{x0}^{\downarrow} \right) = -\Phi \Delta U_{x0}.$$

This force exactly counterbalance the grain born shear stress τ_{g0} as defined in Eq.(2.7), and hence we can use the closed form of Eq.(2.10) to write:

$$f_{bed} = -\frac{\rho g}{2\alpha}.$$

The volumetric drag force exerted by the wind on the saltation layer can be obtained starting from the expression of the drag force on sand grain of Eq.(2.3). As we consider only the mean horizontal velocity u of the saltation layer, we take an effective wind velocity v_{eff} for the calculation of the drag force. This effective wind velocity is the value of the real wind velocity $V(z)$ taken at a reference height z_1 inside the saltation layer: $v_{eff} = V(z_1)$. Multiplying Eq.(2.3) by the density ρ of the saltation layer and dividing it by the mass m of a sand grain we obtain the volumetric drag force:

$$f_{drag} = \rho \frac{3}{4} C_D \frac{\rho_{air}}{\rho_{sand}} \frac{|v_{eff} - u|(v_{eff} - u)}{d} \tag{2.17}$$

To calculate the effective wind velocity v_{eff}, we cannot use the unperturbed logarithmic wind profile of Eq.(2.2), because the saltating grains change the wind profile close to the ground. Following (Durán & Herrmann, 2006a), assuming that the turbulent boundary layer is still at equilibrium, the standard turbulent closure of Eq.(2.1), combined with the shear stress partitioning of Eq.(2.6) leads to the modified velocity profile given by:

$$\frac{\partial V}{\partial \ln z} = \frac{1}{\kappa} \sqrt{\frac{\tau_a(z)}{\rho_{air}}} = \frac{u_*}{\kappa} \sqrt{1 - \frac{\tau_g(z)}{\tau_\infty}}.$$

Above the saltation layer ($z \geq z_m$, where z_m is the height of the saltation layer already introduced in Eq.(2.4)), there is no grain and thus no grain-borne shear stress: $\tau_a(z \geq z_m) = \tau_\infty$. In the saltation layer, the air born shear stress is strongly reduced, and is much smaller than τ_∞. As a consequence the related shear velocity

$$u_{*a}(z) = u_* \sqrt{1 - \frac{\tau_g(z)}{\tau_\infty}}$$

is smaller than u_*. Following (Sørensen, 2004) and (Durán & Herrmann, 2006a), defining

$$a(z) = \tau_g(z)/\tau_{g0},$$

where, as usual, the subscript 0 indicates the value at $z = z_0$, the wind shear velocity in the saltation layer is given by

$$u_{*a}(z) = u_* \sqrt{1 - \frac{\tau_{g0}}{\tau_\infty} a(z)}$$

$$= u_* \sqrt{1 - \left(1 - \frac{\tau_{a0}}{\tau_\infty}\right) a(z)} \qquad (2.18)$$

$$= u_* \sqrt{1 - \left(1 - \frac{u_{*a0}^2}{u_*^2}\right) a(z)}$$

that satisfies the boundary condition $u_{*a} = u_{*a0}$ at the surface, where $a(z) = 1$, and $u_{*a} = u_*$ above the saltation layer, where $a(z) = 0$.

Since equation (2.18) does not yeld an explicit expression for the wind profile, Durán & Herrmann (2006a) replaced the square root $\sqrt{1 - \left(1 - u_{*a0}^2/u_*^2\right) a(z)}$ by the linear function $1 - (1 - u_{*a0}/u_*) a(z)$ which reproduces the boundary conditions and the monotonicity of the original expression. Hence, using the closure (2.1), they proposed the wind profile

$$V(z) = \frac{u_*}{\kappa} \left[\ln \frac{z}{z_0} - \left(1 - \frac{u_{*a0}}{u_*}\right) b(z) \right], \qquad (2.19)$$

where the dimensionless function b is given by

$$b(z) = \int_{z_0}^z \frac{a(\zeta)}{\zeta} \, \mathrm{d}\zeta.$$

The graph of the modified wind velocity profile will be represented in Sect.2.2.5. Near the bed, where $a(z) \sim 1$ and $b(z) \sim \ln z/z_0$, the wind velocity recovers its usual logarithmic profile, but with the reduced shear velocity u_{*a0}:

$$V(z) \approx \frac{u_{*a0}}{\kappa} \ln \frac{z}{z_0}$$

whereas, above the saltation layer $a(z) = 0$ and the wind profile is logarithmic with an unperturbed shear velocity u_*

$$V(z) \approx \frac{u_*}{\kappa} \ln \frac{z}{z_0'}$$

but with a increased roughness length z_0' which takes into account the apparent rugosity of saltation:

$$z_0' \approx z_0 \exp\left[\left(1 - \frac{u_{*a0}}{u_*}\right) b_\infty\right]. \qquad (2.20)$$

In order to find a closed form for $b(z)$, following (Sauermann *et al.*, 2001; Durán & Herrmann, 2006a) we assume an exponential profile for the grain born shear stress, that is $a(z) = \exp(-z/z_m)$. This assumption leads to

$$b(z) = \int_{z_0}^z \frac{\exp(-\zeta/z_m)}{\zeta} \, \mathrm{d}\zeta. \qquad (2.21)$$

Considering that we want to evaluate $v_{eff} = V(z_1)$ where the reference height $z_1 \ll z_m$, we linearize the exponential in Eq.(2.21) obtaining

$$b(z_1) \simeq \ln \frac{z_1}{z_0} - \frac{z_1}{z_m}$$

which, using Eq.(2.19), leads to write the following expression for the effective velocity:

$$v_{eff} = \frac{u_{*a0}}{\kappa} \left[\ln \frac{z_1}{z_0} + \frac{z_1}{z_m} \left(\frac{u_*}{u_{*a0}} - 1 \right) \right]. \tag{2.22}$$

Here we recall that, by definition,

$$u_{*a0} = u_* \sqrt{1 - \frac{\tau_{g0}}{\tau_\infty}}, \tag{2.23}$$

where the grain born shear stress at the ground can be written using the result of Eq.(2.10); hence, the v_{eff} is function of the density ρ. In Eq.(2.22), the height z_1 is a parameter of the model.

2.2.3 Closed model and saturated sand flux

In the previous sections we have introduced the erosion rate Γ, the drag force f_{drag} and the friction force f_{bed} which determine the temporal and spatial evolution of the density ρ and velocity u of the saltating sand flux. To close the system, we have introduced two non dimensional parameters α and r linked to the grain trajectory, a non dimensional parameter $\tilde{\gamma}$ that controls the strength of the erosion process, a reference height z_1 inside the saltation layer where the effective wind velocity responsible for the drag force is calculated as well as the bed roughness z_0 and the saltation height z_m. The last two parameters can be obtained from direct measurements.
In the expression of the erosion rate Eq.(2.15), we can identify two important physical quantities: the density ρ_{sat} which characterizes the steady state and the characteristic time T_{sat} to reach saturation:

$$\rho_{sat} = \frac{2\alpha}{g}(\tau - \tau_t), \tag{2.24}$$

$$T_{sat} = \frac{2\alpha}{g} \frac{u}{r\tilde{\gamma}} \frac{\tau_t}{(\tau - \tau_t)}. \tag{2.25}$$

With these expressions, injecting the erosion rate of Eq.(2.15) in the conservation equation (2.11) we obtain the compact form:

$$\boxed{\frac{\partial \rho}{\partial t} + \frac{\partial}{\partial x}(\rho u) = \frac{\rho}{T_{sat}} \left(1 - \frac{\rho}{\rho_{sat}} \right).} \tag{2.26}$$

The erosion rate due to direct aerodynamic entrainment can be also taken into account adding the term Γ_a of Eq.(2.16) to the right hand side.

In the expression of the drag force of Eq.(2.17), we can identify another important physical quantity: the terminal fall velocity in air u_f of a sand grain of diameter d and density ρ_{sand}:

$$u_f = \sqrt{\frac{4}{3}\frac{\rho_{sand}}{C_D}\frac{\rho_{sand}}{\rho_{air}}gd}, \tag{2.27}$$

which can be obtained from the balance between the gravitational force and the drag resistance

$$g\rho_{sand}\frac{\pi\,d^3}{6} = \frac{1}{2}\rho_{air}C_D\frac{\pi d^2}{4}u_f^2.$$

With this expression, the balance of forces of Eq.(2.12) is written in the compact form:

$$\boxed{\rho\left(\frac{\partial u}{\partial t} + u\frac{\partial u}{\partial x}\right) = \rho g\frac{|v_{eff} - u|(v_{eff} - u)}{u_f^2} - \frac{\rho g}{2\alpha}.} \tag{2.28}$$

Finally, the mass and momentum conservation Eqs.(2.26) and (2.28), with the definitions of Eqs.(2.22), (2.24) and (2.25), constitute the closed model for the sand flux in the saltation layer. This is a system of coupled partial differential equations, whose full dynamics must be solved numerically.

On the other hand we can calculate analytically the saturated sand flux, which is the equilibrium transport capacity for a given constant external shear stress $\tau(x,t) = \tau$ above the threshold (otherwise, only the trivial null solution exists). For this purpose, we consider the stationary solution ($\partial/\partial t = 0$) on an homogeneous bed ($\partial/\partial x = 0$). From Eq.(2.26), the only non vanishing solution is the saturated density defined in Eq.(2.24) which, in terms of the shear velocity, becomes

$$\rho_{sat}(u_*) = \frac{2\alpha}{g}\rho_{air}\left(u_*^2 - u_{*t}^2\right). \tag{2.29}$$

At saturation, for the Owen's hypothesis already introduced in Sect.2.2.1, the residual shear velocity of the wind at the ground u_{*a0} is equal to the threshold shear velocity u_{*t}. Hence, at saturation, the effective wind velocity responsible for the drag acceleration of Eq.(2.22) is

$$v_{sat}(u_*) = \frac{u_{*t}}{\kappa}\left[\ln\frac{z_1}{z_0} + \frac{z_1}{z_m}\left(\frac{u_*}{u_{*t}} - 1\right)\right]. \tag{2.30}$$

The stationary solution of the momentum conservation equation (2.28) leads to the following expression for the mean velocity of the saturated sand flux:

$$\begin{aligned}
u_{sat}(u_*) &= v_{sat}(u_*) - \frac{u_f}{\sqrt{2\alpha}} \\
&= \frac{u_{*t}}{\kappa}\left[\ln\frac{z_1}{z_0} + \frac{z_1}{z_m}\left(\frac{u_*}{u_{*t}} - 1\right)\right] - \frac{u_f}{\sqrt{2\alpha}}.
\end{aligned} \tag{2.31}$$

Here we notice that, in contrast to the saturated density ρ_{sat}, the saturated velocity u_{sat} does not goes to zero near the threshold, but has a finite value

$$u_{sat}(u_{*t}) = \frac{u_{*t}}{\kappa}\ln\frac{z_1}{z_0} - \frac{u_f}{\sqrt{2\alpha}}, \tag{2.32}$$

which reflects the consideration that sand grains at threshold have a finite velocity. Finally, the steady state sand flux $q_{sat} = \rho_{sat} u_{sat}$ at saturation is

$$q_{sat}(u_*) = \frac{2\alpha}{g} \rho_{air} \left(u_*^2 - u_{*t}^2 \right) \left(\frac{u_{*t}}{\kappa} \left[\ln \frac{z_1}{z_0} + \frac{z_1}{z_m} \left(\frac{u_*}{u_{*t}} - 1 \right) \right] - \frac{u_f}{\sqrt{2\alpha}} \right). \qquad (2.33)$$

For wind speeds well above the threshold, the flux is proportional to u_*^3; this asymptotic behaviour has been found in many others saltation models (Bagnold, 1941; Owen, 1964; Sørensen, 2004).

2.2.4 Parameters

Here we detail the physical constants and the model parameters that has been introduced in the previous sections and that will be assumed in the rest of our work.
Fist of all, we use typical values encountered in the literature (Owen, 1964; Pye & Tsoar, 1990; Anderson, 1991; Sauermann *et al.*, 2001) for the sand grain diameter $d = 250\,\mu$m, the air density $\rho_{air} = 1.225\,\mathrm{Kg/m^3}$ and the sand density $\rho_{sand} = 2650\,\mathrm{Kg/m^3}$.
From Parteli (2007) we use the value for the impact threshold friction velocity $u_{*t} = 0.217\,$m/s. For direct aerodynamic entrainment calculation from Sauermann (2001); Parteli (2007) we take the aerodynamic threshold friction velocity $u_{*ta} = 1.25 u_{*t} = 0.271\,$m/s and the strength of the erosion rate $\gamma_a = 5.7 \times 10^{-4}\,\mathrm{Kg\,m^{-2}\,s^{-1}}$. We take the value of the drag coefficient $C_D = 3$ as in Sauermann (2001); Parteli (2007); Durán (2007).
The parameters of the wind model are taken from Durán & Herrmann (2006a), where the authors have first obtained the grain based roughness length $z_0 = 10\,\mu$m and the characteristic height of the saltation layer $z_m = 20\,$mm fitting the expression of the apparent roughness length of Eq.(2.20) to the wind tunnel data of Rasmussen *et al.* (1996), and then obtained the reference heigh $z_1 = 3\,$mm and the splash parameter $\alpha = 0.4$ from the best fit of Eq.(2.33) to experimental data by Iversen & Rasmussen (1999) of the saturated sand flux q_{sat} as function of u_*.
The two remaining parameter are $\tilde{\gamma}$ and r, introduced in Eq.(2.13) and (2.14) respectively. We notice that they finally appear in the closed form of the erosion rate of Eq.(2.15) as a multiplicative prefactor. Hence, starting from the original formulation of Sauermann *et al.* (2001), the two parameters have been incorporated in a single parameter $\gamma = r\tilde{\gamma}$, whose value $\gamma = 0.4$ has been estimated by Sauermann *et al.* (2001) comparing the saturation time T_{sat} of Eq.(2.25) to measurements by Butterfield (1993) and microscopic simulations by Anderson & Haff (1988); Anderson (1991); McEwan & Willetts (1991).

2.2.5 Results

After the definition of all the parameters, we clarify the behaviour of the model with some examples.

Modified wind velocity profile

First, in Fig.2.2, we visualize the wind velocity profile modified by the presence of the saltation layer. The wind profile $V(z)$ of Eq.(2.19) is calculated for a typical shear velocity $u_* = 0.5\,\mathrm{m/s}$ after numerical integration of the term $b(z)$ in Eq.(2.21). We assume a saturated sand flux, hence for the Owen's hypothesis inside the saltation layer the residual shear velocity u_{*a0} is equal to the threshold u_{*t}, whereas the roughness z_0 is the same of the unperturbed wind profile $V_0(z)$ of Eq.(2.2). Above the saltation layer $(z > z_m)$, there are no grains and thus the shear velocity is the same as the undisturbed profile u_*, but the apparent roughness is increased to the value z_0' given in Eq.(2.20) in consequence of the presence of the saltation layer.
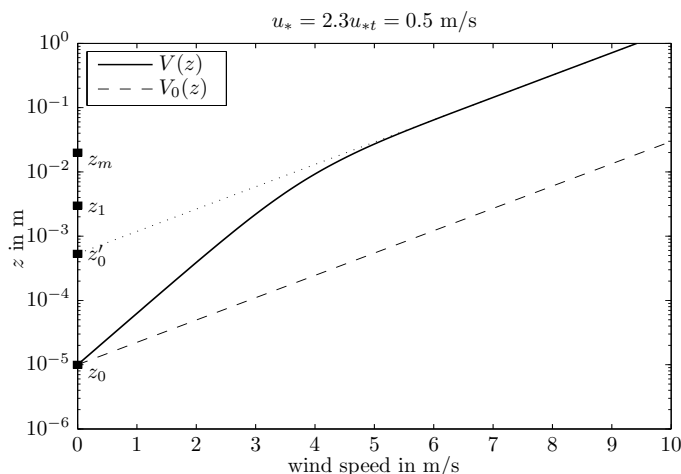
Figure 2.2: Wind velocity profile modified by a saturated sand flux - The undisturbed logarithmic wind profile $V_0(z)$ is modified by the saltation flux; $V(z)$ is a piecewise logarithmic profile. Inside the saltation layer $(z < z_m)$, the shear velocity is decreased to the threshold u_{*t} and the roughness is that of the unperturbed profile z_0. Outside $(z > z_m)$ the shear velocity is u_* but the apparent roughness z_0' due to the presence of the saltation layer is increased. The values of the model parameters z_0, z_1 and z_m are represented on the left axis.

Saturated sand flux

Now we compare the saturated sand flux q_{sat} given in Eq.(2.33) with other transport law found in literature and wind tunnel measurements. The transport law of Bagnold (1941); Lettau & Lettau (1978) and Sørensen (2004), used for comparison, are

31

respectively:

$$q_B = C_B \frac{\rho_{air}}{g} u_*^3, \tag{2.34}$$

$$q_L = C_L \frac{\rho_{air}}{g} u_*^2 \left(u_* - u_{*t} \right), \tag{2.35}$$

$$q_S = \frac{\rho_{air}}{g} u_* \left(u_*^2 - u_{*t}^2 \right) \left(C_\beta \frac{u_{*t}^2}{u_*^2} + C_\gamma \frac{u_{*t}}{u_*} \right), \tag{2.36}$$

where the values of the constants are $C_B = 1.8$, $C_L = 4.2$, $C_\beta = 3.9$ and $C_\gamma = 3.0$. For a better comparison, in Fig.2.3 the sand flux is made non dimensional by dividing it by $Q_0 = \rho_{air} u_*^3 / g$. We also report the wind tunnel measurements of Iversen & Rasmussen (1999) obtained with sand grains of diameter $d = 242 \, \mu$m.
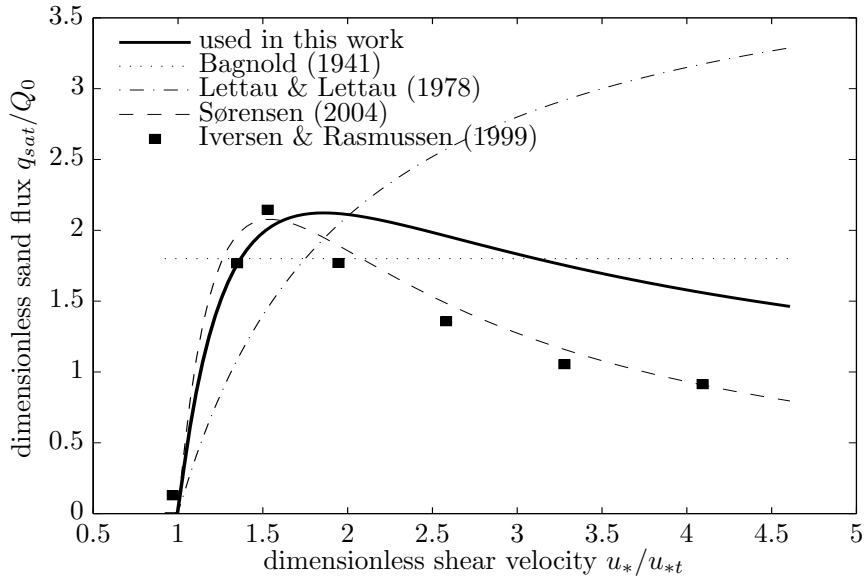
Figure 2.3: Saturated saltation flux $q_{sat}(u_*)$ - Comparison of the transport laws (2.34),(2.35) and (2.36) and the wind tunnel data of Iversen & Rasmussen (1999). The fluxes are normalized by $Q_0 = \rho_{air} u_*^3 / g$.

The saturated sand flux expression of Eq.(2.33) reproduces the observed peak of the dimensionless sand flux at $u_* \approx 1.5 - 2 \, u_{*t}$ and the subsequent decrease for larger shear velocity. The Sørensen (2004) transport law shows the best fitting of wind tunnel data, especially for high shear velocity. The model of Eq.(2.33) overestimates the saturated sand flux at high shear velocity. Durán & Herrmann (2006a) showed that the proposed model can achieve a best fit of wind tunnel data if we replace the Owen (1964) hypothesis used for Eq.(2.30) with the so called "focal point assumption", *i.e.* if we assume (Bagnold, 1941; Andreotti, 2004) that, in presence of a saturated sand flux, there is a fixed height inside the saltation layer at which the wind velocity is constant for all shear velocity. With this hypothesis the surface air shear velocity u_{*a0} decreases

with u_*, and so the effective wind velocity v_{eff} of Eq.(2.22) at saturation increase with u_* slower than in Eq.(2.30), leading to no overestimation of the saturated sand flux at large shear velocity. However, to keep the model simple and avoid the characterization of another parameter (the focal point height), we follow Durán (2007) and assume no focal point.

Temporal dynamics
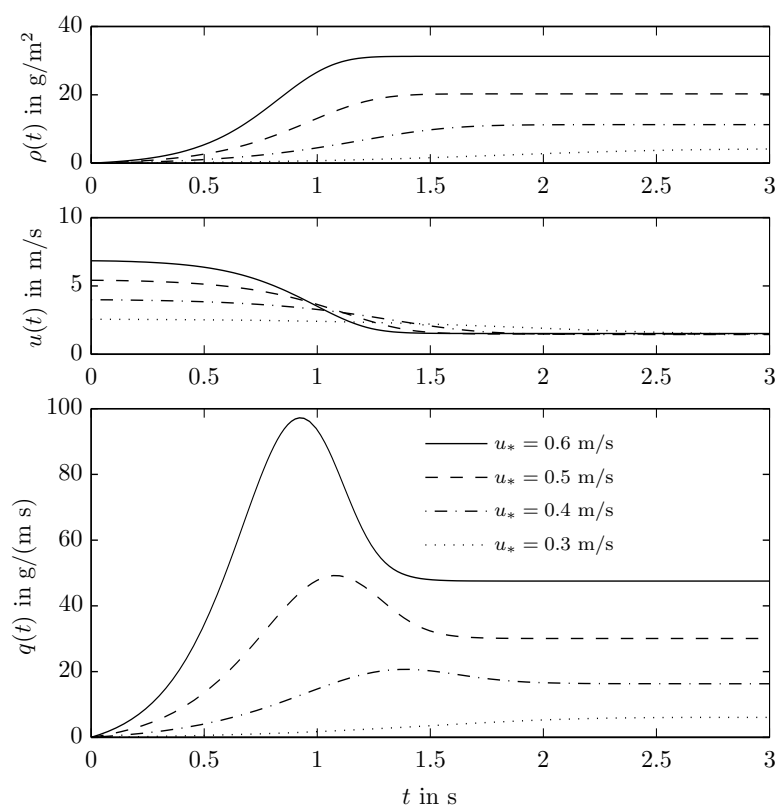
Figure 2.4: Time evolution of the saltation model using spatially homogeneous conditions - The numerical simulations of the time evolution of the saltation model is computed neglecting the spatial derivative and considering a constant shear velocity u_*. From top to bottom the temporal evolution of the density $\rho(t)$, velocity $u(t)$ and flux $q(t)$ is represented.

We now investigate the dynamics of the model. We fist consider spatially homogeneous conditions, namely we neglect the spatial derivative ($\partial/\partial x = 0$). The saltation model of Eq.(2.26)-(2.28) becomes a system of two coupled ordinary differential equations which must be solved numerically on an assigned time interval providing initial boundary conditions for the two variables. The dynamics of the system is determined by the

shear velocity u_* which determines the shear stress exerted by the wind on the sand surface.

We initialize the simulation with a very small density $\rho(0) = \varepsilon \rho_{sat}$ with $\varepsilon = 10^{-6}$ and a velocity $u(0) = v_{eff}(\rho(0)) - u_f/\sqrt{2\alpha}$ such that the drag and the bed forces cancel at $t = 0$. With these boundary conditions we want to investigate the transient process to saturation. The results, which span different values of shear velocity u_*, always assumed constant in time, are shown in Fig.2.4. Here we include in the model also the direct aerodynamic entrainment Γ_a given in Eq.(2.16).

The number of grains in saltation $\rho(t)$ increases exponentially, due at first to the direct aerodynamic entrainment and then to the multiplication effect of the saltation process, and after $\approx 2\,\mathrm{s}$ reaches the equilibrium state $\rho_{sat}(u_*)$ given in Eq.(2.29).

At the beginning of the simulation the velocity is high because the density ρ is low and hence the wind velocity v_{eff} responsible for drag acceleration is high. Then, as the density reaches the saturated value, the velocity decreases to the equilibrium velocity $u_{sat}(u_*)$ of Eq.(2.31). In Fig.2.4 we can clearly notice that the the equilibrium value u_{sat} is very similar for all the shear velocity considered. In detail, we can calculate from Eq.(2.31) that u_{sat} grows linearly from $1.4\,\mathrm{m/s}$ when $u_* = u_{*t}$ to $1.9\,\mathrm{m/s}$ when $u_* = 1\,\mathrm{m/s}$. This is a very small range of variation that cannot be observed on the scale of the axis of Fig.2.4. The almost independence of the mean velocity of the saturated saltation flux from the shear velocity has been recently noticed also by Creyssels *et al.* (2009) with accurate measurements of saturated sand flux with particle image velocimetry (PIV) and particle-tracking velocimetry (PTV) techniques and by Durán *et al.* (2011) with accurate microscopical numerical simulations based on discrete element method (DEM) for sand particles.

The coupled effect of growing density and decreasing velocity leads to a flux profile $q(t)$ with an overshooting at $\approx 1\,\mathrm{s}$ for high shear velocity.

Temporal and spatial dynamics

Now we consider the complete dynamics of the model, which can be obtained by solving numerically the system of coupled partial differential equations (2.26)-(2.28). The details of the numerical methods used for the resolution will be provided in Sect.4.2.1. We consider the physical domain $x \in [0, 10]\,\mathrm{m}$ and the time interval $t \in [0, 10]\,\mathrm{s}$. The dynamics of the model is determined by inflow and initial condition; we choose a very small density of sand in saltation: $\rho(0, t) = \rho(x, 0) = \varepsilon \rho_{sat}$ with $\varepsilon = 10^{-6}$ and a flux velocity in local equilibrium with the the inflow flux density, like the previous case. With these initial and boundary conditions we want to investigate the dynamics of the saturation process. Also in this example we include the direct aerodynamic entrainment Γ_a.

In Fig.2.5 we represent the stationary solution obtained assuming a constant (in space and time) shear velocity $u_* = 0.3\,\mathrm{m/s}$. Despite the small shear velocity near the threshold u_{*t} we have considered, the obtained stationary solution shows an interesting spatial pattern. The stationary density profile $\rho(x)$ in fact grows exponentially and reaches the saturated value after passing through a maximum at $x \approx 5\,\mathrm{m}$. This overshoot of
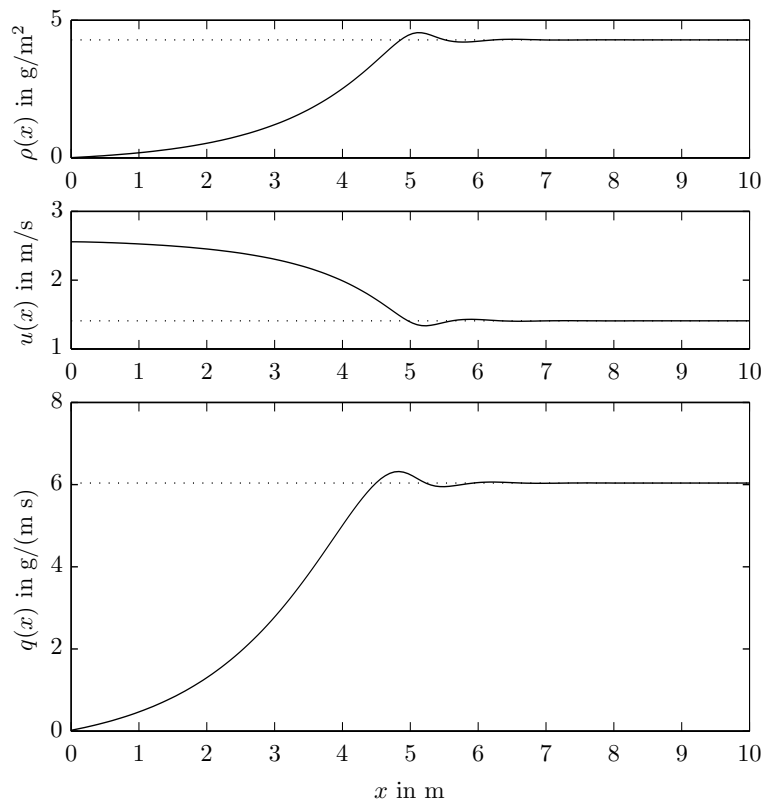
Figure 2.5: Stationary solution of the saltation model for $u_* = 0.3\,\mathrm{m/s}$ - The stationary solution of the saltation model of Eq.(2.26)-(2.28) is computed for a shear velocity near the threshold. From the top are represented the density $\rho(x)$, the velocity $u(x)$ and the sand flux $q(x) = \rho u$. We notice the overshooting of the density before reaching the saturated value (dotted line).

the density profile has not been observed in the previous example, where we neglected the spatial derivative, and hence it is a result of the coupling between the transport term and the erosion term.

This dynamics has to be taken into account if we look at the definition of the residual shear velocity at the ground u_{*a0}, which is necessary to calculate the effective wind velocity inside the saltation layer in Eq.(2.22); from Eq.(2.23) and the definition of the grain born shear stress of Eq.(2.10) we have

$$u_{*a0} = \sqrt{1 - \frac{\rho g}{2\alpha\tau}}.$$

35

Since the argument of the square root must be positive, we must satisfy

$$\rho \leq \frac{2\alpha}{g}\tau = \rho_{sat} + \frac{2\alpha}{g}\tau_t.$$

To quantify, we have a safety margin of $2\alpha\tau_t/g = 4.7\,\mathrm{g/m^2}$ for the amplitude of the overshoot. In view of practical applications of the model, this result is a too strict constraint. For example, if we replicate the previous numerical simulation at the shear velocity of $u_* = 0.4\,\mathrm{m/s}$, the overshoot tends to become greater than the maximum allowed, leading to a mistake in the mathematical formulation of the model.
Hence we introduce one simplification that allows us to use the model in the following of our work.

2.3   A useful simplification

Due to the problems that can arise in the calculation of the residual shear velocity u_{*a0} when the density of grains exceed the saturated value, we follow Sauermann *et al.* (2001) and assume that we can approximate the effective wind velocity $v_{eff}(u_*, \rho)$ of Eq.(2.22) with the equilibrium value $v_{sat}(u_*)$ of Eq.(2.30). That is, in the calculation of the effective wind velocity, we take the density of the saltation flux at its saturated value or, in other words, we take the residual shear velocity u_{*a0} always equal to the threshold u_{*t}, which is the Owen's hypothesis. This hypothesis does not modify the saturated quantities ρ_{sat}, u_{sat} and q_{sat}, but changes the dynamic towards saturation.
In particular, in Fig.2.6, we report the stationary solution of the simplified model obtained with the same initial and inflow condition of the previous case. Since we have changed the definition of v_{eff} and hence the drag force f_{drag}, now the initial velocity and inflow condition in equilibrium with the inflow density is given by $u(0, t) = u(x, 0) = v_{sat}(u_*) - u_f/\sqrt{2\alpha}$. Since we are considering a shear velocity u_* constant in time and space, the initial constant profile of the velocity is maintained for all the computation. We notice that the stationary density profile $\rho(x)$ does not present the overshoot, and it saturates at $x \approx 3\,\mathrm{m}$. This is a smaller saturation length with respect to the results of Fig.2.5 obtained with the non simplified model. This behaviour can be easily explained considering that in the original model the velocity $u(x)$ is greater in the zone where density is well below the saturated value. At the same density ρ, a larger velocity means a greater flight time T and hence a smaller impact rate $\Phi = \rho/T$. This in turn implies a smaller erosion rate $\Gamma = \Phi(n-1)$, and hence a longer saturation length.
Considering this effect, Sauermann *et al.* (2001) suggested to readjust the parameter γ which regulates the efficiency of erosion. They proposed the new value $\gamma = 0.2$ in order to get the saturation with the simplified model at the right time and position.
In Fig.2.7 we report a comparison between the full dynamics of the original model and the simplified model with the modified value of γ. Making the necessary simplification, we lost some interesting feature of the model such as the spatial overshoot in the flux profile, but the main feature such as the saturation length and time are reproduced in a satisfactory way. Moreover, we can now use the simplified model to simulate the
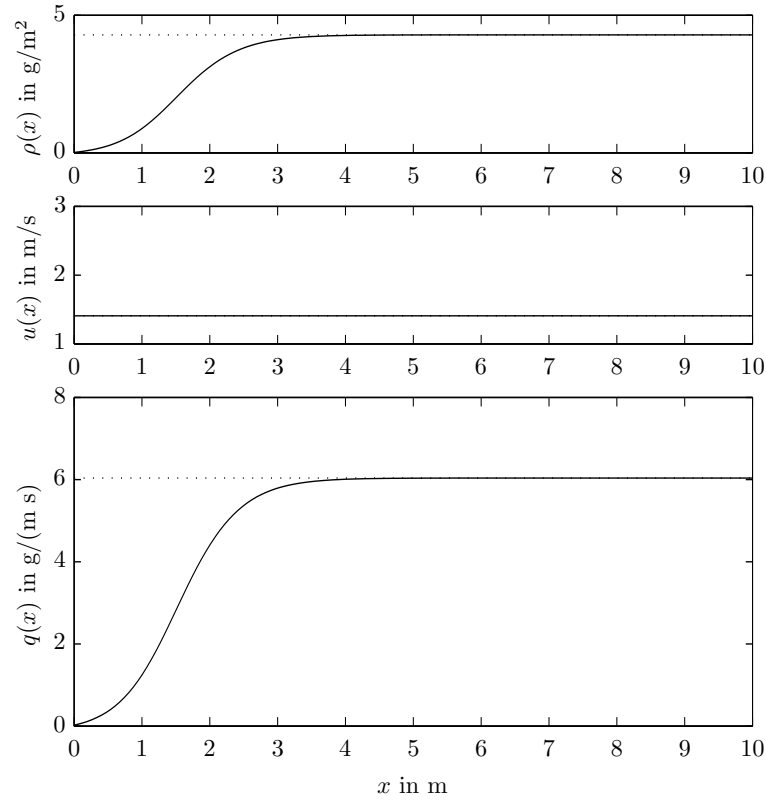
Figure 2.6: Stationary solution of the simplified saltation model for $u_* = 0.3\,\mathrm{m/s}$ - The saltation model is simplified approximating the effective wind velocity $v_{eff}(u_*, \rho)$ with the equilibrium value $v_{sat}(u_*)$. The other simulation conditions are the same of the results reported in Fig.2.5. We notice that the overshoot of the density profile has disappeared and that saturation in reached in a smaller distance.

saturation of the flux at higher shear velocity. The results of the stationary sand flux profile $q(x)$ for different values of the shear velocity u_* are represented in Fig.2.8(a). As u_* increases we notice that the length at which the flux saturates decreases, as we can see in Fig.2.8(b).
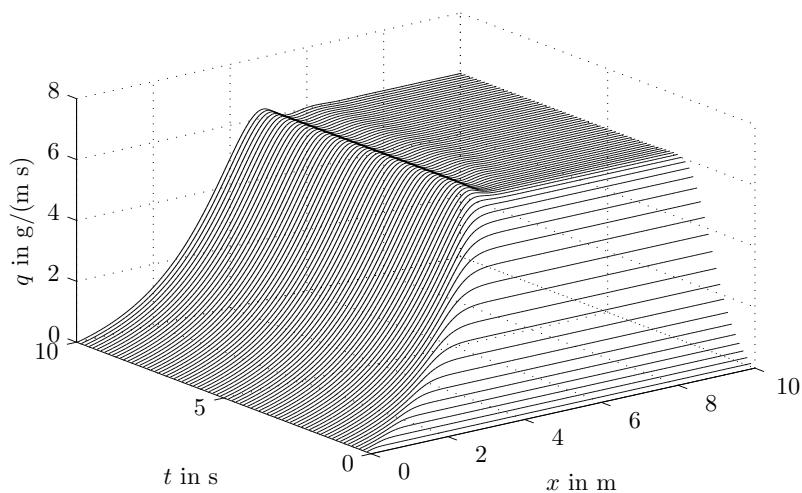
(a) $v_{eff}(\rho, u_*)$, $\gamma = 0.4$
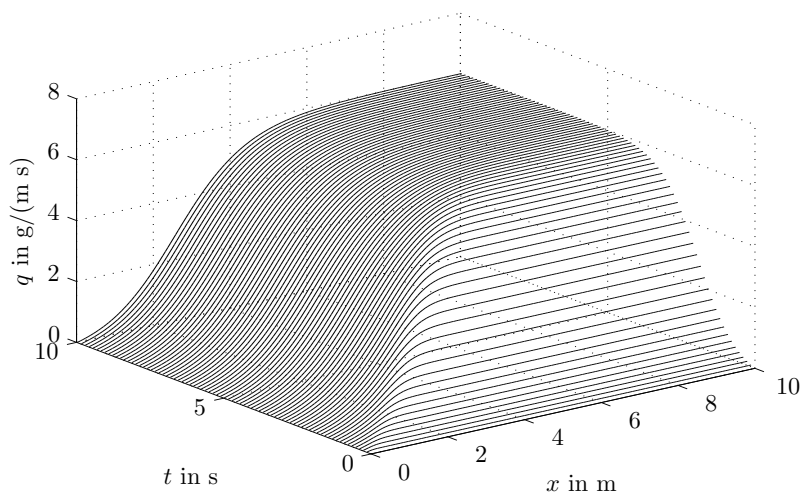
(b) $v_{sat}(u_*)$, $\gamma = 0.2$

Figure 2.7: Comparison between the complete and the simplified saltation model - The shear velocity is $u_* = 0.3\,\mathrm{m/s}$; in (a), the profiles of $q(x,t)$ obtained with the model (2.26)-(2.28) are plotted at different time interval. In (b), the same profiles are obtained with the simplified model changing the parameter γ.
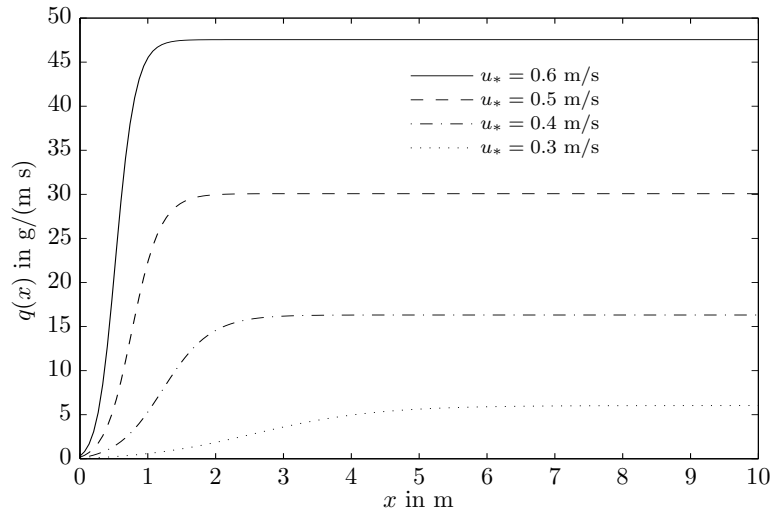
(a) Stationary solutions of the saltation model for different values of u_*
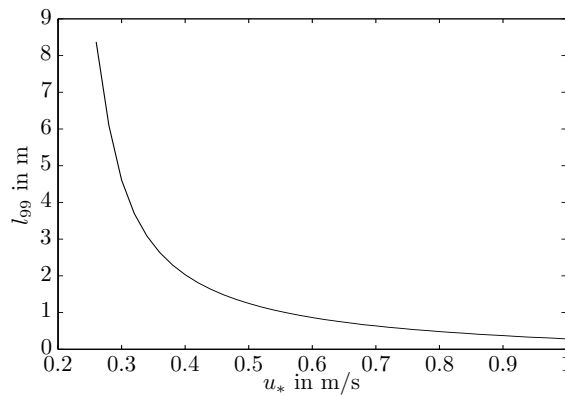
(b) Saturation length in function of the shear velocity.

Figure 2.8: Stationary solutions and saturation length - In (a) we report the stationary solution, obtained with the simplified model after changing the parameter $\gamma = 0.2$, for different values of the shear velocity. In (b) we plot how the saturation length $l_{99} = \{x : q(x) = 0.99 q_{sat}\}$ varies with u_*, and notice how in diverges near the threshold.

3

Dune evolution with marked sand

In this Chapter we develop a mathematical model for the evolution of dunes composed
by a mixture of sands with different characteristics. First, we introduce the model for
sand dunes evolution that, from the pioneering work on two-dimensional dunes of Kroy
et al. (2002), has been developed to successfully reproduce the full three-dimensional dy-
namics of barchan dunes (Schwämmle & Herrmann, 2005), their collisions (Schwämmle
et al., 2003; Durán *et al.*, 2005), the generation of vegetated parabolic dunes (Durán
& Herrmann, 2006b) and of linear dunes under non unidirectional wind (Parteli *et al.*,
2009), as well as the generation of complete dune fields (Durán *et al.*, 2011) and the
evolution of dunes on planet Mars (Parteli & Herrmann, 2007).

The dune model is introduced and analysed in its three dimensional formulation. Then,
we consider the mixture of sands with different characteristics. In particular, we con-
sider sands which can be distinguished only by their appearance, such as their colour,
but which have the same physical characteristics such as diameter and density. Hence
we will refer to "marked" and "clean" sands to distinguish the families of considered
sediments. These kinds of sediments are also known in the literature as "tracers" sedi-
ments.

Starting from one sediment transport model developed in the fluvial literature (Parker,
1991; Parker *et al.*, 2000) which considers the variety of granulometric classes which
composes the river bed, we develop a mathematical model which describes the evolution
of the concentration of marked sands in the sedimentary column during the evolution
of aeolian sand dunes.

3.1   Aeolian sand dune evolution

In this section we introduce the mathematical model for aeolian sand dune evolution,
first proposed in (Kroy *et al.*, 2002) in the two dimensional case and then improved in
the last decade, until the most updated three dimensional version reviewed in (Durán
et al., 2011).

The mathematical setting of the problem is the following. We describe the dynamics of
sand dunes in the three dimensional space by introducing the function h which describes

the height $z = h(x, y, t)$ of the sand surface at the position of horizontal coordinate x, y at instant t with respect to a reference height, usually taken at $z = 0$. Over the sand surface, if the shear stress exerted by the wind on the surface exceeds the threshold value $\tau_t = \rho_{air} u_{*t}^2$, the sand grains can be entrained and generate a flux of sand in saltation.

We consider the control volume $[x + \mathrm{d}x] \times [y + \mathrm{d}y] \times [0, +\infty)$ of infinite height and divide the total mass of sand in the control volume into a static part with mass distribution $\rho_0(x, y, z, t)$ and a saltation layer on top of it with mass distribution $\rho_1(x, y, z, t)$. If we make the hypothesis that the static part has a constant mass distribution given by $\rho_{dune} = (1 - \lambda)\rho_{sand}$, where λ is the porosity and $\rho_{sand} = 2650 \, \mathrm{Kg/m^3}$ is the characteristic density of a sand grain, we integrate along the vertical direction and define

$$ h(x, y, t) = \frac{1}{\rho_{dune}} \int_0^{+\infty} \rho_0 \, \mathrm{d}z \qquad \text{and} \qquad \rho(x, y, t) = \int_0^{+\infty} \rho_1 \, \mathrm{d}z, \qquad (3.1) $$

where $\rho(x, y, t)$ is the total mass in saltation in the control volume. Furthermore, if $\mathbf{q}_1(x, y, z, t)$ is the momentum distribution in the saltation layer, the integration along the vertical direction leads to the definition of the total horizontal momentum

$$ \mathbf{q}(x, y, t) = \int_0^{+\infty} \mathbf{q}_1 \, \mathrm{d}z. \qquad (3.2) $$

Consequently, the mean horizontal velocity is $\mathbf{u} = \mathbf{q}/\rho$.

The equation for conservation of mass can a priori be written separately for the static and the moving phase, including an exchange term between them, *i.e.*

$$ \frac{\partial \rho_i}{\partial t} + \nabla \cdot \mathbf{q}_i = \Gamma_i, \qquad i = 0, 1 \qquad (3.3) $$

where, for total mass conservation, the exchange terms must compensate, that is $\Gamma_1 = -\Gamma_0$. By definition of "static" part, $\mathbf{q}_0 = 0$ and hence, after integration along the vertical coordinate we obtain the conservation equations:

$$ \rho_{dune} \frac{\partial h}{\partial t} = -\Gamma, \qquad (3.4) $$

$$ \frac{\partial \rho}{\partial t} + \nabla \cdot \mathbf{q} = \Gamma, \qquad (3.5) $$

where Γ, which by definition is equal to $\int_0^{+\infty} \Gamma_1 \, \mathrm{d}z$, is in fact an exchange term localised at the interface between phases.

The Eqs.(3.4)-(3.5) express the physical consideration that the free surface h increases when sand grains are deposited from the saltation flux, and conversely decreases when sand grain are entrained in the flow.

We need to express the flux $\mathbf{q}(x, y, t)$ in terms of the height profile $h(x, y, t)$ and the action of external wind. The coupling between Eq.(3.4) and Eq.(3.5) involves two different time scales: the first is called T_h and is related to sand surface evolution, the second is called T_ρ and is related to sand transport. Considering that the typical order
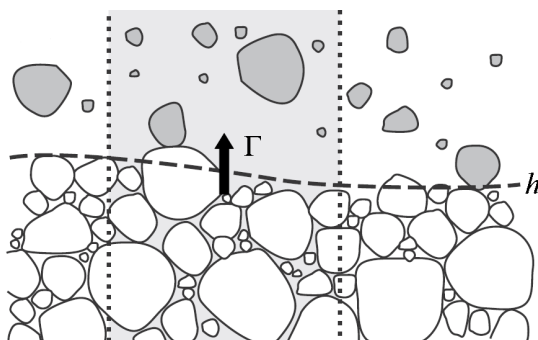
Figure 3.1: Definitions of the problem - The colours refer to moving (grey) and static (white) grains. Modified from (Durán *et al.*, 2011).

of magnitude of h and ρ are respectively $\mathcal{O}(1\,\text{m})$ and $\mathcal{O}(10^{-2}\,\text{Kg/m}^2)$, see *e.g.* Fig.2.4, we compare the two time scales:

$$\frac{T_h}{T_\rho} = \frac{\rho_{dune}\mathcal{O}(h)/\mathcal{O}(\Gamma)}{\mathcal{O}(\rho)/\mathcal{O}(\Gamma)} \sim \frac{\mathcal{O}(10^3\,\text{Kg/m}^3)\mathcal{O}(1\,\text{m})}{\mathcal{O}(10^{-2}\,\text{Kg/m}^2)} = \mathcal{O}(10^5). \qquad (3.6)$$

From this calculation we can infer that the two time scales are well separated. In particular, we see in Fig.2.4 that the sand flux saturates on a time scale $T_\rho \sim \mathcal{O}(1\,\text{s})$, and then from Eq.(3.6) we deduce that a significant change in sand surface can happen only within $T_h \sim \mathcal{O}(10^5\,\text{s}) = \mathcal{O}(1\,\text{d})$.

This separation of time scales allows us to decouple the different processes; the sand surface can be assumed to be stationary with respect to sand transport dynamics. This assumption allows us to calculate the flux $\mathbf{q}(x, y)$ by the following steps:

1. calculate the stationary wind velocity above the given topography; more precisely we need the shear stress $\boldsymbol{\tau}(x, y)$ exerted by the wind on the sand surface;

2. calculate the stationary sand flux $\mathbf{q}(x, y)$ for a given $\boldsymbol{\tau}(x, y)$.

For the second problem, we have already seen in Chap.2 how to model the sand flux in the horizontal case with homogeneous wind. We need to adapt these considerations to the three dimensional non homogeneous case.

3.1.1 Wind model: shear stress calculation

As shown in Chapter 2, the sand flux is determined by the shear velocity u_* which expresses the effect of shear stress exerted by the wind on the surface. We have also seen that the presence of the flux in saltation modifies the wind profile, which in the undisturbed case is logarithmic with shear velocity u_* and roughness z_0, into a piecewise logarithmic profile. Into the saltation layer the modified wind profile is characterized by a reduced shear velocity $u_{*a}(z)$ (equal to the threshold u_{*t} at saturation), and over

the saltation layer it feels the presence of the latter through an increased roughness z_0'. The wind is not only modified by the saltation sand flux, but also by the possible presence of a non flat topography profile $h(x, y)$. In principle, one can solve the Navier–Stokes equations with a turbulence model over the topography and then extract the necessary quantities at the surface. The problem of this type of calculation is its computational cost, which is excessively high for long time scale calculation such as the evolution of a dune. For this reason, following (Kroy *et al.*, 2002), we look for an analytical theory of logarithmic boundary layer perturbation which, thanks to the very low computational costs, is the preferred choice for our problem.

In particular, a dune can be considered as a perturbation of the flat surface that causes a modification of the air flow. If $\boldsymbol{\tau}_0 = \begin{pmatrix} \tau_0 \\ 0 \end{pmatrix}$ is the homogeneous shear stress on an undisturbed flat surface when the wind direction is aligned to the x axis, the actual shear stress $\boldsymbol{\tau}(x, y)$ on the non flat surface $h(x, t)$ is written in the form

$$\boldsymbol{\tau}(x,y) = \tau_0 \begin{pmatrix} 1 + \delta\tau_x(x,y) \\ \delta\tau_y(x,y) \end{pmatrix} \tag{3.7}$$

where $\delta\tau_x$ and $\delta\tau_y$ are the non dimensional shear stress perturbations in x and y directions.

An analytical theory of logarithmic boundary layer perturbation onto a two dimensional hill of small aspect ractio has been first developed by Jackson & Hunt (1975). Later, the work has been refined (Sykes, 1980; Zeman & Jensen, 1987; Hunt *et al.*, 1988), extended to three dimensional hills (Mason & Sykes, 1979) and finally adapted to sand dunes (Weng *et al.*, 1991; Kroy *et al.*, 2002; Schwämmle & Herrmann, 2005).

The following discussion is mainly based on (Hunt *et al.*, 1988). The analytical perturbation model is built considering a hill with moderate slope with height H, length $2L$ at half height and roughness z_0, and is valid when $H/L \ll 1$ and $\ln(L/z_0) \gg 1$. It is based on the subdivision of the air flow over the hill into an inviscid outer region and a thin inner region of height l. Each of these regions is furthermore subdivided into two sublayers, and in each one of the four layers the flow is determined separately considering the prevailing physical processes. Finally, the solutions in the four regions are matched together and the complete flow is obtained.

For our purposes, the most important results of the analytical model is the shear stress perturbations at the ground which is written in term of Fourier transform (Weng *et al.*, 1991) as:

$$\mathcal{F}[\delta\tau_x](\mathbf{k}) = \frac{2}{U^2(l)} \frac{k_x^2}{(k_x^2 + k_y^2)^{1/2}} \left(1 + \frac{2\ln L|k_x| + 4\epsilon + 1 + i\,\mathrm{sign}(k_x)\pi}{\ln(l/z_0^{dune})} \right) \mathcal{F}[h](\mathbf{k}) \tag{3.8}$$

$$\mathcal{F}[\delta\tau_y](\mathbf{k}) = \frac{2}{U^2(l)} \frac{k_x k_y}{(k_x^2 + k_y^2)^{1/2}} \mathcal{F}[h](\mathbf{k}), \tag{3.9}$$

where $\mathcal{F}[\cdot](\mathbf{k})$ denotes the Fourier transform with wave vector $\mathbf{k} = (k_x, k_y)$ and $\epsilon = 0.577216$ is the Euler's constant. The constant $U(l)$ is the dimensionless velocity of

the undisturbed logarithmic profile of Eq.(2.2) at height l, where l is the height of the inner layer of the flow. The velocity $U(l)$ is made dimensionless by scaling it by the velocity at the reference height h_m that separates the middle and upper layer of the flow. Therefore, we obtain the logarithmic wind profile

$$U(l) \equiv \frac{V_0(l)}{V_0(h_m)} = \frac{\ln(l/z_0^{dune})}{\ln(h_m/z_0^{dune})}.$$ (3.10)

Here, both l and h_m are computed from the implicit equations

$$l \ln(l/z_0^{dune}) = 2\kappa^2 L$$ (3.11)

$$h_m^2 \ln(h_m/z_0^{dune}) = L^2.$$ (3.12)

The last parameter of the model is the roughness z_0^{dune} of the dune surface. We have
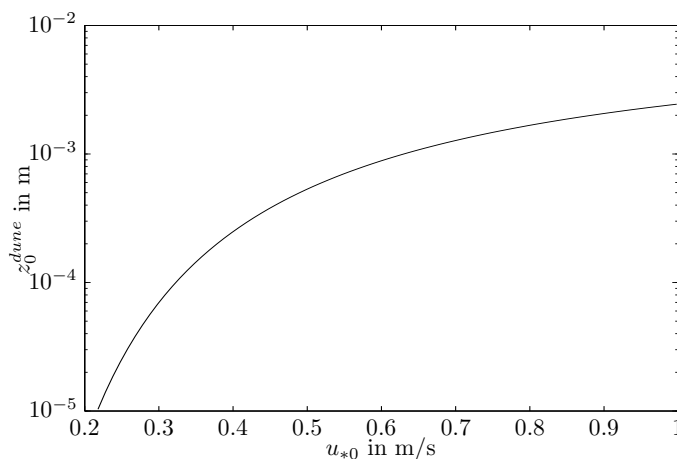
Figure 3.2: Apparent roughness - Roughness z_0^{dune} used in the shear stress calculation as a function of the undisturbed shear velocity u_{*0}.

seen in Chapter 2 that in the undisturbed case the roughness of a sandy surface without saltation layer is typically $z_0 = 10\,\mu$m, whereas if the saltation layer is present the roughness changes to the apparent value $z_0' = z_0 \exp\left[\left(1 - \frac{u_{*a0}}{u_*}\right) b_\infty\right]$ given in Eq.(2.20), where the residual shear velocity u_{*a0} depends on the density ρ of the saltation flux through Eq.(2.23). Over the topography $h(x,y)$ both u_* and ρ depends on the space coordinates, hence the apparent roughness is in general not constant in space: $z_0' = z_0'(x,y)$. The situation is complicated by the fact that up to now $u_*(x,y)$ is still unknown.

These considerations contrast with the analytical theory of boundary layer perturbation which assume that the roughness of the dune surface z_0^{dune} is constant. Hence we must choose a priori an effective value for the roughness to be used in the wind model. If $u_{*0} = \sqrt{\tau_0/\rho_{air}}$ is the undisturbed shear velocity on a flat surface, we choose

$$z_0^{dune} = z_0 \exp\left[\left(1 - \frac{u_{*t}}{u_{*0}}\right) b_\infty\right],$$ (3.13)

which is the apparent roughness of a saturated sand flux for the shear velocity u_{*0}. The value $b_\infty \simeq 7$ is obtained from Eq.(2.21). In Fig.3.2 we see that the apparent roughness can increase of two orders of magnitude for typical values of the shear velocity. The value $z_0^{dune} = 1\,\text{mm}$ used by Parteli *et al.* (2009) is well within the range of the results of Eq.(3.13). Moreover, we notice that z_0^{dune} appears in Eqs.(3.8)–(3.12) only as logarithmic factor, hence the coefficients change very little with a varying z_0^{dune}.

Notwithstanding Eqs.(3.8)-(3.9) seem to be of difficult interpretation, the results of the application to a simple case can clarify the overall behaviour of this analytic wind model.

Example   We consider the Gaussian profile $h(x,y) = H \exp\left(-\left(\frac{x-x_0}{\sigma}\right)^2 - \left(\frac{y}{\sigma}\right)^2\right)$ with $H = 1\,\text{m}$, $x_0 = 50\,\text{m}$ and σ chosen such that $L = 10\,\text{m}$. For a typical undisturbed shear velocity $u_{*0} = 0.5\,\text{m/s}$, the Eq.(3.13) gives $z_0^{dune} \simeq 0.5\,\text{mm}$, and the hypothesis of validity of the model $H/L = 0.1 \ll 1$ and $\ln(L/z_0) \simeq 10 \gg 1$ are satisfied.
The Eqs.(3.11)-(3.12) gives $l = 0.47\,\text{m}$ and $h_m = 3.38\,\text{m}$ respectively, hence from Eq.(3.10) we obtain $U = 0.775$.
In Fig.3.3(a) we notice that the shear stress perturbation in the horizontal direction $\delta\tau_x$ is not symmetric even if the topography h represented in Fig.3.3(c) is symmetric. It has a maximum shifted upwind with respect to the maximum of h, and two minima, with the one on the downwind part of the hill more pronounced than the one on the upwind part. See also the trend $\delta\tau_x(x,0)$ on the central section $h(x,0)$, represented in Fig.3.3(d).
The shear stress perturbation on the lateral direction $\delta\tau_y$ represented in Fig.3.3(b) is antisymmetric with respect to the symmetry center of h. We also compare the orders of magnitude of the shear stress perturbations: $\delta\tau_x \in [-0.15, 0.35]$ and $\delta\tau_y \in [-0.08, 0.08]$, and deduce that in the lateral direction the perturbation is small but not negligible.

During evolutionary calculations of sand dune profile the typical length of the dune L changes. Following Durán (2007), it can be calculated during the iterations as the mean wavelength of the Fourier representation of the height profile:

$$L \equiv \frac{1}{\langle k_x \rangle} = \frac{\int_0^\infty |\mathcal{F}[h](\mathbf{k})|\,\mathrm{d}\mathbf{k}}{\int_0^\infty k_x |\mathcal{F}[h](\mathbf{k})|\,\mathrm{d}\mathbf{k}}.$$

By inserting the inverse Fourier transform of Eq.(3.8)-(3.9) in Eq.(3.7) we obtain the profile of the modified shear stress $\boldsymbol{\tau}(x,y)$, or equivalently the profile of the perturbed shear velocity

$$\mathbf{u}_*(x,y) = u_*(x,y)\mathbf{e}_{\boldsymbol{\tau}}(x,y),$$

where the unit vector $\mathbf{e}_{\boldsymbol{\tau}} \equiv \boldsymbol{\tau}/|\boldsymbol{\tau}|$ defines the wind direction at the surface and the perturbed shear velocity is

$$u_*(x,y) = \sqrt{|\boldsymbol{\tau}|/\rho_{air}} = u_{*0} \sqrt[4]{(1 + \delta\tau_x)^2 + \delta\tau_y^2}$$

(a) Shear stress perturbation $\delta\tau_x(x,y)$

(b) Shear stress perturbation $\delta\tau_y(x,y)$

(c) Smooth hill $h(x,y)$

(d) $\tau_x(x,0)/\tau_0$ on the central section $h(x,0)$
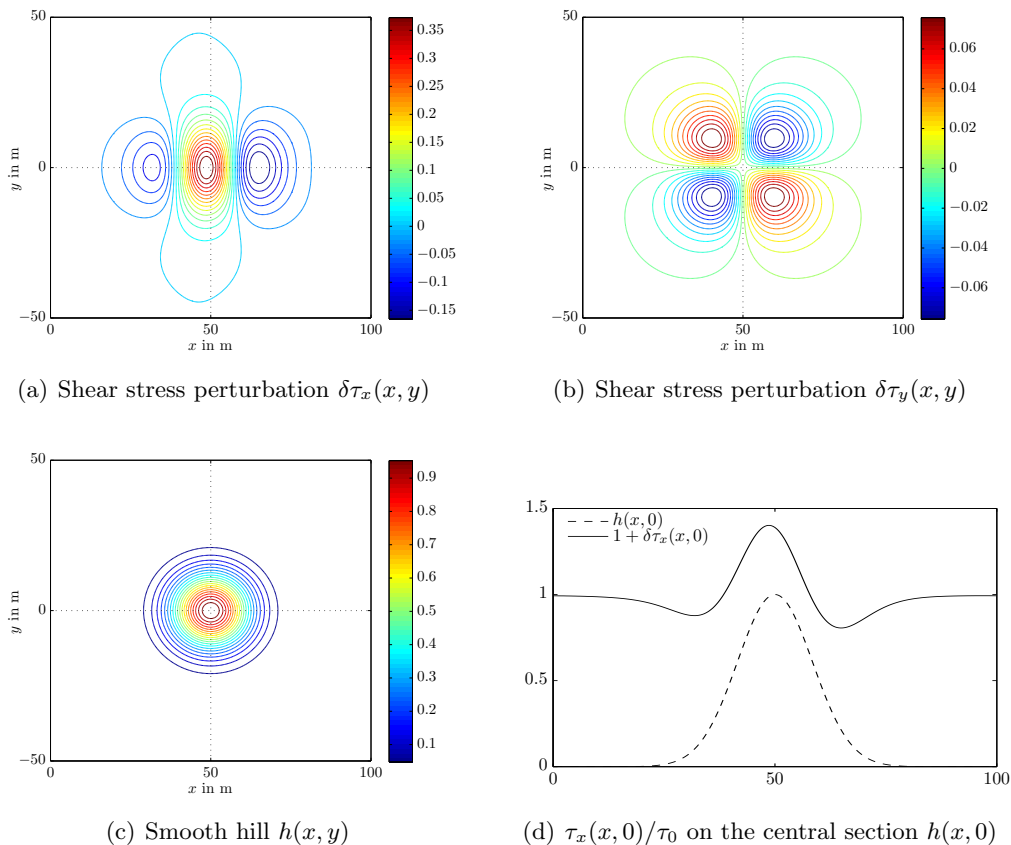
Figure 3.3: Shear stress perturbation over a gaussian hill - The wind blows from the left; in (a) and (b) are represented the obtained dimensionless shear stress perturbations on the topography profile (c). The horizontal shear stress perturbation on the central slice of the hill is represented in (d).

Separation bubble

The analytical theory of logarithmic boundary layer perturbation introduced so far is only valid for smooth surfaces. In particular, this theory does not include nonlinear effects like flow separation. However, the shape of sand dunes often includes a sharp brink where the wind streamlines separates from the surface. This phenomenon creates a recirculating zone in the lee side of the dune, called also recirculation bubble, which cannot be modelled by the analytical perturbation method. Nevertheless, the strength of the recirculating wind in the separation bubble is too small to dislodge and entrain sand grains in saltation. Hence, we can avoid the accurate description of the wind flow in the recirculating zone, and adapt heuristically the analytical model to the case of recirculating flows.

In particular, following (Kroy *et al.*, 2002), we can empirically reconstruct the surface that contains the recirculation bubble and assume that the wind follows it as a

solid surface. Hence, we calculate the shear stress perturbations using the analytical theory of Eq.(3.8)-(3.9) over an ideal smooth surface which include the surface of the dune and the separation bubble. In this way, from the one hand we are apparently introducing an error by treating the separation bubble like a solid surface where the wind velocity decreases to zero. On the other hand, we can expect that if the separating surface joins smoothly the dune surface, the calculated shear stress profile is smooth too and the errors in the shear stress over the windward dune surface are small.

Let's first formalize these considerations in the two dimensional case, where $h(x)$ is the sand surface profile and the recirculation bubble is enclosed in the separating streamline $s(x)$.
The simplest mathematical function that can be used to empirically reconstruct a smooth separating streamline is a third order polynomial. In fact, we require at least a continuous junction with continuous derivative at detachment and at reattachment points; these are four conditions that determine a unique third order polynomial. If the detachment point is well determined by the geometry of the dune *i.e.* the point of discontinuity of the derivative of $h(x)$, the reattachment point is still undetermined. Following Sauermann (2001), we find the reattachment point by imposing that the separating streamline has a fixed maximum negative slope of 14. This value is taken after experimental evidence that a turbulent boundary layer detaches at angle larger than 14, and then it is assumed as the upper limit of validity of the analytical perturbation model.
Separation can occur on smooth profiles too. Hence we suppose that if a profile has negative slope which exceeds 14, in this point the flow separates and from the detachment point we build the empirical separating streamline.
The results of this heuristic procedure are shown in Fig.3.4; in Fig.3.4(a), $h(x)$ is the profile of a hill with negative slope greater than 14. In Fig.3.4(b), $h(x)$ is the idealized profile of a dune with a slipface. The two profiles are used to build the polynomial separating streamline $s(x)$ with the described procedure. Then, the analytical perturbation model of Eqs.(3.7)-(3.8) is applied on the smooth surface defined by $\max(h(x), s(x))$ to find the ideal shear stress profile $\tau_s(x)$ given in Fig.3.4(c)-3.4(d). Finally, for the purpose of sand transport calculation, inside the recirculation bubble, where $s(x) > h(x)$, we fix $\tau(x) = 0$, because in this zone the superficial shear stress is too small to keep a saltation flux.

In the three dimensional case, the reconstruction of the surface which includes the recirculation bubble is made by following the procedure of the two dimensional case for each section of the domain parallel to the wind direction (Durán, 2007; Parteli, 2007). Hence, for each fixed lateral coordinate $\bar{y}$, the separating streamline $s(x, \bar{y})$ is a third order polynomial with smooth junction with $h(x, \bar{y})$ at brink and reattachment point. In Fig.3.5 we report the results of the procedure on a test case consisting in a gaussian hill cut with an inclined plane. We notice that on the windward side, the shear stress is smooth, similar to the profile obtained with the Gaussian hill in Fig.3.3. As in the two
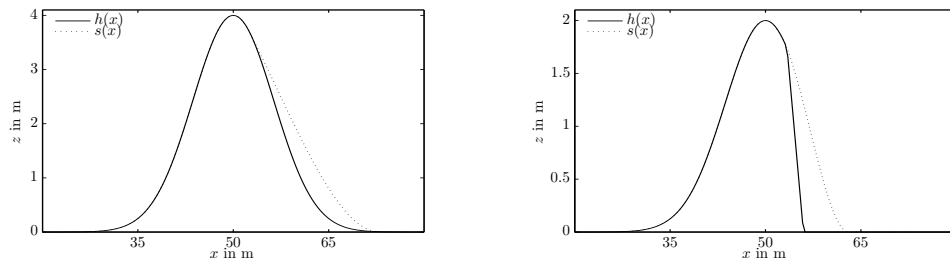
(a) Smooth profile $h(x)$ and separating streamline $s(x)$

(b) Dune profile with slip face $h(x)$ and separating streamline $s(x)$
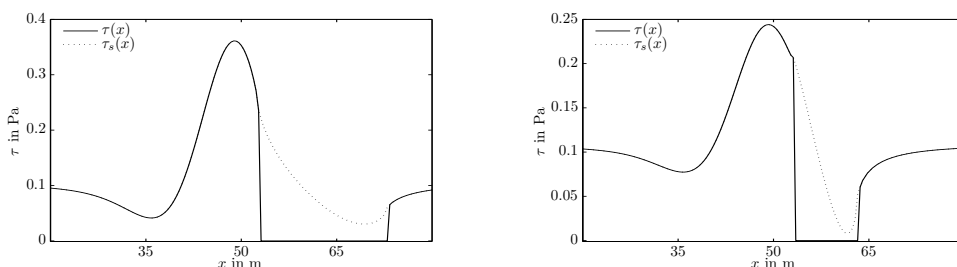
(c) Shear stress $\tau_s(x)$ calculated on the separating streamline and then neglected in the recirculation zone $\tau(x)$ for the smooth profile

(d) Shear stress $\tau_s(x)$ calculated on the separating streamline and then neglected in the recirculation zone $\tau(x)$ for the dune profile

Figure 3.4: Shear stress calculation on profiles with separation - In (a), the profile $h(x)$ has negative slope steeper than 14. In (b), the profile of the dune $h(x)$ presents a slope discontinuity at the brink between the windward side and the slip face. At the detachment point, the separating streamline $s(x)$ starts with smooth junction with $h(x)$ and reattaches downwind with smooth junction too. In (c) and (d), the shear stress $\tau_s(x)$ is calculated on the smooth surface $\max(h(x), s(x))$, and then inside the recirculating zone $\tau(x)$ is neglected and hence fixed to 0. In these examples the undisturbed shear velocity is $u_{*0} = 0.3\,\mathrm{m/s}$.

dimensional case, in the recirculation zone the shear stress is intentionally neglected ($\boldsymbol{\tau} = 0$).

3.1.2 Three dimensional sand transport model

The previous Section provides us a model for the calculation of the stationary shear stress field $\boldsymbol{\tau}(x, y)$ over a given topography $h(x, y)$, even in the case of topography with discontinuities in the slope as in the case of dunes with slipface. Now we need to calculate the sand flux $\mathbf{q}(x, y)$ transported by the wind which regulates the erosional dynamic of the sand surface through the system of conservation equations (3.4)-(3.5). As already introduced in Section 3.1, the horizontal flux of sand in saltation $\mathbf{q}(x, y)$ can be described by its density $\rho(x, y)$ and velocity $\mathbf{u}(x, y)$, where these variables are to be intended as obtained after vertical integration of the corresponding three dimensional
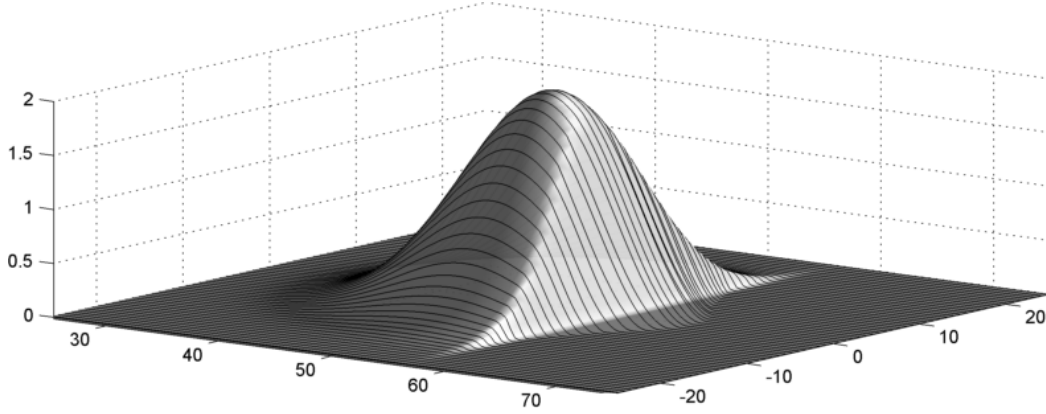
(a) Profile $h(x, y)$ with slope discontinuity and reconstructed polynomial separating streamlines.
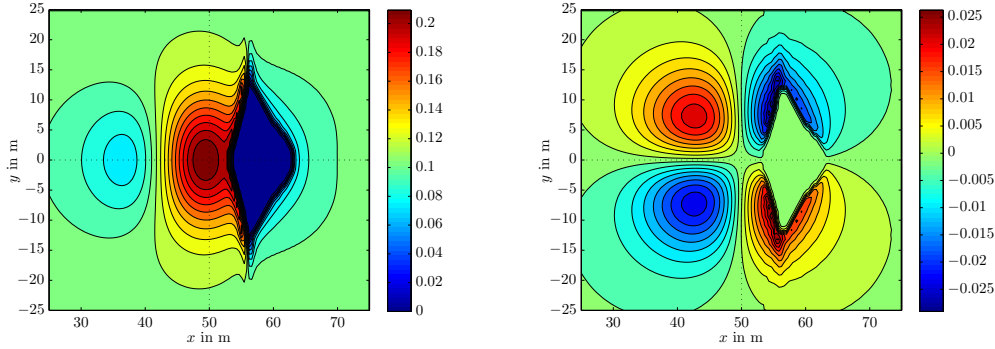
(b) Horizontal shear stress $\tau_x(x, y)$

(c) Lateral shear stress $\tau_y(x, y)$

Figure 3.5: Three dimensional recirculation bubble reconstruction - The surface $h(x, y)$ is a gaussian hill cut with an inclined plane (a). The surface which includes the recirculation bubble is build with a third order polynomial in each horizontal section. In (b) and (c), the shear stresses $\tau_x(x, y)$ and $\tau_y(x, y)$ are calculated on the smooth surface $\max(h(x, y), s(x, y))$, and then inside the recirculating zone both $\tau_x(x, y)$ and $\tau_y(x, y)$ are fixed to 0. This procedure leads to a smooth shear stress field on the windward side of the hill. In this example the undisturbed shear velocity is $u_{*0} = 0.3 \, \text{m/s}$.

distribution, see Eqs.(3.1)-(3.2). The comparison between the time scales related to the evolution of the sand surface and the saltation flux allows us to neglect the temporal variation of the latter and hence consider only the stationary solution of the equations for ρ and $\mathbf{u}$.

We have already presented in Section 2.2 a continuum model for the saltation flux in the case of a horizontal sandy surface blown by an homogeneous wind. Here we only need to adapt these considerations to the three dimensional non homogeneous case. In the stationary mass conservation equation

$$\nabla \cdot \mathbf{q} = \Gamma,$$

the rate of exchange of sediment with the static phase $\Gamma(x,y)$ is linked to two distinct phenomena: the balance between the number of impacting and splashed grains $\Gamma_i(x,y)$, which can be either negative or positive, and the number of grains directly entrained by the wind $\Gamma_a(x,y)$, which is a positive value. We need also to consider that Γ can be strictly positive, *i.e.* we erode sediments from the sand surface, only if sand grains are available in the static phase, *i.e.* if $h > 0$.

In view of the application we have in mind, the most convenient form to write the balance Γ_i is:

$$\Gamma_i = \frac{\rho}{T}\,(n-1) \tag{3.14}$$

where we recall from Section 2.2.1 that

$$T(x,y) = \frac{2\alpha}{g}\frac{|\mathbf{u}|}{r} \tag{3.15}$$

is the flight time, ρ/T is the impact rate and

$$n(x,y) = 1 + \tilde{\gamma}\left(\frac{|\boldsymbol{\tau}| - \tau_{g0} - \tau_t}{\tau_t}\right) \tag{3.16}$$

is the number of ejected grains for one impacting grain. Notice that with respect to the calculation of Section 2.2.1, we are in the three dimensional non homogeneous case and hence in Eqs.(3.15)-(3.16) we must use the magnitude of the flux velocity $|\mathbf{u}(x,y)|$ and of the shear stress $|\boldsymbol{\tau}(x,y)|$.

From Eq.(2.16), the direct aerodynamic entrainment rate $\Gamma_a(x,y)$ takes the form

$$\Gamma_a = \max\left(\gamma_a\frac{|\boldsymbol{\tau}| - \tau_{g0} - \tau_{ta}}{\tau_{ta}}, 0\right) \tag{3.17}$$

where in both Eqs.(3.16)-(3.17) the grain born shear stress $\tau_{g0}(x,y)$ is

$$\tau_{g0} = \frac{g}{2\alpha}\rho(x,y)$$

as derived in Eq.(2.10). Finally, the global exchange term between the static and the moving phase is:

$$\Gamma = \begin{cases} \Gamma_i + \Gamma_a & \text{if } h(x,y) > 0, \\ \min(\Gamma_i, 0) & \text{if } h(x,y) = 0, \end{cases} \tag{3.18}$$

which takes into account the consideration that on the unerodible surface $h = 0$, the direct aerodynamic entrainment is null ($\Gamma_a = 0$) and the sand grain in the moving phase can only rebound or deposit ($n \leq 1$), so that only net deposition can occur.

The stationary momentum conservation equation in the three dimensional case is:

$$\rho\mathbf{u}\cdot\nabla\mathbf{u} = \mathbf{f}_{drag} + \mathbf{f}_{bed} + \mathbf{f}_{grav},$$

where now, on sloped surfaces, with respect to Eq.(2.12) we must add the gravitational force $\mathbf{f}_{grav}(x, y)$, directed towards the direction of steepest descent of h:

$$\mathbf{f}_{grav} = -\rho g \boldsymbol{\nabla} h(x, y). \tag{3.19}$$

The drag force becomes:

$$\mathbf{f}_{drag} = \rho g \frac{|\mathbf{v}_{eff} - \mathbf{u}|(\mathbf{v}_{eff} - \mathbf{u})}{u_f^2} \tag{3.20}$$

where, from the definitions of Eq.(2.22), Eq.(2.30) and the simplification of Section 2.3:

$$\mathbf{v}_{eff}(x, y) = \frac{u_{*t}}{\kappa} \left[\ln \frac{z_1}{z_0} + \frac{z_1}{z_m} \left(\frac{u_*(x, y)}{u_{*t}} - 1 \right) \right] \mathbf{e}_{\boldsymbol{\tau}}(x, y) \tag{3.21}$$

is the effective wind velocity (aligned with $\boldsymbol{\tau}$) responsible for the acceleration of the saltation layer.

Finally, the friction force is aligned with the velocity vector $\mathbf{u}$:

$$\mathbf{f}_{bed}(x, y) = -\frac{\rho g}{2\alpha} \frac{\mathbf{u}}{|\mathbf{u}|}. \tag{3.22}$$

In conclusion, the system:

$$
\begin{cases}
\rho_{dune} \dfrac{\partial h}{\partial t} = -\Gamma, \\[2.5ex]
\nabla \cdot (\rho \mathbf{u}) = \Gamma, \\[2.5ex]
\rho \mathbf{u} \cdot \nabla \mathbf{u} = \mathbf{f}_{drag} + \mathbf{f}_{bed} + \mathbf{f}_{grav},
\end{cases}
\tag{3.23}
$$

constitutes the closed model for dune evolution. We need to provide an initial condition for the topography $h(x, y, 0)$ and boundary conditions for the density ρ and velocity $\mathbf{u}$ of the saltation flux. The input parameter of the model is the undisturbed shear stress τ_0 which, through Eq.(3.7), determines the intensity of the shear stress field $\boldsymbol{\tau}(x, y)$ during the evolution of the surface and hence the dynamics of the whole system.

At this point, we still need to consider that sand avalanches can develop on the sand surface if the slope exceeds the angle of repose of the sediments. This physical mechanism will be discussed in Section 3.3. First we will build a model for the evolution of sand dune formed by a mixture of sands.

3.2 Marked sand transport

As already stated in the beginning of this Chapter, we consider a mixture of sands which can be distinguished only by their appearance, such as their colour, but which have the same physical characteristics such as diameter and density. We will consider two

families of sediments, hence from now on we will refer to "marked" and "clean" sands to distinguish the considered sediments. The first step is deriving the conservation equation for the mass of marked sand in the static and the moving phase, analogously of what have been done in Section 3.1.

Let $\tilde{\rho}_0(x,y,z,t)$ and $\tilde{\rho}_1(x,y,z,t)$ be the mass distribution of marked sand in the static and moving phase respectively. The equations for conservation of mass of marked sand are

$$\frac{\partial \tilde{\rho}_i}{\partial t} + \nabla \cdot \tilde{\mathbf{q}}_i = \tilde{\Gamma}_i, \qquad i = 0, 1 \tag{3.24}$$

where $\tilde{\mathbf{q}}_1(x,y,z,t)$ is the momentum distribution of the moving phase, by definition of static phase $\tilde{\mathbf{q}}_0 = 0$ and for total mass conservation the exchange terms must compensate: $\tilde{\Gamma}_1 = -\tilde{\Gamma}_0$.

We define now the total mass and momentum of marked sand in the moving phase in a vertical infinite control volume:

$$\tilde{\rho}(x,y,t) = \int_0^{+\infty} \tilde{\rho}_1 \, \mathrm{d}z \qquad \text{and} \qquad \tilde{\mathbf{q}}(x,y,t) = \int_0^{+\infty} \tilde{\mathbf{q}}_1 \, \mathrm{d}z,$$

integrating Eq.(3.24) for the moving phase ($i = 1$) along the vertical direction. We obtain the conservation equation for the mass of marked sand in the saltation layer:

$$\frac{\partial \tilde{\rho}}{\partial t} + \nabla \cdot \tilde{\mathbf{q}} = \tilde{\Gamma}. \tag{3.25}$$

where, as usual, the vertically integrated exchange term $\tilde{\Gamma}$ is in fact localised at the interface between static and moving phase.

Now we notice that, from the hypothesis of constant porosity which lead also to Eq.(3.1), the marked mass distribution in the static phase can be defined as

$$\tilde{\rho}_0(x,y,z,t) = \begin{cases} \rho_{dune}\tilde{f}(x,y,z,t) & \text{if } z \le h(x,y,t), \\ 0 & \text{otherwise}, \end{cases}$$

where $\tilde{f}$ is the concentration of marked sand in the static phase. At this point, the integration along the vertical direction of Eq.(3.24) for the static phase ($i = 0$) leads to

$$\rho_{dune}\frac{\partial}{\partial t}\int_0^{h(x,y,t)} \tilde{f} \, \mathrm{d}z = -\tilde{\Gamma}. \tag{3.26}$$

The coupled conservation equations (3.25)-(3.26) are not in a closed form yet. In fact, the exchange rate $\tilde{\Gamma}$ is still unknown. Moreover, the integral in (3.26) extends to a moving boundary. In the following, we introduce a modelling framework that allows us to write the problem in a convenient form suitable for numerical simulation.

3.2.1 The active layer setting

Here we adopt some hypothesis that simplify the conservation equation for mass of marked sand in the static phase Eq.(3.26). In particular, in order to derive a closed
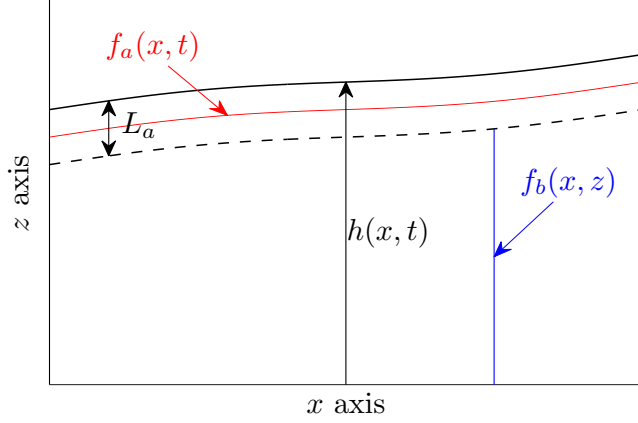
Figure 3.6: The active layer framework - In the active layer, the marked sand concentration $f_a(x,t)$ does not depend on the vertical coordinate z; in the substrate, the marked sand concentration $f_b(x,z)$ does not change in time.

form for the exchange rate $\tilde{\Gamma}$, we need to distinguish the more superficial zone of the sedimentary column from the deep substrate. This kind of distinction is often made in fluvial literature, in particular in sediment transport models which consider the mixture of granulometric classes composing the river bed. In particular, we adapt to our problem the *active layer* framework encountered in (Parker, 1991; Hoey & Ferguson, 1994; Armanini, 1995; Parker *et al.*, 2000). More precisely, we formulate the following assumptions, see Fig.3.6:

1. the static phase exchanges sediments with the moving phase in a superficial layer of finite thickness L_a, named *active layer*;

2. the active layer is well mixed by the exchange process so that it has no vertical structure. Therefore we define:

$$\tilde{f}(x,y,z,t) = f_a(x,y,t) \quad \text{if} \quad h - L_a < z < h;$$

3. the substrate has a vertical structure, and thus a functional dependence in z, but it does not change in time because it is below the zone that exchanges sediments with the moving phase:

$$\tilde{f}(x,y,z,t) = f_b(x,y,z) \quad \text{if} \quad z < h - L_a.$$

These hypotheses allow us to write Eq.(3.26) separately for the active layer and the substrate:

$$\rho_{dune} \frac{\partial}{\partial t} \int_{h(t)-L_a}^{h(t)} f_a(x,y,t)\,\mathrm{d}z + \Phi = -\tilde{\Gamma} \qquad (3.27)$$

$$\rho_{dune} \frac{\partial}{\partial t} \int_{0}^{h(t)-L_a} f_b(x,y,z)\,\mathrm{d}z - \Phi = 0, \qquad (3.28)$$

where the new term $\Phi(x,y,t)$ is the exchange rate of mass of marked sand through the internal surface $z = h(x,y,t) - L_a$ separating the active layer and the substrate. If the sand surface is locally in erosion ($\partial_t h < 0$), the active layer incorporates sediments from the substrate, and the interface mass rate will be $\Phi = \rho_{dune} f_b\big|_{z=h-L_a} \partial_t(h - L_a)$. Otherwise, if the sand surface is locally in deposition ($\partial_t h > 0$), the active layer passes sediments to the substrate, and the interface mass rate will be $\Phi = \rho_{dune} f_a \partial_t(h - L_a)$. These considerations can be incorporated in the definition of the interface concentration:

$$f_I = \begin{cases} f_b\big|_{z=h-L_a} & \text{if } \partial_t h < 0, \\ f_a & \text{if } \partial_t h \geq 0, \end{cases} \qquad (3.29)$$

which allows us to write Eq.(3.27) in the compact form:

$$\rho_{dune} \left[\frac{\partial(L_a f_a)}{\partial t} + f_I \frac{\partial(h - L_a)}{\partial t} \right] = -\tilde{\Gamma}. \qquad (3.30)$$

The conservation equation (3.30) states that the temporal variation of the mass of marked sand in the active layer is linked to the amount of marked sand which enters (leave) the active layer through the internal interface with the substrate in erosion (deposition) processes and to the exchange of sediment with the moving phase.
On the other hand, the marked sand conservation equation (3.28) in the substrate becomes:

$$f_b(x,y,h(\bar{t}) - L_a) = f_a(x,y,\bar{t}) \quad \text{when } \partial_t h > 0 \qquad (3.31)$$

which expresses the fact that the substrate marked sand concentration at the vertical coordinate $\bar{z}$ is the active layer concentration $f_a(\bar{t})$ at time $\bar{t} : \bar{z} = h(\bar{t}) - L_a$ of passage of the interface through the point $\bar{z}$. This modelling framework hence constitutes an efficient strategy to track the history of marked sand concentration in the sedimentary column through depositional processes.

Now we provide a closed form for $\tilde{\Gamma}$, the exchange term which describes the mass of marked sand passing from the static to the moving phase over a surface of unit area in the unit time. First, it is useful to rewrite $\tilde{\rho} = f_t \rho$, where $f_t(x,y,t)$ is the concentration of marked sand in the moving phase.
We recall that the global exchange rate Γ given in Eq.(3.18) is composed of two terms: the direct aerodynamic entrainment rate Γ_a and the impact-ejection balance Γ_i; this

partition of course holds also when we consider the exchange rate for the marked sand:

$$\tilde{\Gamma} = \tilde{\Gamma}_i + \tilde{\Gamma}_a.$$

The mass of marked sand entrained directly by the wind $\tilde{\Gamma}_a$ is proportional to the global entrainment rate Γ_a times the concentration of marked sand in the active layer:

$$\tilde{\Gamma}_a = f_a \Gamma_a.$$

The exchange of marked sand due to the impact-ejection balance $\tilde{\Gamma}_i$ is more difficult to determine. We recall that the global impact-ejection balance Γ_i is given in Eq.(3.14). What we need in the following is to write Γ_i as a balance between the entrainment $E(x, y, t)$ and deposition $D(x, y, t)$ rates of sand:

$$\Gamma_i = E - D, \tag{3.32}$$

where, by definition, the entrainment (deposition) rate is the mass of sand which passes from the static (moving) to the moving (static) phase over a unit area in the unit time. In fact, an immediate consequence of Eq.(3.32) is writing the analogous for the balance of marked sand:

$$\tilde{\Gamma}_i = \tilde{E} - \tilde{D} = f_a E - f_t D, \tag{3.33}$$

where we have specified that the entrainment rate of marked sand $\tilde{E}(x, y, t)$ is proportional to the global entrainment rate $E(x, y, t)$ times the concentration of marked sand in the active layer $f_a(x, y, t)$, and that the deposition rate of marked sand $\tilde{D}(x, y, t)$ is proportional to the global deposition rate $D(x, y, t)$ times the concentration of marked sand in the moving phase $f_t(x, y, t)$.
In the global impact-ejection balance Γ_i given in Eq.(3.14), the number of ejected grains for each impacting grain n includes the rebounding grain. Hence, if we know the probability p_{reb} that an impacting grain rebound we can define:

$$D = \frac{\rho}{T} \left(1 - p_{reb}\right) \qquad \text{and} \qquad E = \frac{\rho}{T} \left(n - p_{reb}\right)$$

and close the problem. The characterization of p_{reb} is a really hard problem. In particular we have in mind to apply the model to the evolution of sand dune, where non constant wind, sloped and rippled surfaces exists, and all these conditions may greatly affect the effective value of p_{reb}. Moreover, we recall that the saltation model exposed in Chapter 2 is based on the "single trajectory" hypothesis, while p_{reb} shall depend on the effective continuum distribution of impact angle and velocity.

In conclusion, the model for marked sand transport is composed by the following coupled conservation equations:

$$\begin{cases} \dfrac{\partial}{\partial t} \left(f_t \rho\right) + \nabla \cdot \left(f_t \rho \mathbf{u}\right) = \tilde{\Gamma} \\[2em] \rho_{dune} \left[\dfrac{\partial(L_a f_a)}{\partial t} + f_I \dfrac{\partial(h - L_a)}{\partial t} \right] = -\tilde{\Gamma} \end{cases} \tag{3.34}$$

where the exchange rate of marked sand from the static phase to the moving phase is:

$$\tilde{\Gamma} = \tilde{\Gamma}_i + \tilde{\Gamma}_a = \frac{\rho}{T}\left[(n - p_{reb})\,f_a - (1 - p_{reb})\,f_t\right] + \Gamma_a f_a. \tag{3.35}$$

The system (3.34) is coupled with the Eq.(3.31) which tracks the marked sand concentration in the sedimentary column, and with the system (3.23) which determines the variables of the dune evolution model h, ρ and $\mathbf{u}$. It must be equipped with an initial condition for the concentration in the active layer $f_a(x, y, 0)$ and an initial field of marked sand concentration in the substrate $f_b^0(x, y, z)$. Initial and inflow boundary condition must be given for the concentration in the moving phase $f_t(x, y, t)$.

3.2.2 Parameter estimation

The new parameters of the model are the depth of the active layer L_a and the probability of rebound p_{reb}. Moreover, we recall that the parameters r and $\tilde{\gamma}$ which appears in Eqs.(3.15)-(3.16), when we consider a single family saltation flux, have been combined through the definition a single parameter $\gamma = r\tilde{\gamma} = 0.2$, see Sections 2.2.4 and 2.3. Since we need the disjoint values of n and T in Eq.(3.35), we have to characterize the parameters r and $\tilde{\gamma}$ separately.

Parameter r

We start with a simplified procedure for the qualitative characterization of r. From Eq.(2.14), r is defined as the ratio between the mean horizontal velocity $\overline{U}_x$ and the increment between the initial and final horizontal velocity ΔU_{x0} of the typical saltation trajectory. This parameter can be estimated for rebounding grains. Referring to Fig.3.7, we have:

$$r = \frac{\overline{U}_x}{\Delta U_{x0}} = \frac{\overline{U}_x}{U_{imp}\cos(\theta_{imp}) - U_{reb}\cos(\theta_{reb})}.$$

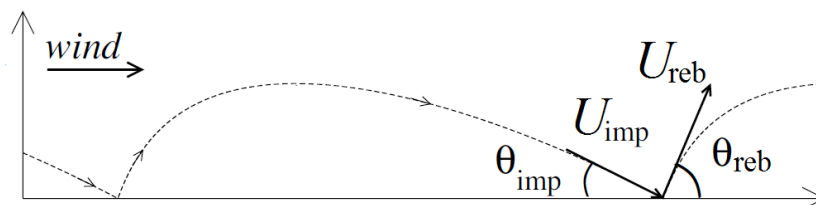**Figure 3.7: Sand grain trajectory** - Definition of impact and rebound velocity and angle. Adapted from (Almeida *et al.*, 2008).

We consider a simplified sand grain trajectory driven by drag force in horizontal direction and gravity in vertical direction:

$$\begin{cases} \dfrac{\mathrm{d}U_x}{\mathrm{d}t} = g\dfrac{(V - U_x)|V - U_x|}{u_f^2} \\ \dfrac{\mathrm{d}U_z}{\mathrm{d}t} = -g \\ U_x(0) = U_{reb}\cos(\theta_{reb}) \\ U_z(0) = U_{reb}\sin(\theta_{reb}) \end{cases} \qquad (3.36)$$

where u_f is the terminal fall velocity defined in Eq.(2.27), equal to $1.5\,\mathrm{m/s}$ for the considered sand grain diameter. We consider a simplified wind model consisting in a constant horizontal velocity V equal to the effective wind velocity for a saturated sand flux of $v_{sat}(u_*)$ given in Eq.(2.30). The second equation determines the flight time $T = 2U_z(0)/g$.

We fix some typical values (Rioual, 2002): $\theta_{imp} = 10°$, $\theta_{reb} = 40°$ and $U_{reb} = 0.4U_{imp}$. For a fixed value of u_*, we determine the only free parameter U_{imp} by solving iteratively the system (3.36) until equilibrium between solution at final and initial time is reached. Once the equilibrium trajectory is found, we calculate the mean horizontal velocity $\overline{U}_x = \frac{1}{T}\int_0^T U_x(t)\,\mathrm{d}t$ and hence the requested parameter r.

Varying the input value of shear velocity u_*, we obtain the results reported in Fig.3.8. In Fig.3.8(a), we notice that the obtained mean horizontal velocity $\overline{U}_x(u_*)$ is in good agreement with the value of the mean velocity of the saturated sand flux $u_{sat}(u_*)$ given in Eq.(2.31), which confirm that this procedure, although very simple, is qualitatively correct.

In Fig.3.8(b), we finally notice that the obtained value of parameter r is almost constant for varying u_*. This is a reassuring result, which allows us to take the value $r = 1$ in the following.

(a) $U_{imp}(u_*)$ and $\overline{U}_x(u_*)$ (b) $r(u_*)$
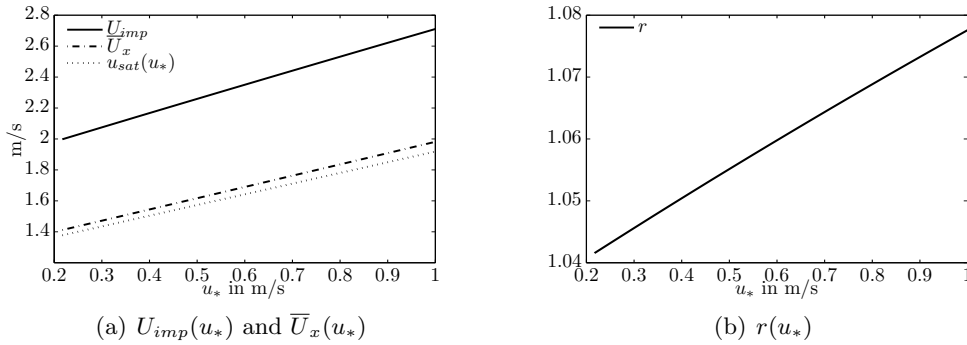
Figure 3.8: Estimation of parameter r - In (a), the velocity of impact U_{imp} and the mean horizontal velocity $\overline{U}_x$ are plotted for varying shear velocity. The behaviour of $\overline{U}_x(u_*)$ is in good agreement with $u_{sat}(u_*)$. In (b), the obtained value of parameter r is plotted for varying shear velocity. Its value $r \approx 1$ is almost constant.

Active layer depth and probability of rebound

Now we propose a technique to estimate the lacking parameters: the active layer depth L_a and the probability of rebound p_{reb}. In particular, we fit our model to the experimental data of Willetts & Rice (1988).

The experimental procedure is the following: in a wind tunnel, a horizontal sand bed of 10 mm depth is blown by constant wind. At a distance of 6 m from the inlet of the tunnel, a strip of coloured sand is collocated. The extension of the strip is 100 mm in the flow direction. Over the strip, a camera is placed over a sampling area of the strip near its upwind edge. The extension of the sampling area is 20 mm. When wind starts blowing, the camera takes a picture of the sampling area every 5 seconds. The number of surviving coloured grains in the sampling area is then counted in each photography. The sand considered in the experiment is not homogeneous: the mass distribution is composed at 22 % of coarse sediments (0.355 mm $< d <$ 0.6 mm), at 50 % of medium sediments (0.25 mm $< d <$ 0.355 mm) and at 28 % of fine sediments (0.150 mm $< d <$ 0.250 mm). The obtained results are reported subdivided in these three classes. In the following we use the results obtained for the medium class, since in our work we generally consider the typical value $d = 0.25$ mm, and the results for the fine class are affected by greater noise.

The experiment is repeated by varying the shear velocity u_*. The number of coloured grains counted in each photography is reported in Fig.3.9.
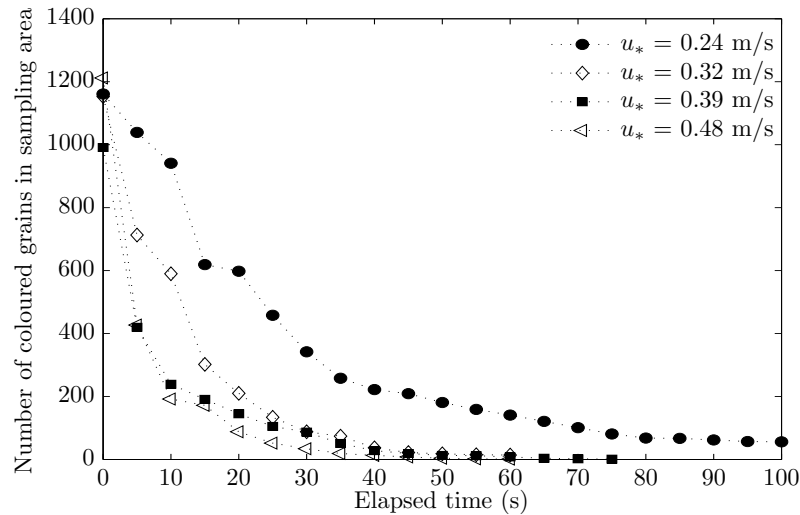
Figure 3.9: Results of Willetts & Rice (1988) experiment - Temporal evolution of the number of coloured grains in the sampling area for the different shear velocity considered in the experiment.

The model for marked sand transport can be fitted to this experiment; the experimental conditions are such that we will be able to characterize the interesting parameters. In particular, as the sampling area is 6 m from the beginning of the sand bed, we can

reasonably assume that the sand flux is saturated in this zone.

This leads to great simplifications of the model for marked sand transport of Eq.(3.34)-(3.35); in particular $\rho(x,t) = \rho_{sat}$, $\mathbf{u} = (u_{sat}, 0)$ and the active layer thickness L_a are constant in time and space. The direct aerodynamic entrainment Γ_a and the net impact-ejection balance Γ_i are null, or equivalently the number of ejected grains for each impacting grain is $n = 1$. These simplifications leads to the system:

$$\begin{cases} \rho_{sat}\dfrac{\partial f_t}{\partial t} + \rho_{sat}u_{sat}\dfrac{\partial f_t}{\partial x} = \tilde{\Gamma} \\[4mm] \rho_{dune}L_a\dfrac{\partial f_a}{\partial t} = -\tilde{\Gamma} \end{cases} \qquad (3.37)$$

with

$$\tilde{\Gamma} = \frac{\rho_{sat}}{T}\left(1 - p_{reb}\right)\left(f_a - f_t\right) \quad \text{and} \quad T = \frac{2\alpha}{g}\frac{u_{sat}}{r}$$

with all the quantities constant in time and space except the concentrations $f_t(x,t)$ and $f_a(x,t)$. Since the sampling area is placed at the upwind edge of the coloured strip, as a first approximation we can assume that over the sampling area the concentration of coloured sand in the moving phase is null. Hence we can decouple the equations in system (3.37) and obtain the equation for the concentration f_a in the active layer:

$$\frac{\partial f_a}{\partial t} = -k f_a \qquad \text{with} \qquad k = \frac{\rho_{sat}}{T\,\rho_{dune}}\frac{(1 - p_{reb})}{L_a}, \qquad (3.38)$$

whose solution is the exponential $f_a(t) = \exp(-kt)$. For the experiment data, the logarithm of the number of coloured grains shows a linear trend, hence we can estimate k from linear regression, as reported in Fig.3.10.

Since the prefactor $\rho_{sat}/T\rho_{dune}$ depends only on shear velocity u_*, we can use the obtained values of the decay rate k to estimate the ratio $L_a/(1-p_{reb})$. In the following, it is useful to write L_a as a multiple of the grain diameter: $L_a = Md$.

The results are reported in Tab.3.1. In the fourth column, the rescaled active layer depth M is expressed as a multiple of $(1 - p_{reb})$. If we assume p_{reb} constant with u_*, M would grow with u_*, reflecting the physical consideration that a stronger impact velocity leads to a deeper involvement of sand grains in the transport processes.

In the fifth column of Tab.3.1, we express $(1 - p_{reb})$ in term of the rescaled active layer thickness M. We notice that we must have $M \leq 0.622$ to have $(1 - p_{reb}) < 1$ in all the four cases. For instance, if we fix $M = 0.5$, we obtain $p_{reb} \approx 0.2$ for $u_* = 0.24\,\text{m/s}$ and $p_{reb} \approx 0.8$ for $u_* = 0.39\,\text{m/s}$.

This procedure delineates a range of values for the active layer thickness L_a and for the rebound probability p_{reb} that sound qualitatively correct, but the two unknown parameters cannot be obtained disjointly with this single set of experiments. Moreover, both L_a and p_{reb} may depend on the shear velocity u_*. The correctness of the results is furthermore affected by the experimental conditions; we recall that the sand used in the Willetts & Rice (1988) experiments is composed by coarse, medium and fine grains,
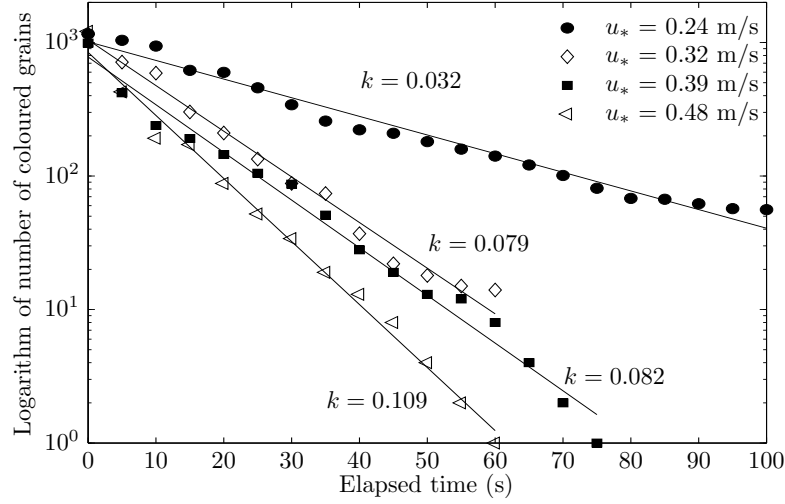
Figure 3.10: Linear fit of Willetts & Rice (1988) data - The decay rate k increases with shear velocity u_*.

and this fact naturally affects all the parameters used in the calibration such as the threshold shear velocity u_{*t}.

What is really important for the following is that the active layer thickness L_a is of the order of the grain diameter. This will lead to some important consideration when we will apply the model in the context of dune evolution, as we will see in Chapter 4.

u_* (m/s)	k (s^{-1})	$\dfrac{\rho_{sat}}{T\,\rho_{dune}}$ (m/s)	M	$(1-p_{reb})$
		$10^{-4}\times$	$(1-p_{reb})\times$	$M\times$
0.24	0.032	0.050	0.622	1.608
0.32	0.079	0.258	1.311	0.763
0.39	0.082	0.481	2.340	0.427
0.48	0.109	0.820	3.018	0.331

Table 3.1: Variation with u_* of time constant k obtained with exponential fitting of the data in Fig.3.9. The decay rate k can be expressed in terms of the known parameter in the third column. In the fourth column, the resulting value for the rescaled active layer thickness $M = L_a/d$ is expressed as a multiple of $(1-p_{reb})$. In the fifth column, $(1-p_{reb})$ is expressed as a multiple of M.

3.3   Description of avalanches

Besides the sand in saltation, the other transport mechanism is due to avalanches that spontaneously arise if the local slope exceeds the angle of repose of sand. Comparing the time scale of sand avalanches, which are of the order of some seconds, with the time scale of sand surface evolution, which is of the order of some hours as we have seen in Sect.3.1, we can consider the sand avalanche as an instantaneous event which acts as a constraint on the maximum slope of the sand surface:

$$|\nabla h| \leq \tan(\theta),$$

where $\theta = 34°$ is the angle of repose of desert sand, and this constraint has to be added to the system for sand surface evolution given in Eq.(3.23). This approach is profitable since we can avoid the accurate description of the avalanche process, and the solution of the constrained evolutionary problem is possible with numerical methods for variational inequalities (Glowinski, 2008; Caboussat & Glowinski, 2009).

On the other hand with this approach it is not possible to obtain a model for the transport of marked sand, so we need to derive an alternative formulation.

For the description of marked sand transport during sand avalanches processes, we intend to apply the same active layer framework seen in the case of transport driven by wind. In particular, we will consider the sand avalanche as a phenomena involving a static phase and a moving phase rolling over it. We have seen that to determine the exchange term of marked sand between the stating and moving phase, it is necessary to write the entrainment and deposition rate of sand, see Eq.(3.33).

We hence propose to describe the temporal variation of the sand surface due to the avalanches in terms of the balance between entrainment and deposition rates:

$$T_{av}\rho_{dune}\frac{\partial h}{\partial t} = \mathcal{D} - \mathcal{E}, \tag{3.39}$$

where T_{av} is a small time scale related to sand avalanches which allows to decouple Eq.(3.39) from the evolutionary equation (3.23) related to the saltation process.

In avalanches the sand begins to move when the local slope exceeds the angle of repose; we then assume the entrainment rate to be proportional to the excess of local slope with respect to the angle of repose:

$$\mathcal{E}(x,y) = M \max(|\nabla h(x,y)| - \tan(\theta), 0), \tag{3.40}$$

where M is a parameter whose dimensions are Kg/m^2. At this point, we can suppose that the entrained sand is deposited on the slip face line after rolling for a distance r, following a path along the line of maximum steepness. We assume that the distance r is probabilistic with a given probability density function $\mathcal{S}(r)$. Hence we can link the deposit rate to what is entrained above through an integral relation that in the two dimensional case reads:

$$\mathcal{D}(x) = \int_{x_B}^{x} \mathcal{E}(\xi)\mathcal{S}(x - \xi)\,d\xi, \tag{3.41}$$

where x_B is the position of the brink of the slip face. In the three dimensional case the convolution integral is written along the line of maximum steepness.

In Chapter 4 we will detail the avalanche model and characterize with the aid of numerical solution its dynamical and stationary behaviour.

4

Numerical methods and applications

In this Chapter, we propose some applications of the mathematical models proposed in previous sections. First we consider separately the model for sand avalanches. Then we consider the complete sand dune evolution with marked sand in the two dimensional case, as most of the characteristic phenomena leading to dune formation and evolution can be easily understood in this simplified setting. The numerical methods used for simulating the evolution of the system will also be detailed.

4.1   Avalanche model

Here we consider the mathematical and numerical modelling of sand avalanche both in the two dimensional and three dimensional cases. In particular, we need to provide a numerical procedure to solve the evolution of a sand surface subject to a point-wise constraint on the norm of the gradient. We introduce the mathematical augmented Lagrangian algorithm proposed in Caboussat & Glowinski (2009), and then detail our original formulation based on entrainment and deposition rates. With the aid of numerical examples, we will highlight the equivalence of the two approaches.

The setting of the problem is the following: let $\Omega \subset \mathbb{R}^d$ be a bounded domain with $d = 1, 2$ identifying the dimension of the problem. We consider the evolution of a sand surface $h(x, t)$, with $x \in \Omega$ and $t \in (0, T)$, $h(x, 0)$ being a known profile. The evolution of the sand surface is driven by a generic erosion-deposition operator $G = G(h, x, t)$ and subject to a point-wise constraint on the norm of the gradient:

$$\frac{\partial h}{\partial t} = G \qquad \text{s.t.} \qquad |\nabla h| \leq \tan(\theta). \tag{4.1}$$

In the sand dune evolution problem, $G = -\Gamma$, where Γ is the exchange rate between the sand surface and the saltation flux which is given by the intricate nonlinear relations which links the surface profile h to the wind shear stress τ and the saltation flux $\mathbf{q}$,

as seen in Sect.3.1. In the reference work (Caboussat & Glowinski, 2009), the authors considered the simplest case $G = -\mathbf{a} \cdot \nabla h + f$, where $\mathbf{a}$ is a given advection field and $f : f \geq 0$ is a given rate of added sand particles.
If we consider the functional spaces:

$$V = \{v \in H^1(\Omega) : v = 0 \text{ on } \partial\Omega\},$$
$$K = \{v \in V : |\nabla v| \leq \tan(\theta)\},$$

the problem Eq.(4.1) can be rewritten in the equivalent form:

$$\frac{\partial h}{\partial t} + \partial I_K(u) \ni G \tag{4.2}$$

where I_K is the indicator functional of the set K defined for all $v \in V$ as:

$$I_K(v) = \begin{cases} 0 & \text{if } v \in K, \\ +\infty & \text{if } v \notin K. \end{cases}$$

The time interval $t \in [0, T]$ is subdivided in N subintervals of equal duration Δt, and $t^n = n\Delta t$, $n = 0, ..., N$ are the discrete instants where the variables are approximated. We denote by h^n the approximation of $h(t^n)$. The first order Euler method is used to approximate the time derivative and an operator splitting technique is used for the numerical solution of Eq.(4.2). This method consists in solving successively

$$\frac{h^{n+1/2} - h^n}{\Delta t} = G^n \tag{4.3}$$

and

$$\frac{h^{n+1} - h^{n+1/2}}{\Delta t} + \partial I_K(h^{n+1}) \ni 0, \tag{4.4}$$

where Eq.(4.3) will be discretized explicitly since the erosion-deposition operator for the sand dune problem is a nonlinear term which requires many sub-calculation, as we will see in Sect.4.2-4.3.
In this Section we focus on the numerical solution of Eq.(4.4). Given a surface profile $h^{n+1/2} \notin K$, Eq.(4.4) projects it in the set K, providing a relaxed sand profile h^n which satisfies the point-wise constraint on the norm of the gradient. In the following we will neglect that the profile $h^{n+1/2} \notin K$ is given by the solution of the generic erosion-deposition operator G and, to ease notation, we set $h = h^{n+1}$ and $f = h^{n+1/2}$. Hence, the problem of surface relaxation of a generic profile $f \notin K$ is rewritten as:

$$h + \partial I_K(h) \ni f \tag{4.5}$$

4.1.1 An augmented Lagrangian technique

Following Glowinski (2008); Caboussat & Glowinski (2009), the Eq.(4.5) can be seen as the Euler-Lagrange equation corresponding to the minimization problem

$$h = \arg \min_{v \in K} \frac{1}{2} \int_{\Omega} |v - f|^2 \, \mathrm{d}x$$

which, equivalently, corresponds to minimize the functional

$$\min_{v \in K} \frac{1}{2} \int_{\Omega} |v|^2 \, \mathrm{d}x - \int_{\Omega} fv \, \mathrm{d}x. \tag{4.6}$$

The set K contains a point-wise constraint on the gradient of the function, which can be relaxed by penalization: let $\varepsilon > 0$ be a small parameter, the problem (4.6) is relaxed into:

$$\min_{v \in V} \frac{1}{2} \int_{\Omega} |v|^2 \, \mathrm{d}x - \int_{\Omega} fv \, \mathrm{d}x + \frac{1}{3\varepsilon} \int_{\Omega} \left(\left(|\nabla v|^2 - \tan(\theta)^2 \right)^+ \right)^3 \, \mathrm{d}x, \tag{4.7}$$

where $(\xi)^+ = \max(\xi, 0)$ denotes the positive part and the choice of the penalization exponent equal to 3 will be motivated below. Let us define $q = \nabla v \in L^2(\Omega)^d$ and denote $L^2(\Omega)^d$ by Q. Problem (4.7) is therefore equivalent to

$$\min_{\{v, q\} \in \mathcal{K}} \frac{1}{2} \int_{\Omega} |v|^2 \, \mathrm{d}x - \int_{\Omega} fv \, \mathrm{d}x + \frac{1}{3\varepsilon} \int_{\Omega} \left(\left(|q|^2 - \tan(\theta)^2 \right)^+ \right)^3 \, \mathrm{d}x, \tag{4.8}$$

where

$$\mathcal{K} = \{(v, q) \in V \times Q : \nabla v - q = 0\}.$$

Now, we impose the relation $\nabla v - q = 0$ by penalization and the use of a Lagrangian multiplier $\mu \in Q$, thus we define the augmented Lagrangian functional:

$$
\begin{aligned}
\mathcal{L}_r(v, q, \mu) \quad = \quad & \frac{1}{2} \int_{\Omega} |v|^2 \, \mathrm{d}x + \frac{r}{2} \int_{\Omega} |\nabla v - q|^2 \, \mathrm{d}x + \int_{\Omega} \mu \cdot (\nabla v - q) \, \mathrm{d}x - \int_{\Omega} fv \, \mathrm{d}x \\
& + \frac{1}{3\varepsilon} \int_{\Omega} \left(\left(|q|^2 - \tan(\theta)^2 \right)^+ \right)^3 \, \mathrm{d}x,
\end{aligned}
$$

now we observe that if $\{u, p, \lambda\} \in V \times Q \times Q$ is a saddle point of $\mathcal{L}_r$, *i.e.* verifies

$$\mathcal{L}_r(u, p, \mu) \leq \mathcal{L}_r(u, p, \lambda) \leq \mathcal{L}_r(v, q, \lambda) \qquad \forall \{v, q, \mu\} \in V \times Q \times Q$$

then, the pair $\{u, p\}$ solves problem (4.8), which implies that u is solution of (4.7) and that $p = \nabla u$.

In order to solve the saddle point problem the authors propose the following Uzawa-type algorithm:

- $u^{-1} \in V$ and $\lambda^0 \in Q$ are given arbitrary function (typically $u^{-1} = f$ and $\lambda^0 = 0$). Then, for $k = 0, 1, 2, \ldots$, being u^{k-1} and λ^k known:

4. NUMERICAL METHODS AND APPLICATIONS

1. Find $p^k \in Q$ such that

$$\mathcal{L}_r(u^{k-1}, p^k, \lambda^k) \leq \mathcal{L}_r(u^{k-1}, q, \lambda^k) \qquad \forall q \in Q; \tag{4.9}$$

2. then, find $u^k \in V$ such that

$$\mathcal{L}_r(u^k, p^k, \lambda^k) \leq \mathcal{L}_r(v, p^k, \lambda^k) \qquad \forall v \in V; \tag{4.10}$$

3. finally, update the multipliers $\lambda^{k+1} \in Q$:

$$\lambda^{k+1} = \lambda^k + r(\nabla u^k - p^k).$$

until convergence is reached.

This algorithm has already been introduced with the name ALG2 in Fortin & Glowinski (1983); Glowinski & Le Tallec (1989); Glowinski (2008), where one can also find the proof of the following convergence results:

$$\forall \, \{u^{-1}, \lambda^0\} \in V \times Q, \quad \lim_{k \to \infty} \{u^k, p^k\} = \{u, \nabla u\}$$

Regarding the effective implementation of the algorithm, Eq.(4.9) corresponds to find:

$$p^k = \arg\min_{q \in Q} \frac{r}{2} \int_\Omega |q|^2 \, \mathrm{d}x - \int_\Omega (r\nabla u^{k-1} + \lambda^k) \cdot q \, \mathrm{d}x + \frac{1}{3\varepsilon} \int_\Omega \left(\left(|q|^2 - \tan(\theta)^2\right)^+ \right)^3 \, \mathrm{d}x;$$

this minimization problem does not involve any derivative of q, so it can be solved point-wise in Ω: for $x \in \Omega$ given. It corresponds to find:

$$p^k = \arg\min_{q(x) \in \mathbb{R}^d} \left[\frac{r}{2} |q(x)|^2 - X^k(x) \cdot q(x) + \frac{1}{3\varepsilon} \left(\left(|q(x)|^2 - \tan(\theta)^2\right)^+ \right)^3 \right] \tag{4.11}$$

where $X^k(x) = r\nabla u^{k-1}(x) + \lambda^k(x)$. This strictly convex minimization problem admits a unique minimizer.
The other step of the algorithm, (4.10), corresponds to find:

$$u^k = \arg\min_{v \in V} \frac{r}{2} \int_\Omega |\nabla v|^2 \, \mathrm{d}x + \frac{1}{2} \int_\Omega |v|^2 \, \mathrm{d}x - \int_\Omega (rp^k - \lambda^k) \cdot \nabla v \, \mathrm{d}x - \int_\Omega fv \, \mathrm{d}x,$$

whose optimality condition leads to the following linear Dirichlet problem: find $u^k \in V$ such that, $\forall \, v \in V$:

$$r \int_\Omega \nabla u^k \cdot \nabla v \, \mathrm{d}x + \int_\Omega u^k v \, \mathrm{d}x = \int_\Omega (rp^k - \lambda^k) \cdot \nabla v \, \mathrm{d}x + \int_\Omega fv \, \mathrm{d}x. \tag{4.12}$$

Numerical approximation

A finite element method is used for the numerical resolution of the steps of the algorithms (4.9) and (4.10); let $h > 0$ be the discretization parameter and $\mathcal{T}_h$ the partition of the domain Ω in sub-domains, which can either be intervals if $d = 1$ or triangles if $d = 2$. The main finite elements spaces are defined by:

$$X_h^1 = \{v \in C^0(\bar{\Omega}) : v|_K \in \mathbb{P}^1, \forall K \in \mathcal{T}_h\}$$
$$X_h^0 = \{v \in L^2(\Omega) : v|_K \in \mathbb{P}^0, \forall K \in \mathcal{T}_h\},$$

while, for the problem we are considering, we will use the following spaces:

$$V_h = \{v \in X_h^1 : v = 0 \text{ on } \partial\Omega\}$$
$$K_h = \{v \in V_h : |\nabla v|_K| \leq \tan(\theta), \ \forall K \in \mathcal{T}_h\}$$
$$Q_h = \left(X_h^0\right)^d$$

The discrete version of the algorithm consists in computing $u_h \in V_h$, $p_h \in Q_h$ and $\lambda_h \in Q_h$ through the following steps (the subscripts h are omitted):

- $u^{-1} \in V_h$ and $\lambda^0 \in Q_h$ are given arbitrary function (typically $u^{-1} = f$ and $\lambda^0 = 0$). Then, for $k = 0, 1, 2, \ldots$, being u^{k-1} and λ^k known:

  1. since $p^k \in Q_h$ is piecewise constant on each element $K_i \in \mathcal{T}_h$, we can solve problem (4.11) on each element K_i:

  $$p_i^k = \arg\min_{q_i \in \mathbb{R}^d} \left[\frac{r}{2}|q_i|^2 - X_i^k \cdot q_i + \frac{1}{3\varepsilon}\left(\left(|q_i|^2 - \tan(\theta)^2\right)^+\right)^3\right]$$

  where X_i^k is the piecewise constant value of $r\nabla u^{k-1} + \lambda^k$ on the ith element. The minimum occurs when $q_i = \xi X_i^k$, ($\xi \in \mathbb{R}$). In fact, let

  $$f(s) = \frac{r}{2}s + \frac{1}{3\varepsilon}\left(\left(s^2 - \tan(\theta)^2\right)^+\right)^3,$$

  we have to find

  $$p_i^k = \arg\min_{q_i \in \mathbb{R}^d} f(q_i \cdot q_i) - X_i^k \cdot q_i.$$

  The optimality condition is then given by

  $$2\frac{\mathrm{d}f}{\mathrm{d}s}q_i - X_i^k = 0,$$

  which shows that the minimizing vector p_i^k must be parallel to X_i^k. Hence the minimization problem becomes:

  $$\eta_i = \arg\min_{\xi \in \mathbb{R}} \frac{r}{2}\xi^2|X_i^k|^2 - |X_i^k|^2\xi + \frac{1}{3\varepsilon}\left(\left(\xi^2|X_i^k|^2 - \tan(\theta)^2\right)^+\right)^3.$$

4. NUMERICAL METHODS AND APPLICATIONS

The minimum is thus given by the solution of the nonlinear equation:

$$r\xi - 1 + \frac{2}{\varepsilon}\xi \left(\left(\xi^2 |X_i^k|^2 - \tan(\theta)^2 \right)^+ \right)^2 = 0, \qquad (4.13)$$

which is solved with a Newton method in order to obtain η_i and set $p_i^k = \eta_i X_i^k$ for each element $K \in \mathcal{T}_h$.

2. compute $u^k \in V_h$ such that it solves $\forall v \in V_h$ the Dirichlet problem (4.12); in particular, denoting with φ_j, $j = 1, \ldots, N_h$ the finite element basis functions for V_h, by setting $u^k(x) = \sum_{j=1}^{N_h} u_j \varphi_j(x)$, (4.12) corresponds to solve the linear system

$$\sum_{j=1}^{N_h} u_j \left(r \int_\Omega \nabla\varphi_j \cdot \nabla\varphi_i \, \mathrm{d}x + \int_\Omega \varphi_j \varphi_i \, \mathrm{d}x \right) =$$
$$\int_\Omega (r p^k - \lambda^k) \cdot \nabla\varphi_i \, \mathrm{d}x + \int_\Omega f \varphi_i \, \mathrm{d}x, \qquad i = 1, \ldots, N_h. \qquad (4.14)$$

3. finally, we update the multipliers $\lambda^{k+1} \in Q_h$ by:

$$\lambda^{k+1}|_K = \lambda^k|_K + r(\nabla u^k|_K - p^k|_K), \qquad \forall K \in \mathcal{T}_h,$$

until convergence is reached. We stop the algorithm when the normalized relative increments of the variable u between two successive iterates is less than a given tolerance:

$$\frac{\|u^{k+1} - u^k\|_{L^2(\Omega)}}{\|f\|_{L^2(\Omega)}} \le tol. \qquad (4.15)$$

We now provide some numerical examples to illustrate the behaviour of the augmented Lagrangian algorithm.

Example 1 We first apply the algorithm to a one dimensional test case. We consider the interval $\Omega = [0, 10]$ and we define the initial function to be projected on the set K as:

$$f(x) = \begin{cases} 3\cos^2\left(\frac{\pi}{5}(x-5)\right) & \text{if } x \in [2.5, 7.5], \\ 0 & \text{otherwise.} \end{cases} \qquad (4.16)$$

The initial profile $f(x)$ is represented in Fig.4.1, where also the gradient $\nabla f(x)$ is shown: we see that $f(x) \notin K$.

We then apply the augmented Lagrangian algorithm considering a discretization of the domain in 100 equispaced intervals. The penalization parameters is set to $\varepsilon = 10^{-12}$, as recommended in the original work (Caboussat & Glowinski, 2009). The Newton
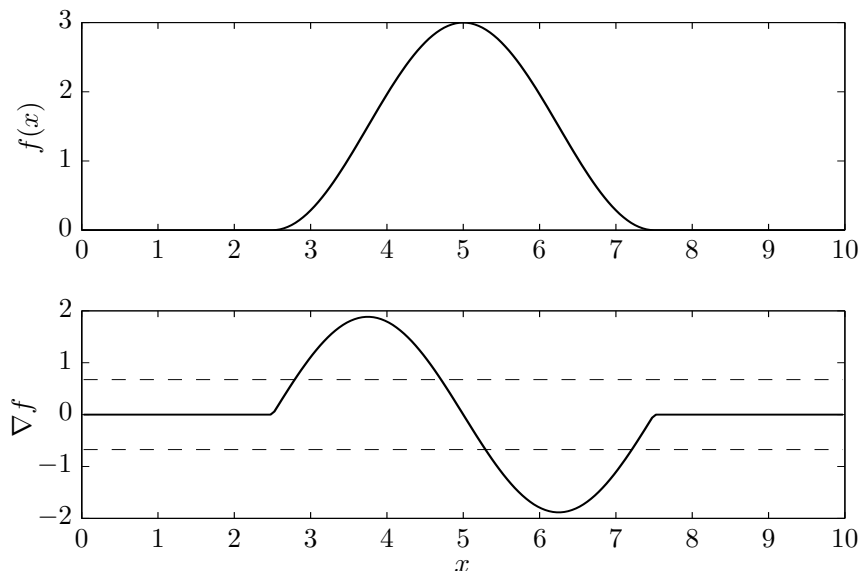
70

Figure 4.1: Initial profile for Example 1 - On top $f(x)$, on bottom the gradient $\nabla f(x)$. The dashed lines represents the boundaries of the admitted region $|\nabla u| \leq \tan(\theta) = 0.6745$ for the angle of repose of sand $\theta = 34°$.

method for the solution of the nonlinear equation (4.13) is stopped when the increment between two iterates is less than $tol = 10^{-12}$, with up to 100 iterations.

The iterations are stopped when Eq.(4.15) is verified, with $tol = 10^{-6}$. The choice of the parameter r plays a crucial role in the global convergence of the algorithm. The optimal value depends mainly on the length scale of the problem. In particular, we noticed that applying the algorithm to a rescaled profile with scale factor δ, the history convergence of the algorithm is equivalent if we scale the parameter r with δ^2. For this particular problem, we performed several tests and found that the optimal value is $r_{\text{opt}} = 0.1$; with this choice, the convergence criterion (4.15) is satisfied in 131 iterations. The obtained relaxed profile u^k, together with the dual variable p^k and the Lagrangian multiplier λ^k are shown in Fig.4.2. The relaxed profile is a sharp triangular pile.

Example 2 Now we consider the two dimensional case. We take the domain $\Omega = [-5, 5]^2$ and an initial profile, steeper than the angle of repose, given by:

$$f(x,y) = \begin{cases} 3\cos^2\left(\dfrac{\pi}{5}x\right)\cos^2\left(\dfrac{\pi}{5}y\right) & \text{if } x \in [-2.5, 2.5] \text{ and } y \in [-2.5, 2.5], \\ 0 & \text{otherwise.} \end{cases} \tag{4.17}$$

The domain Ω is triangulated after a subdivision into 32×32 equal squares, each split into four triangles. All the parameters of the algorithm are equal to the values given
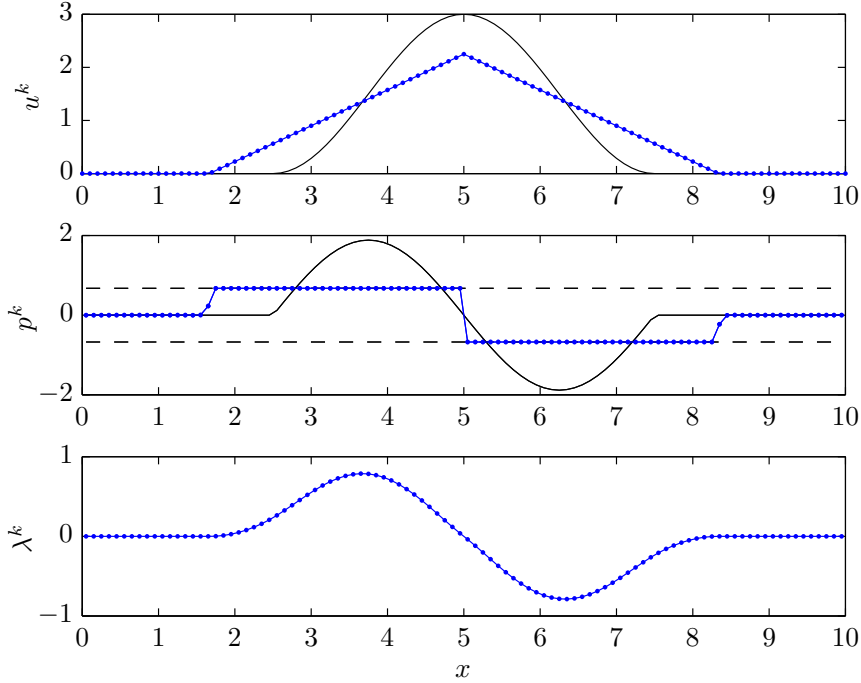
Figure 4.2: Solution of the problem in Example 1 obtained with the augmented Lagrangian algorithm - On top, the dotted line is the relaxed profile $u^k = h$, while the continuous line is the initial profile $f(x)$. In the middle is represented the dual variable $p^k = \nabla h$ together with ∇f, on bottom the Lagrangian multiplier λ^k.

in Example 1, except the parameter r whose optimal value is found to be $r_{\text{opt}} = 1$. The algorithm satisfy the convergence criterion (4.15) in 221 iterations. The solution is shown in Fig.4.3; the initial steep surface is relaxed to a sharp conical sand pile, even if the initial profile does not have circular sections.

4.1.2   An entrainment-deposition formulation

The solution of problem (4.5) describing the relaxation of a steep surface f under the point-wise constraint on the norm of the gradient can be also resolved with the entrainment-deposition formulation proposed in Sect.3.3. In particular, the relaxed sand profile h can be obtained as a stationary solution of the evolutionary equation (3.39), which is rewritten here coherently with the notation introduced previously in the form of a Cauchy problem:

$$\begin{cases} \dfrac{\partial u}{\partial t_{av}} = \mathcal{D} - \mathcal{E}, \\ u(x,0) = f(x). \end{cases}$$
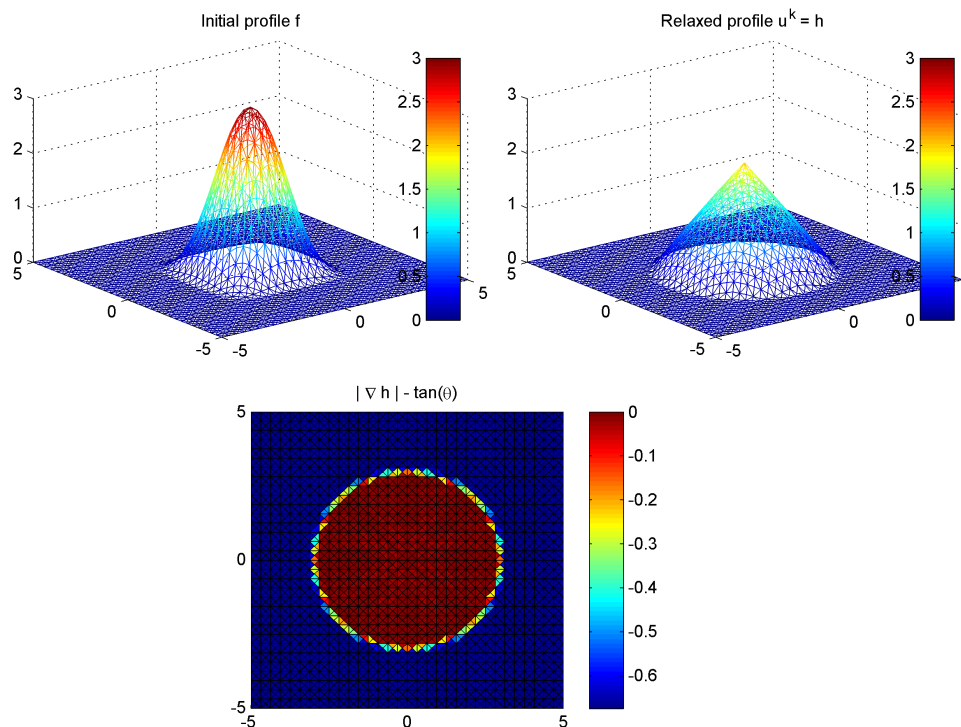
Figure 4.3: Solution of the problem in Example 2 obtained with the augmented Lagrangian algorithm - On top, at the left the initial steep profile f, on the right the relaxed profile $u^k = h$. In the bottom figure, the piece-wise constant $|\nabla h| - \tan(\theta)$ is plotted for each triangle of the mesh, showing that the relaxed profile is a conical sand pile with constant slope equal to the angle of repose.

Here t_{av} denotes the time axis related to sand avalanches, and incorporates the physical parameters T_{av}, ρ_{dune} and M which appears in Eqs.(3.39)-(3.40). The relaxed sand profile is given by $h(x) = \lim_{t\to+\infty} u(x,t)$.

As usual, we consider the discrete instants $t_{av}^k = k\Delta t_{av}$, $k = 0, 1, 2, \cdots$, and approximate the time derivative with the first order explicit Euler method:

$$u^{k+1} = u^k + \Delta t_{av}(\mathcal{D}^k - \mathcal{E}^k), \tag{4.18}$$

Here we propose the following algorithm for the evolution of Eq.(4.18):

- $u^0 = f$ is the initial profile which exceed the maximum admitted slope. Then, for $k = 0, 1, 2, \ldots$, being u^k known:

  1. compute the gradient ∇u^k.

  2. compute the erosion rate $\mathcal{E}^k = \max(|\nabla u^k| - \tan(\theta), 0)$.

  3. for each point x, compute the descent direction of maximum steepness

  $$d^k = -\nabla u^k / |\nabla u^k|.$$

4. assuming that, once entrained, the sand is deposited after rolling for a distance r along the descent direction, and that the length r is probabilistic with a given density function $\mathcal{S}(r)$, the mass of sand entrained from the point $\overline{x}$ is deposited in the point $\overline{x} + rd^k(\overline{x})$ through the relation:

$$\mathcal{D}^k(\overline{x} + rd^k(\overline{x})) = \mathcal{S}(r)\mathcal{E}^k(\overline{x})$$

5. finally, update the surface profile via Eq.(4.18).

until convergence is reached.

We now detail the numerical approximation of the entrainment and deposition rates, first in the two dimensional and then in the three dimensional case.

Numerical approximation in the two dimensional case

The horizontal domain $[0, L]$ is subdivided in N_x intervals of equal size $\Delta x = L/N_x$, and the variables are approximated at the points $x_i = i\Delta x$, $i = 0, 1, \ldots, N_x$ with the notation $f_i \simeq f(x_i)$. We neglect the superscript k for ease notation. We set by definition the backward and forward finite differences

$$D_x^- u_i = \frac{u_i - u_{i-1}}{\Delta x}, \qquad D_x^+ u_i = \frac{u_{i+1} - u_i}{\Delta x}. \tag{4.19}$$

Then we discretize the derivative of u at node x_i by the following difference scheme, see Fig.4.4:

$$D_x u_i = \begin{cases} 0 & \text{if } D_x^- u_i \leq 0,\ D_x^+ u_i \geq 0, \\ D_x^- u_i & \text{if } D_x^- u_i > 0,\ D_x^+ u_i \geq 0, \\ D_x^+ u_i & \text{if } D_x^- u_i \leq 0,\ D_x^+ u_i < 0, \\ \text{maxmod}(D_x^- u_i, D^+ u_i) & \text{if } D_x^- u_i > 0,\ D_x^+ u_i < 0. \end{cases} \tag{4.20}$$

For local minima, the approximated derivative is null. On sloped surface, the approximated derivative is the backward (forward) finite difference for positive (negative) slopes, that is the finite difference which points downwards. For local maxima, the biggest finite difference in magnitude is taken. The idea is to take the finite difference pointed towards the direction of rolling of the avalanche. A similar finite difference scheme has been proposed in (Falcone & Finzi Vita, 2007) for the numerical solution of the growing sandpile problem, but here the underlying mathematical model is different. With scheme (4.20), the absolute value of the approximated derivative is

$$|D_x u_i| = \frac{1}{\Delta x} \max(u_i - u_{i-1}, u_i - u_{i+1}, 0),$$

a popular finite difference scheme adopted for the numerical solution of the eikonal equation, see *e.g.* (Sethian, 1999; Oberman, 2006).
The discrete entrainment rate is a calculated at each grid node through

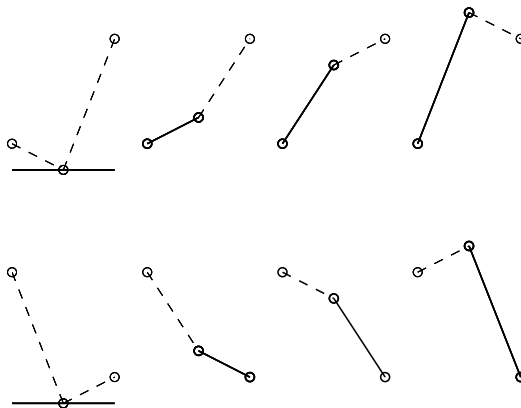$$\mathcal{E}_i = \max(|D_x u_i| - \tan(\theta), 0).$$

Figure 4.4: Finite difference scheme for gradient calculation. - For local minima, the approximated gradient is null. In the general case, the approximated gradient is the finite difference which points downwards. For local maxima, it is the biggest finite difference in magnitude.

In the two dimensional case the descent direction is easily calculated:

$$d_i = \begin{cases} +1 & \text{if } D_x u_i < 0, \\ -1 & \text{if } D_x u_i > 0. \end{cases}$$

At this point, we define the probability density function for the rolling distance $\mathcal{S}(r)$: it is a generic positive function, such that $\mathcal{S} = 0$ if $r < 0$ and $\int_0^{+\infty} \mathcal{S}(r)\,\mathrm{d}r = 1$. Its discrete counterpart is formed by the following entries:

$$\mathcal{S}_0 = \int_0^{\Delta x/2} \mathcal{S}(r)\,\mathrm{d}r, \quad \mathcal{S}_i = \int_{(i-1/2)\Delta x}^{(i+1/2)\Delta x} \mathcal{S}(r)\,\mathrm{d}r, \quad i = 1, \dots, N_{av}. \tag{4.21}$$

Even if we can a priori define $\mathcal{S}(r)$ such that $\mathcal{S}(r) > 0$ for $x \to +\infty$ (*e.g* an exponential p.d.f.), we must limit the number of entries of the discrete version of $\mathcal{S}$ to $N_{av} + 1$. In any cases, since quadrature error can occur in numerical integration of Eq.(4.21), the entries $\mathcal{S}_i$ are renormalized to have $\sum_{i=0}^{N_{av}} \mathcal{S}_i = 1$.
Given the discrete p.d.f. for rolling distance, having calculated the entrainment rate and the descent direction, the deposition rate in each node is given by the discrete version of the convolution integral (3.41):

$$\mathcal{D}_i = \sum_{j=0}^{N_x} \mathcal{D}_{i \leftarrow j}, \tag{4.22}$$

where $\mathcal{D}_{i \leftarrow j}$ is the rate of sand coming from the j-th node deposited at the i-th node. The latter, in turn, is given by:

$$\mathcal{D}_{i \leftarrow j} = \begin{cases} \mathcal{S}_{i-j} \mathcal{E}_j & \text{if } D_x u_j < 0, \\ \mathcal{S}_{j-i} \mathcal{E}_j & \text{if } D_x u_j > 0, \end{cases} \tag{4.23}$$

with the implicit assumption that $\mathcal{S}_i = 0$ for $i < 0$.

Once the deposition rate is calculated, the surface profile is updated using Eq.(4.18), and the procedure is repeated until convergence is reached.

We now provide some numerical examples to illustrate the behaviour of the entrainment-deposition model for relaxation of the two dimensional sandpile.

Example 3 We set the same initial condition (4.16) of Example 1. The domain $\Omega = (0, 10)$ is discretized in 100 intervals of amplitude $\Delta x = 0.1$. We choose an exponential p.d.f. for rolling distance

$$\mathcal{S}(r) = \frac{1}{\lambda} e^{-\frac{r}{\lambda}}. \tag{4.24}$$

We simulate the sandpile collapse assuming a mean rolling distance $\lambda = 0.2$ and $\lambda = 0.5$ respectively. The entries of the discrete p.d.f. are calculated up to a distance equal to 5λ, which combined with the chosen Δx leads to $N_{av} = 10$ and 25 respectively. The stopping criteria is the same used in Example 1, *i.e.* Eq.(4.15). We choose $\Delta t_{av} = \Delta x / 2$, as we have numerically verified that the algorithm is stable if the condition $\Delta t_{av} \leq \Delta x$ is verified.

The algorithm satisfies the desired tolerance in 605 and 273 iterations respectively. The obtained solutions are reported in Fig.4.5: we note that the obtained relaxed profile are really similar to the profiles obtained with the augmented Lagrangian algorithm, except for a tail of the profile at the foot of the relaxed sand pile. This effect is due to the exponential p.d.f. for rolling distance which tends to diffuse the final profile.

Example 4 The exponential p.d.f. for rolling distance proposed in Example 3 suffers from at least two important drawbacks: the first one is the tail effects at the foot of the sand pile, the second one is that the with these p.d.f. we cannot deal with the case of two interacting avalanches coming from opposite directions.

We can prevent these drawbacks by limiting as much as possible the width of the p.d.f. for rolling distance. But taking a narrow continuous p.d.f. (such as Eq.(4.24) with a small λ) would mean that we have to decrease the interval width Δx to capture such fast variation. This, in turn, would results in impractical mesh size, when we apply the model to the evolution of sand dune.

A different choice to circumvent these problems is to assume, at the discrete level, that
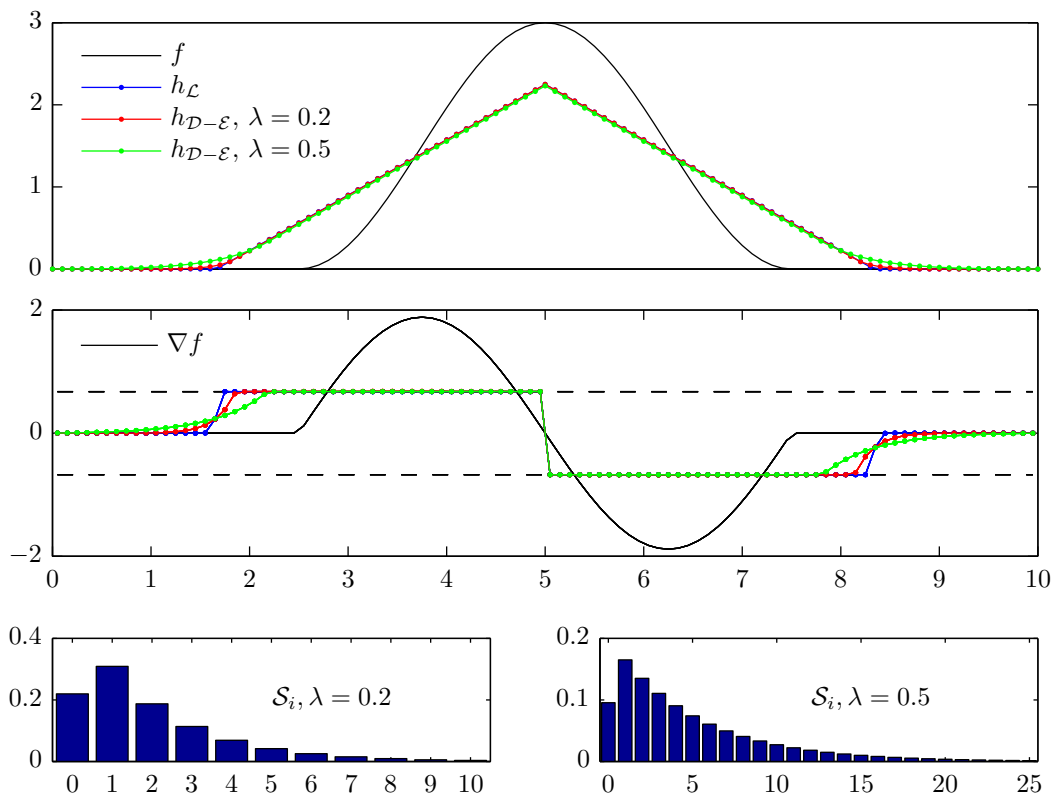
Figure 4.5: Comparison between algorithms for the collapsing sandpile problem - On top, the relaxed profiles h obtained with the entrainment-deposition formulation and exponential p.d.f. for rolling distance are compared to the one obtained with the augmented Lagrangian algorithm. In the middle, the slopes of the relaxed profiles are shown. It is evident a tail effect at the foot of the relaxed profile. On bottom, the entries of the discrete p.d.f. are represented for the two choices of λ.

all the sand entrained from a mesh node is deposited on the next node in downward direction. Formally, at the continuous level, we choose :

$$\mathcal{S}(r) = \delta(r - \Delta x), \qquad (4.25)$$

where δ is the Dirac delta function. Its discrete counterpart (4.21) is simply given by the two entries $\mathcal{S}_0 = 0$ and $\mathcal{S}_1 = 1$.

We compare in Fig.4.6 the relaxed profile obtained with the augmented Lagrangian algorithm and with the entrainment-deposition formulation with the p.d.f. (4.25). The initial profile is formed by a triangle, a square and a cosine hill placed in such a manner that the avalanches formed on opposite sides of the profiles will interact. The domain $\Omega = (0, 10)$ is subdivided in 100 subintervals. The relaxed sandpile is obtained in 120 iterations of the augmented Lagrangian algorithm with $r = 0.1$ and in 237 iterations of the entrainment-deposition formulation with $\Delta t_{av} = \Delta x/2$. The obtained relaxed

profile, shown in Fig.4.6, are almost indistinguishable.

In conclusion, the original entrainment-deposition formulation, with p.d.f. for rolling grains given by Eq.(4.25), can reproduce the exact profile of relaxed sandpile. Moreover, this formulation is based on the physics of the rolling process dynamics, and hence can be used to study the dispersion of marked sands during the avalanche. Finally, the method is fully explicit, and hence faster than the augmented Lagrangian algorithm, which at each iteration must solve the linear system given in Eq.(4.14).
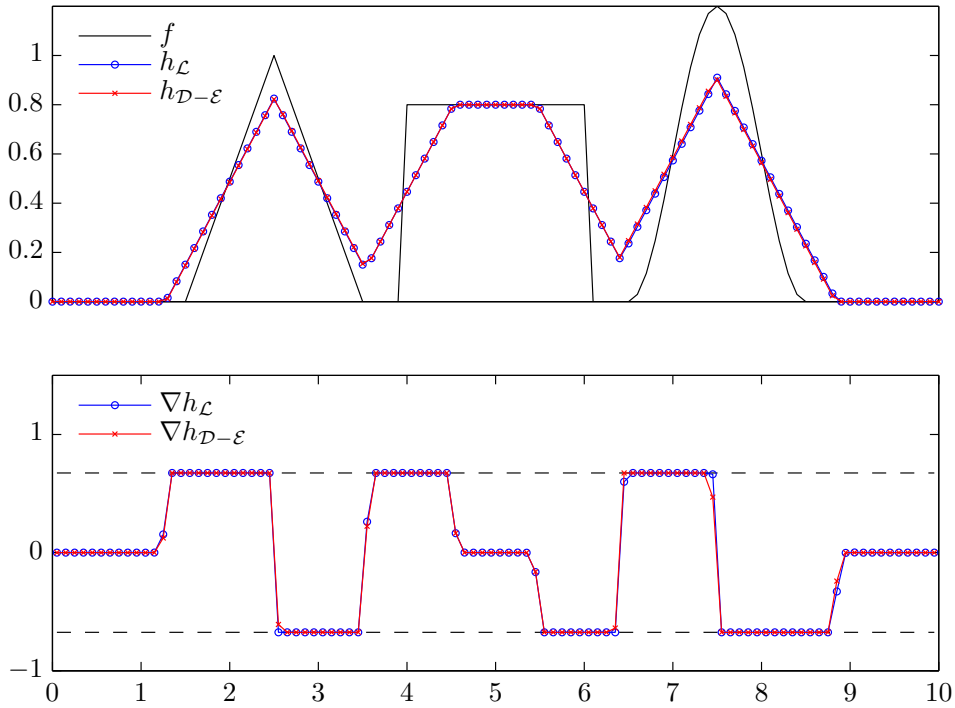
Figure 4.6: Comparison of the two algorithm for the interacting avalanche problem. - On top, the initial profile f is shown in black. The relaxed profile obtained with the augmented Lagrangian algorithm is shown in blue, while the one obtained with the entrainment-deposition formulation is shown in red. On bottom, the slopes of the relaxed profiles are shown.

Numerical approximation in the three dimensional case

We suppose a rectangular domain $\Omega = (0, L_x) \times (0, Ly)$, subdivided in $N_x \times N_y$ cells of equal extension $\Delta x \times \Delta y$. The notation f_{ij} indicates the approximated value of $f(x_i, y_j)$, where the discretization nodes are $x_i = i\Delta x$, $i = 0, \ldots, N_x$ and $y_j = j\Delta y$,

$j = 0, \ldots, N_y$.

In the step of evolution of Eq.(4.18), we first need to calculate the gradient of the surface u (we omit the superscript k for ease notation). In each grid node, the approximated gradient is given by

$$Du_{ij} = (D_x u_{ij}, D_y u_{ij}),$$

where $D_x u_{ij}$ and $D_y u_{ij}$ are given by the straightforward application of the schemes (4.19)-(4.20) to the two directions of the cartesian grid.

The magnitude of the approximated gradient reads:

$$|Du_{ij}| = \left(D_x u_{ij}^2 + D_y u_{ij}^2\right)^{1/2},$$

hence the discretized entrainment rate is given by

$$\mathcal{E}_{ij} = \max(|Du_{ij}| - \tan(\theta), 0),$$

to be further interpreted as a piecewise constant data on the cell $[x_{i-1/2}, x_{i+1/2}] \times [y_{j-1/2}, y_{j+1/2}]$. The descent direction is the unitary vector:

$$d_{ij} = -\frac{1}{|Du_{ij}|}(D_x u_{ij}, D_y u_{ij}).$$

Following the consideration made for the two dimensional case in Example 4, we choose the p.d.f. for rolling distance as

$$\mathcal{S}(r) = \delta(r - \Delta\mathcal{S})$$

where $\Delta\mathcal{S}$ is taken equal to $\min(\Delta x, \Delta y)$ to ensure that the sand entrained from node (x_i, y_j) will deposit only in neighbour nodes. In fact, the deposition rate is obtained by shifting the piecewise constant entrainment rate $\mathcal{E}_{ij}$ by distance $d_{ij}\Delta\mathcal{S}$, and then calculating the amount of deposited sand on each neighbour cell, see Fig.4.7. Once the entrainment and deposition rates are calculated, the surface profile is updated through Eq.(4.18), and the calculations are repeated until convergence is reached.

We now illustrate the behaviour of this model in some numerical examples.

Example 5 For comparison with the augmented Lagrangian algorithm, we take the domain and initial profile (4.17) of Example 2. Now the domain $\Omega = [-5, 5]^2$ is subdivided in 64×64 uniform cells. The entrainment-deposition relaxation algorithm satisfies the convergence criterion on the relative increments (4.15) in 341 iterations, given the tolerance $tol = 10^{-6}$. Even in this case, the relaxed profile is a conical sandpile, see Fig.4.8, almost undistinguishable from the profile obtained with the augmented Lagrangian algorithm of Fig.4.3.
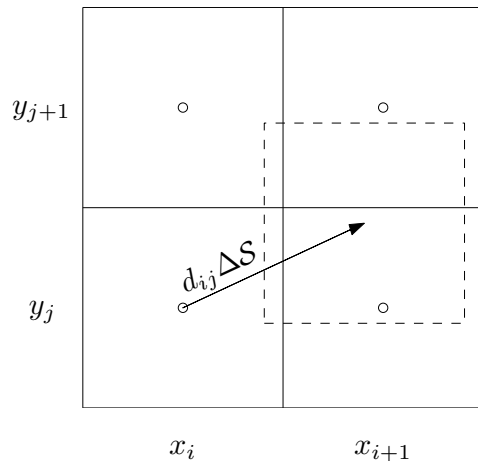
Figure 4.7: Deposition rate calculation in the three dimensional case - The piecewise constant entrainment rate $\mathcal{E}_{ij}$ is shifted by distance $d_{ij}\Delta\mathcal{S}$. From the area of the overlapping zones, we obtain the deposition rate on the neighbour cells.
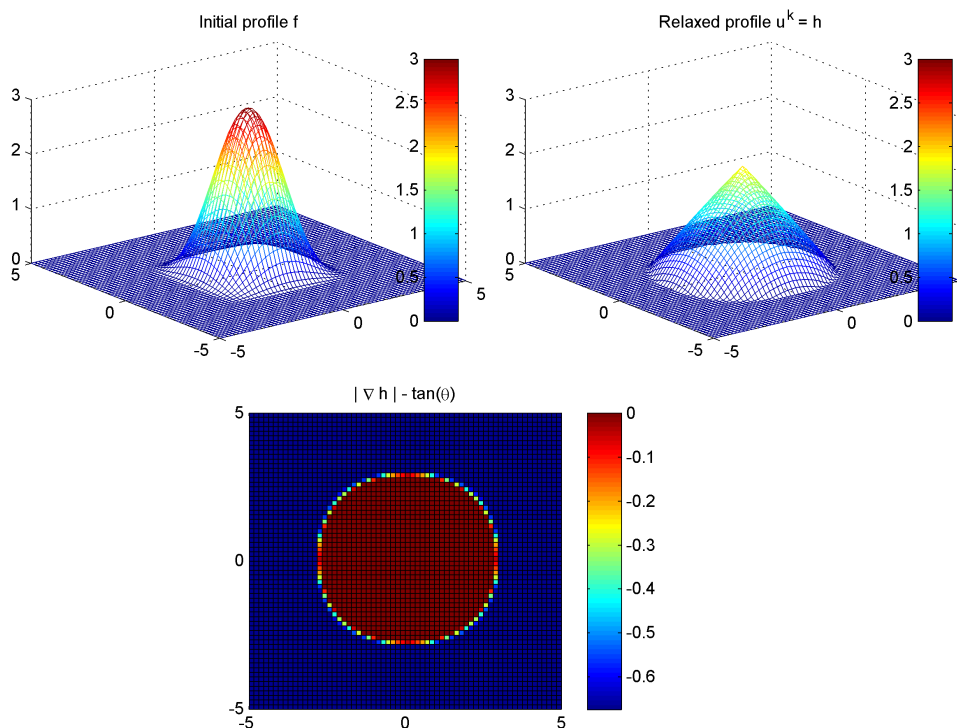
Figure 4.8: Solution of the problem in Example 5 obtained with the entrainment-deposition algorithm - On top, at the left the initial steep profile f, on the right the relaxed profile $u^k = h$. In the bottom figure, the value $|Dh - \tan(\theta)|$ is plotted. The results are really similar to that obtained with the augmented Lagrangian algorithm, see Fig.4.3.

4.2 The evolution of two dimensional dunes

In the two dimensional setting x is the horizontal direction aligned with wind direction and z is the vertical direction. The system given in Eq.(3.23) regulates the evolution of the the sand surface in the three dimensional case. In the two dimensional case the shear stress τ and the sand flux velocity u simplify to scalar fields, hence we can rewrite the system in the equivalent form:

$$
\begin{cases}
\rho_{dune}h_t = -\Gamma, \quad \text{s.t.} \quad |h_x| < \tan(\theta) & (4.26) \\
(\rho u)_x = \Gamma, & (4.27) \\
\rho u u_x = f_{drag} + f_{bed} + f_{grav}, & (4.28)
\end{cases}
$$

where the subscripts x and t denotes partial derivative with respect to the subscripted variable. As observed in Sec.3.1, the only time dependent equation is Eq.(4.26) which describes the temporal evolution of the sand surface $h(x,t)$. The exchange term Γ is given by the stationary solution of coupled equations (4.27)-(4.28).

This evolutionary model can also be coupled with the system given in Eq.(3.34) which regulates the evolution of the concentrations of marked sand in the sedimentary column and in the active layer. However, first we will analyse the dynamics of the model for sand dune, and subsequently consider the additional problem of marked sand dispersion.

4.2.1 Numerical methods

In the following, we consider the horizontal domain $x \in (0, L)$ subdivided in N_x intervals of equal size $\Delta x = L/N_x$. The midpoints $x_j = (j - \frac{1}{2})\Delta x$, $j = 1, ..., N_x$ are the point where the variables are approximated using the standard subscript notation $f_j \simeq f(x_j)$. The time interval $t \in [0, T_{\max}]$ is subdivided in N_t subintervals of equal duration Δt, and $t^n = n\Delta t$, $n = 0, ..., N_t$ are the discrete instants where the variables are approximated using the standard superscript notation $f_j^n \simeq f(x_j, t^n)$. In the following, the compact notation f^n (without subscripts) indicates the set of discrete values f_j^n, $j = 1, \ldots, N_x$ at time t^n.

Given the intricate nonlinear relations which link the sand flux to the topography, we consider an explicit discretization scheme for the equation (4.26) for temporal evolution of the sand surface. A simple technique consists in taking the explicit Euler method:

$$
h^{n+1/2} = h^n - \frac{\Delta t}{\rho_{dune}}\Gamma^n, \qquad n = 0, \ldots, N_t - 1. \tag{4.29}
$$

where h^0 is a given initial profile and the superscript $n + 1/2$ indicates that the obtained surface at this stage may not satisfies the pointwise constraint on the maximum admitted slope. To calculate the exchange rate Γ^n, we first need the shear stress on the sand surface. We then use the wind model proposed in Section 3.1.1, which in the two dimensional case consists in reconstructing the polynomial separating streamline

s^n and then calculating the shear stress with:

$$\tau^n = \begin{cases} 0 & \text{if } s^n > h^n \\ \tau_0(1 + \delta\tau^n) & \text{otherwise,} \end{cases} \tag{4.30}$$

where again we have specified that inside the recirculation bubble, where $s^n > h^n$, the shear stress is negligible for sand transport. The shear stress perturbation, calculated on the smooth surface $\tilde{h}^n = \max(h^n, s^n)$ which envelopes the separating streamline, is numerically given by:

$$\delta\tau^n = \frac{2}{U^2(l)} \texttt{ifft} \left\{ \left[|\boldsymbol{\kappa}| \left(1 + \frac{2\ln L|\boldsymbol{\kappa}| + 4\epsilon + 1}{\ln(l/z_0^{dune})} \right) + i\boldsymbol{\kappa}\frac{\pi}{\ln(l/z_0^{dune})} \right] \texttt{fft}\left\{ \tilde{h}^n \right\} \right\}. \tag{4.31}$$

In Eq.(4.31), $\texttt{fft}$ and $\texttt{ifft}$ denotes direct and inverse discrete Fourier transform respectively, $\boldsymbol{\kappa}$ is the discrete set of wave numbers used in the $\texttt{fft}$ algorithm.

Once the wind shear stress τ^n on the sand surface h^n has been calculated, the exchange term Γ^n is obtained from the the stationary density ρ^n and velocity u^n of the saltation flux which solves the coupled equations (4.27)-(4.28). For the numerical solution, it is convenient to exploit the relation:

$$\left(\rho u^2\right)_x = \rho u u_x + (\rho u)_x u$$

and rewrite Eq.(4.28) in the conservative form:

$$\left(\rho u^2\right)_x = f_{drag} + f_{bed} + f_{grav} + \Gamma u. \tag{4.32}$$

At this point, a straightforward technique to obtain the stationary solution of Eqs.(4.27)-(4.32) is to iterate the following time dependent system of conservation laws with source terms:

$$\begin{pmatrix} \rho \\ \rho u \end{pmatrix}_{t_1} + \begin{pmatrix} \rho u \\ \rho u^2 \end{pmatrix}_x = \begin{pmatrix} \Gamma \\ \Sigma_f + \Gamma u \end{pmatrix}, \tag{4.33}$$

until convergence is reached, where t_1 is a fictitious time needed only for reaching the stationary state and Σ_f denotes in a compact manner the sum of external forces $f_{drag} + f_{bed} + f_{grav}$.

From the extensive literature on numerical methods for the solution of systems of conservation laws with source terms like Eq.(4.33), we choose the operator splitting method (LeVeque, 2002; Toro, 2009) described in the following paragraph.

In general, for a system of conservation laws with source terms in the form:

$$\begin{cases} \mathbf{U}_t + \mathbf{F}(\mathbf{U})_x = \mathbf{S}(\mathbf{U}) \\ \mathbf{U}(x,0) = \mathbf{U}^0(x), \end{cases} \tag{4.34}$$

the operator splitting scheme consists in evolving $\mathbf{U}^n$ from time $t^n = n\Delta t$, $n \in \mathbb{N}$ to the new value $\mathbf{U}^{n+1}$ at time t^{n+1} with the following steps:

1. Solve the homogeneous advection problem:

$$\begin{cases} \mathbf{U}_t + \mathbf{F}(\mathbf{U})_x = \mathbf{0} \\ \mathbf{U}(x, t^n) = \mathbf{U}^n(x) \end{cases} \tag{4.35}$$

from t^n to t^{n+1}, to obtain $\mathbf{U}^*(x)$.

2. Solve the system of ordinary differential equations:

$$\begin{cases} \dfrac{\mathrm{d}\mathbf{U}}{\mathrm{d}t} = \mathbf{S}(\mathbf{U}) \\ \mathbf{U}(x, t^n) = \mathbf{U}^*(x) \end{cases} \tag{4.36}$$

from t^n to t^{n+1}, to obtain $\mathbf{U}^{n+1}(x)$, the solution of the the full problem (4.34) at time step t^{n+1}.

Each numerical sub-problem (4.35), (4.36) is solved separately for a time step Δt. We need a numerical method to solve the homogeneous advection problem in Eq.(4.35), and another numerical method to solve the system of ordinary differential equation in Eq.(4.36), with the initial data taken from the solution of (4.35). The splitting scheme is generically first order accurate in time, even if we solve the sub-problems with a higher order method. Higher order splitting method can be obtained by combining higher order method for each sub-problem with the *Strang*-splitting procedure (LeVeque, 2002).

In our problem, we only need the stationary solution of the system of conservation laws with source terms Eq.(4.33). Moreover, the stationary solution must be computed at every iteration of the sand evolution problem. We hence privilege the computational efficiency of the first order methods with respect to the more expensive higher order methods.

In particular, if we consider the conserved variables ρ and $q = \rho u$, the system (4.33) assume the general form given in Eq.(4.34) with $\mathbf{U} = \left(\begin{smallmatrix} \rho \\ q \end{smallmatrix} \right)$, $\mathbf{F}(\mathbf{U}) = \left(\begin{smallmatrix} q \\ q^2/\rho \end{smallmatrix} \right)$ and $\mathbf{S}(\mathbf{U})$ a compact notation for the right hand side of Eq.(4.33).

We introduce the time step Δt_1 used for the discretization of the fictitious time t_1 such that $t_1^m = m\Delta t_1$, $m = 0, \ldots$, and the superscript notation $f^{n,m}$ indicates that we are considering the generic variable f at the m-th subiteration needed to find f^n.

The splitting scheme that we implement for the stationary solution of Eq.(4.33) reads:

1. Initialize the values of the conserved variables from previous time step: $\rho^{n,0} = \rho^{n-1}$ and $q^{n,0} = \rho^{n-1}u^{n-1}$.

2. For $m = 0, \ldots, \overline{m} - 1$, iterate the following steps until convergence is reached (we omit the superscript n for ease notation):

   (a) Solve the homogeneous advection problem given by Eq.(4.35) using the conservative finite volume method:

$$\mathbf{U}_j^* = \mathbf{U}_j^m + \frac{\Delta t_1}{\Delta x} \left[\mathbf{F}_{j-\frac{1}{2}}^m - \mathbf{F}_{j+\frac{1}{2}}^m \right] \tag{4.37}$$

where $\mathbf{F}_{j-\frac{1}{2}}^m = \mathcal{F}\left(\mathbf{U}_{j-1}^m, \mathbf{U}_j^m\right)$ is some numerical flux function.

(b) In each point, solve the system of two coupled ordinary differential equations (o.d.e.) given by Eq.(4.36), with initial conditions given by the previous calculations. Following the considerations on the global first order accuracy of the splitting scheme, we use the first order explicit Euler method:

$$\mathbf{U}_j^{m+1} = \mathbf{U}_j^* + \Delta t_1 \mathbf{S}(\mathbf{U}_j^*). \tag{4.38}$$

The stopping criteria is based on the evaluation of the relative increments between two iterations:

$$\max\left(\frac{\|\rho^{n,m+1} - \rho^{n,m}\|}{\|\rho^{n,0}\|}, \frac{\|q^{n,m+1} - q^{n,m}\|}{\|q^{n,0}\|}\right) < \varepsilon \tag{4.39}$$

where ε is a given tolerance.

3. Set $\rho^n = \rho^{n,\overline{m}}$ and $q^n = q^{n,\overline{m}}$, hence $\Gamma^n = \Gamma(\rho^n, q^n)$ is the stationary exchange term which is needed to update h^n to $h^{n+1/2}$ through Eq.(4.29).

The Jacobian matrix of the advection problem is $\partial \mathbf{F}/\partial \mathbf{U} = \begin{pmatrix} 0 & 1 \\ -q^2/\rho^2 & 2q/\rho \end{pmatrix}$, with coincident eigenvalues $\lambda_1 = \lambda_2 = q/\rho = u$. This can also be seen from Eq.(4.33), where the two conserved variables ρ and ρu are both advected with speed u. In the setting we are going to consider, as we will see in practical examples, the sand flux velocity u will also be a strictly positive value. Hence, following the considerations on the global first order accuracy of the splitting scheme, in Eq.(4.37) we choose the first order upwind numerical flux function:

$$\mathbf{F}_{j-\frac{1}{2}}^m = \mathbf{F}(\mathbf{U}_{j-1}^m), \tag{4.40}$$

which leads to the following practical computation:

$$\rho_j^* = \rho_j^m + \frac{\Delta t_1}{\Delta x}\left[q_{j-1}^m - q_j^m\right], \tag{4.41}$$

$$q_j^* = q_j^m + \frac{\Delta t_1}{\Delta x}\left[\frac{(q_{j-1}^m)^2}{\rho_{j-1}^m} - \frac{(q_j^m)^2}{\rho_j^m}\right]. \tag{4.42}$$

We now define the numerical discretization of the source terms at the right hand side of Eq.(4.33) which are necessary for the step given in Eq.(4.38). We recall from Eq.(3.18) that the exchange rate Γ is defined as the sum of the contributions of the impact exchange rate Γ_i and the direct aerodynamic entrainment Γ_a. Moreover, on the unerodible surface $h = 0$ and in the recirculating zone $s > h$, the direct aerodynamic entrainment Γ_a is null and the impact exchange rate Γ_i cannot be positive, since in these zones only net deposition can occur. These considerations must hold also at the discrete level.

Hence, given h^n, τ^n from Eq.(4.30) and the intermediate values ρ^* and $u^* = q^*/\rho^*$ from Eqs.(4.41)-(4.42), we calculate:

$$
\begin{cases}
\tau_{g0}^* = \dfrac{\rho^* g}{2\alpha}, \quad T^* = \dfrac{2\alpha}{gr} u^*, \\[2mm]
\Gamma_a^* = \min\left(\max\left(\gamma_a \dfrac{\tau^n - \tau_{g0}^* - \tau_{ta}}{\tau_{ta}}, 0\right), h^n \dfrac{\rho_{dune}}{\Delta t}\right), \\[2mm]
n^* = \begin{cases} 0, & \text{if } s^n > h^n \\[2mm] \min\left(1 + \tilde{\gamma}\dfrac{\tau^n - \tau_{g0}^* - \tau_t}{\tau_t}, \left(h^n \dfrac{\rho_{dune}}{\Delta t} - \Gamma_a^*\right)\dfrac{T^*}{\rho^*} + 1\right), & \text{otherwise,} \end{cases} \\[2mm]
\Gamma_i^* = \dfrac{\rho^*}{T^*}(n^* - 1),
\end{cases}
\tag{4.43}
$$
$$\text{(4.44)}$$

and finally update Eq.(4.38) at each sub-iterations:

$$
\rho^{m+1} = \rho^* + \Delta t_1 (\Gamma_a^* + \Gamma_i^*).
$$

The choice of $\min(\ldots, h^n \frac{\rho_{dune}}{\Delta t})$ in Eq.(4.43), and the similar procedure in Eq.(4.44), ensures not only that $\Gamma_a^* = 0$ and $n^* \leq 1$ if $h^n = 0$, but also that in each point of the domain we are not eroding more sediments than available; in fact, this choice guarantees that the updated sand surface profile $h^{n+1/2}$ finally obtained through Eq.(4.38) is strictly not negative.

We now describe the numerical discretization of the external forces acting on the saltation layer which constitute the the source term of the momentum conservation equation. In Sect.3.1.2 we defined these forces in the classical situation consisting in a saltation layer over the dune surface, but we still need to detail what happens to these equations in the recirculation zone. In practical conditions, the mass of sand which comes from the lee side of the dune is thrown through the brink and deposited on the slip face. Since in this zone the dynamic of the sand grains is dominated by gravity, the wind velocity responsible for the acceleration of the sand flux v_{eff} given in Eq.(3.21) can be neglected. As a consequence, the drag force f_{drag} given in Eq.(3.20) now decelerates the grains. Moreover, since the sand flux is no more saltating on the sand surface, both the gravitational and the friction forces f_{grav} and f_{bed} given in Eqs.(3.19) and (3.22) vanish.

These consideration can be summarized in the following practical computations: we first derive the shear velocity $u_*^n = \sqrt{\tau^n/\rho_{air}}$ from the wind shear stress profile τ^n given in Eq.(4.30), and then write the effective wind velocity responsible for drag acceleration as:

$$
v_{eff}^n = \begin{cases} 0 & \text{if } s^n > h^n, \\[2mm] \dfrac{u_{*t}}{\kappa}\left[\ln\dfrac{z_1}{z_0} + \dfrac{z_1}{z_m}\left(\dfrac{u_*^n}{u_{*t}} - 1\right)\right] & \text{otherwise.} \end{cases}
$$

4. NUMERICAL METHODS AND APPLICATIONS

The external forces are hence numerically computed by:

$$
\begin{cases}
f^*_{drag} = \rho^* g \dfrac{|v^n_{eff} - u^*|(v^n_{eff} - u^*)}{u_f^2} \\[2mm]
f^*_{bed} = \begin{cases} 0 & \text{if } s^n > h^n \\[1mm] -\dfrac{\rho^* g}{2\alpha} & \text{otherwise} \end{cases} \\[4mm]
f^*_{grav} = \begin{cases} 0 & \text{if } s^n > h^n \\[1mm] -\rho^* g D_x(h^n) & \text{otherwise,} \end{cases}
\end{cases}
$$

where, for the computation of the gravitational force f_{grav} due to sloped bed, we need to approximate the slope of the sand surface h_x. We choose the first order upwind finite difference

$$
h_x(x_j) \simeq [D_x(h)]_j = \frac{1}{\Delta x}(h_j - h_{j-1}),
$$

which is consistent with the choice performed in the discretization of the numerical flux of the advective part, see Eq.(4.40). In conclusion, the update of Eq.(4.38) at each sub-iteration reads:

$$
q^{m+1} = q^* + \Delta t_1 \left[f^*_{drag} + f^*_{bed} + f^*_{grav} + (\Gamma^*_i + \Gamma^*_a)\, u^* \right].
$$

The global stability of the splitting algorithm for stationary sand flux calculation depends on the stability of the single sub-step. The advection step is stable if Courant-Friedrichs-Lewy (CFL) condition:

$$
\Delta t_1 \leq \frac{\Delta x}{u}
$$

is satisfied. The step of resolution of the system of o.d.e. requires that the condition of absolute stability of the forward Euler method is satisfied, *i.e.*:

$$
|1 + \Delta t_1 \lambda_i| < 1, \qquad i = 1, 2, \tag{4.45}
$$

where λ_i are the eigenvalues of the Jacobian $\partial \mathbf{S}/\partial \mathbf{U}$. Considering the whole domain, the most limiting conditions hold inside the recirculation bubble. Here, the system of o.d.e. is suitably rewritten in term of the non conserved variables:

$$
\begin{cases}
\dfrac{\partial \rho}{\partial t} = -\dfrac{\rho}{T} = -\dfrac{rg}{2\alpha}\dfrac{\rho}{u}, \\[3mm]
\dfrac{\partial u}{\partial t} = -g\dfrac{u^2}{u_f^2},
\end{cases}
$$

and the eigenvalues of the Jacobian of the right hand side are the real values:

$$
\lambda_1 = -\frac{rg}{2\alpha}\frac{1}{u} \qquad \text{and} \qquad \lambda_2 = -2g\frac{u}{u_f^2}.
$$

Substituting the values of the parameters r, g, α and u_f, one find $\lambda_1 \simeq -\frac{12}{u}$ and $\lambda_2 \simeq -8u$. Hence the absolute stability condition (4.45) becomes:

$$\begin{cases} \Delta t_1 < \dfrac{2}{|\lambda_1|} \simeq \dfrac{u}{6}, \\ \Delta t_1 < \dfrac{2}{|\lambda_2|} \simeq \dfrac{1}{4u}. \end{cases} \qquad (4.46)$$

In practical situations, the saltation flux velocity does not exceed the value $u_{max} = 2\,\mathrm{m/s}$, whereas, in the recirculating zone, it can easily decrease of at least one order of magnitude. Hence the most limiting condition for the stability of the global splitting scheme is in general the first one in system (4.46).

At this point, all the iterative sub-steps for the stationary solution of Eq.(4.33) have been detailed. Hence, the stationary exchange rate Γ^n can be calculated and the sand surface evolves through Eq.(4.29). The obtained surface $h^{n+1/2}$ in general violate the point-wise constraint on the maximum admitted slope. Hence, at this stage of the computations, we must relax the surface to finally obtain:

$$h^{n+1} + \partial I_k(h^{n+1}) \ni h^{n+1/2}.$$

For the relaxation procedure, we can use one of the algorithm introduced in Sect.4.1. For its computational efficiency, we would in general prefer the algorithm based on the entrainment-deposition formulation.

We now provide the results of some numerical simulations of two dimensional dunes evolution.

4.2.2 Numerical simulations

The simplest way to obtain a two dimensional numerical dune is to impose an initial sand surface profile $h^0(x) \geq 0$ and let it evolve towards the stationary travelling shape. The other input parameter of the model is the undisturbed wind shear velocity u_{*0} which determines the undisturbed wind shear stress $\tau_0 = \rho_{air} u_{*0}^2$ necessary in Eq.(4.30) to calculate the shear stress field on the sand surface.

Example 6   We consider the horizontal domain $x \in (0, 80)$m subdivided in $N_x = 128$ sub-intervals of equal length. The initial profile is given by the symmetric profile:

$$h^0(x) = \begin{cases} H_0 \cos^2\left(\dfrac{\pi}{30}(x - 20)\right) & \text{if } x \in [5, 35], \\ 0 & \text{otherwise,} \end{cases} \qquad (4.47)$$

where H_0 is the initial height and the initial length is $30\,\mathrm{m}$. The undisturbed wind shear velocity is $u_{*0} = 0.5\,\mathrm{m/s}$. The time step for surface evolution equation (4.29) is $\Delta t = 2\,\mathrm{min}$, while the time step for the sub-iterations for stationary sand flux calculation of Eq.(4.33) is $\Delta t_1 = 0.01\,\mathrm{s}$. The required tolerance for the convergence criterion (4.39) is $\varepsilon = 10^{-6}$, and in average the convergence is achieved in ~ 20 sub-iterations.

We vary the initial height $H_0 = 1.5$, 2, 2.5 and $3\,\mathrm{m}$ and let the model evolve towards the travelling dune solution. In Fig.4.9 we report the obtained profiles at time interval of $1\,\mathrm{day}$, up to the final time $T_{\max} = 20\,\mathrm{days}$. All the four initial profiles evolves in a travelling dune with slip face. However, the smaller is the dune, the higher is the velocity of advancement. These numerical results are summarized in Tab.4.1.

H_0	1.5 m	2 m	2.5 m	3 m
H_{staz}	2 m	2.35 m	2.68 m	2.97 m
v_{staz}	800 m/y	695 m/y	615 m/y	560 m/y

Table 4.1: **Relevant results of numerical simulations of Example 6** - For the given height H_0 of the initial profile (4.47), the height H_{staz} and the velocity v_{staz} of the stationary travelling dune is reported.

For the stationary dune obtained with $H_0 = 2.5\,\mathrm{m}$, we report in Fig.4.10 the main variables of the model. The density of sand in saltation ρ increases starting from the foot of the dune, because of increasing shear velocity on the lee side, and this imply the erosion of the latter. After the brink, the wind shear velocity u_* is set to zero in the recirculation zone through Eq.(4.30), and this imply that both the density ρ and the velocity u of the saltation flux decreases. The minimum saltation flux velocity inside the recirculation zone is $u_{min} \simeq 0.2\,\mathrm{m/s}$; this value, through Eq.(4.46), justifies the choice of Δt_1.

4.3   Marked sand dispersion in two dimensional dunes

In the two dimensional setting, the system of conservation equations (3.34) which describes the evolution of marked sand concentration in the saltation flux f_t and in the active layer f_a is written as:

$$\begin{cases} (f_t\rho)_t + (f_t\rho u)_x = \tilde{\Gamma} & (4.48) \\ \rho_{dune}\left[(L_a f_a)_t + f_I(h - L_a)_t\right] = -\tilde{\Gamma}, & (4.49) \end{cases}$$

where the exchange rate $\tilde{\Gamma}$ is given by Eq.(3.35), the interface concentration f_I is defined in Eq.(3.29) and the whole system is coupled with Eq.(3.31) which tracks the marked sand concentration in the sedimentary column through depositional processes.

In Sect.3.2.2, we have characterized the parameter of the model: in particular we have found that the active layer thickness L_a is of the order of some sand grain's diameters.

(a) $H_0 = 1.5\,\text{m}$

(b) $H_0 = 2\,\text{m}$

(c) $H_0 = 2.5\,\text{m}$
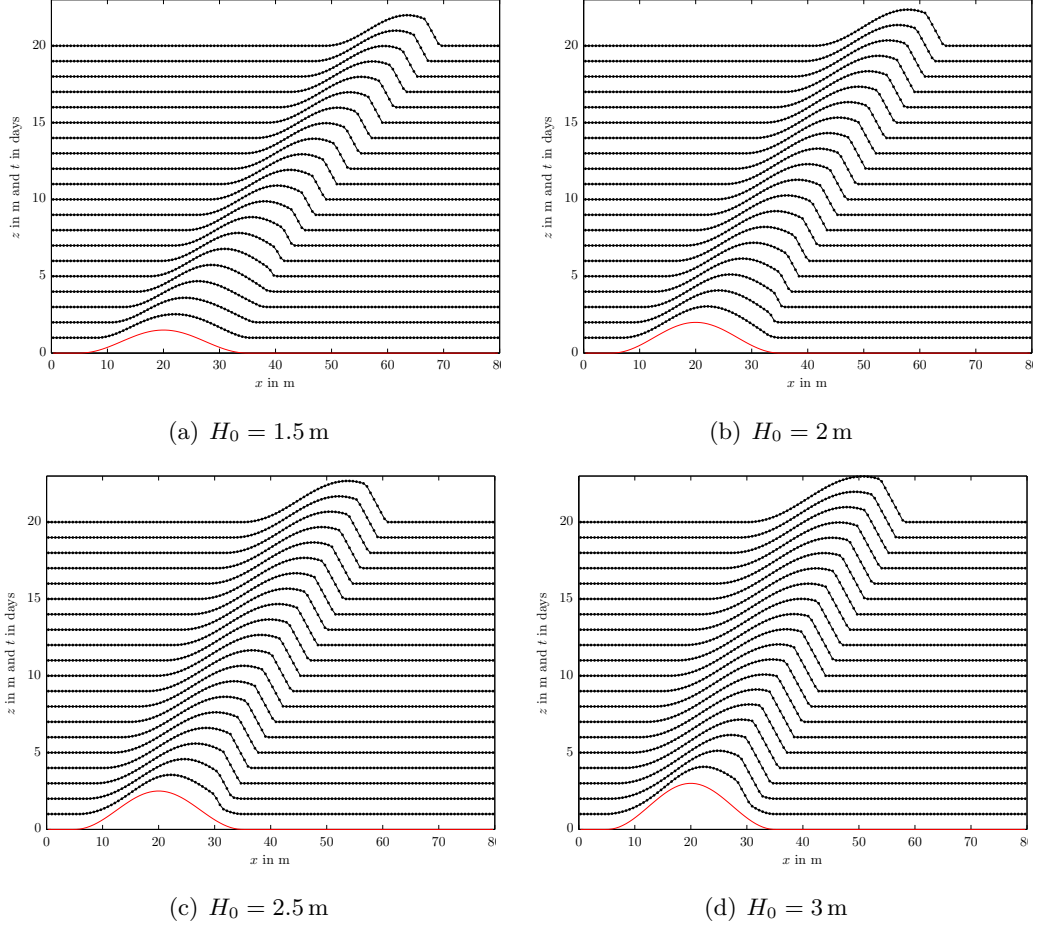
(d) $H_0 = 3\,\text{m}$

Figure 4.9: Evolution of the sand dune model for different initial conditions
- The initial profile is given by Eq.(4.47), with the undisturbed shear velocity given by
$u_{*0} = 0.5\,\text{m/s}$. With four different initial height H_0, the initial symmetric surface profile
evolves to a full developed travelling dune with slip face. Note that the velocity is higher
for smaller dune. Each profile is plotted at time interval of 1 day.

This means that the two equations (4.48)-(4.49) evolves at a comparable time scale. In
fact:

$$\frac{T(f_a)}{T(f_t)} = \frac{\rho_{dune}\mathcal{O}(L_a)/\mathcal{O}(\tilde{\Gamma})}{\mathcal{O}(\rho)/\mathcal{O}(\tilde{\Gamma})} \sim \frac{\mathcal{O}(10^3\,\text{Kg/m}^3)\mathcal{O}(10^{-4}\,\text{m})}{\mathcal{O}(10^{-2}\,\text{Kg/m}^2)} = \mathcal{O}(10). \qquad (4.50)$$

The numerical solution of the coupled problem is affordable in very simplified situation,
such as the experimental conditions described in Willetts & Rice (1988) experiment,
already seen in Sect.3.2.2. It consists in an horizontal sand bed with homogeneous
saturated sand flux, with a patch of marked sand initially positioned in a zone of the
domain. Since no net erosion occurs in the whole domain, the system takes the form
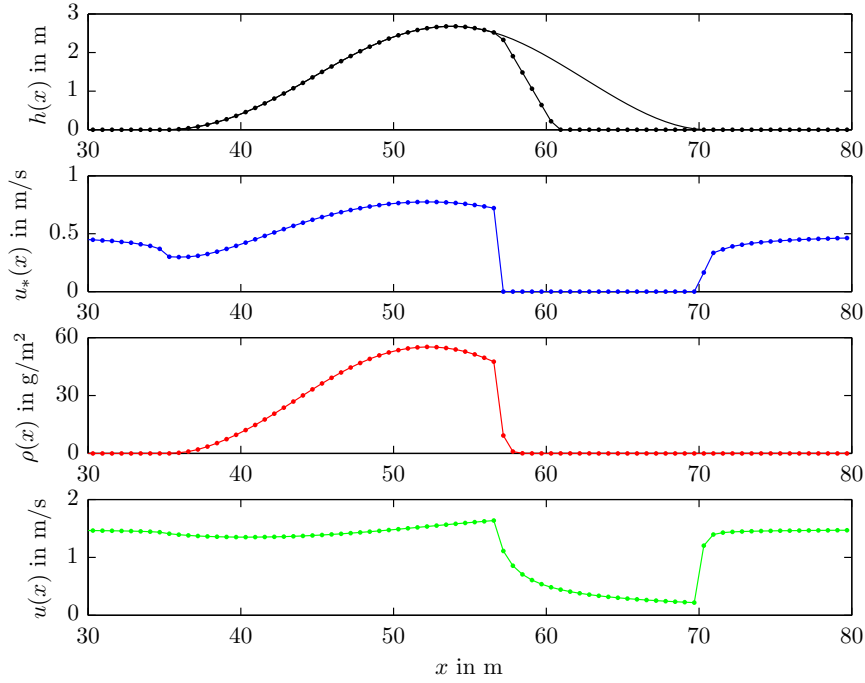given in Eq.(3.37).

89

Figure 4.10: Variables of the model on a stationary dune - From the top: dune surface profile and separating streamline, wind shear velocity, saltation flux density and velocity.

This system of coupled conservation laws can be solved with the operator splitting method already introduced in Sect.4.2.1. In particular, adopting the typical discretization of the horizontal domain $(0, L)$ and of the time interval $t \in [0, T_{\max}]$, we solve alternatively the advection problem from time t^n to t^{n+1} in each cell using the upwind flux:

$$[f_t^*]_i = [f_t^n]_i - u_{sat} \frac{\Delta t}{\Delta x} \left([f_t^n]_i - [f_t^n]_{i-1} \right), \qquad \text{for} \quad i = 1, \ldots, N_x,$$

to obtain the intermediate value f_t^*, and the system of coupled o.d.e. with initial condition given by f_t^* and f_a^n, from time t^n to time t^{n+1} using the explicit Euler method:

$$\begin{cases} f_t^{n+1} &= f_t^* + \Delta t \dfrac{1 - p_{reb}}{T} (f_a^n - f_t^*), \\ f_a^{n+1} &= f_a^n - \Delta t \dfrac{\rho_{sat}}{\rho_{dune} L_a} \dfrac{1 - p_{reb}}{T} (f_a^n - f_t^*). \end{cases}$$

In this splitting procedure, the value $[f_t]_0$ is the inlet boundary condition.

Example 7 In this numerical simulation, we replicate the condition of the experiment of Willetts & Rice (1988). Hence, we take the horizontal domain $x \in [0,1]$m and subdivide it in $N_x = 100$ cells. The initial active layer concentration of marked sand is:

$$f_a^0(x) = \begin{cases} 1 & \text{if } x \in [0.2, 0.3]\,\text{m} \\ 0 & \text{otherwise,} \end{cases}$$

while the initial and inlet transported concentration is null. We take the wind shear velocity $u_* = 0.24\,\text{m/s}$, as in one of the real experiments. We neglect the rebound probability ($p_{reb} = 0$), hence to match the parameters of Tab.3.1 we choose $L_a = 0.622d \simeq 0.15\,\text{mm}$. Here the choice of the time step is limited by the CFL condition, hence we choose $\Delta t = 0.25 \Delta x / u_{sat}$.

The results of the coupled dynamics, simulated on the time interval $t \in [0, 100]$ sec, are reported in Fig.4.11. The transported concentration increases over the initial patch to reach a maximum value ~ 0.5 at the downwind edge of the patch in the first instants of simulation. Then this peak is smoothed in time, due to the mixing processes. At the same time, the active layer concentration of marked sand in the initial patch decreases exponentially in time, as already supposed in Eq.(3.38).

We have seen that, a priori, the equations for the evolution of the concentrations in the active layer (4.48) and in the saltation flux (4.49) must be solved in a coupled way. But, in more complicate conditions that the horizontal homogeneous case investigated in Example 7, these equations must also be coupled with the system (4.26)-(4.27)-(4.28) which describes the spatio-temporal evolution of h, ρ and u. We notice that the equations of sand surface evolution and of active layer concentration must be solved at the same time scale, because the temporal derivative of h appears explicitly in (4.49). As a consequence, the whole coupled system must a priori be solved at the smallest time scale given by the sand transport dynamics. This would imply prohibitive computational costs, since computing the evolution of the sand surface with the time step needed for the solution of the sand transport is hard to achieve.

The only solution for this drawback is to decouple the equations for the evolution of the concentrations in the active layer (4.48) and in the saltation flux (4.49). This can be made only by assuming a large active layer width. Hence, in the following, we choose:

$$L_a = 100d = 25\text{mm}.$$

With this simple choice, the time scale ratio (4.50) becomes $\mathcal{O}(10^3)$, and hence the two equation can be decoupled. In particular, we can assume that the active layer concentration is stationary with respect to the sand transport concentration dynamics of Eq.(4.48).

These considerations lead to write the following global system for marked sand evolution
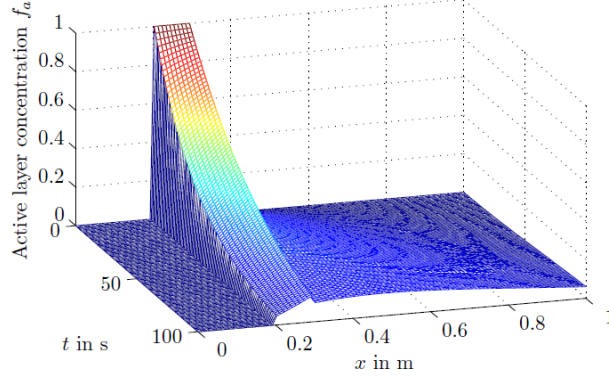
(a) $f_a(x,t)$
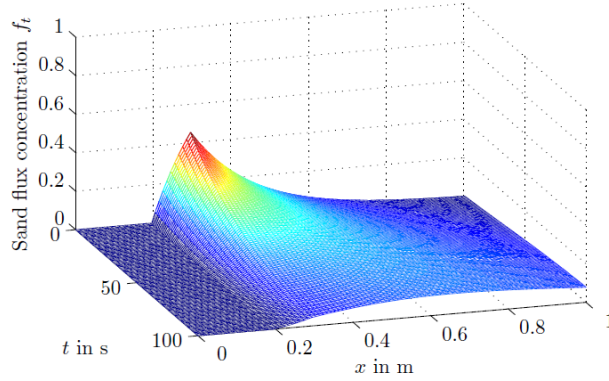
(b) $f_t(x,t)$

Figure 4.11: Simulation of Willetts & Rice (1988) experiment - The temporal and spatial evolution of the active layer concentration f_a and the transported concentration f_t are shown.

in two dimensional sand dune as:

$$
\begin{cases}
\rho_{dune} h_t = -\Gamma, \quad \text{s.t.} \quad |h_x| < \tan(\theta) & (4.51) \\
\rho_{dune} \left[L_a(f_a)_t + f_I h_t \right] = -\tilde{\Gamma}, & (4.52) \\
(\rho u)_x = \Gamma, & (4.53) \\
(\rho u u)_x = f_{drag} + f_{bed} + f_{grav} + \Gamma u, & (4.54) \\
(\rho f_t u)_x = \tilde{\Gamma}, & (4.55)
\end{cases}
$$

where the interface concentration f_I is given by Eq.(3.29) and at the same time the equation for marked sand conservation in the substrate (3.31) holds.

Here the equations for sand surface (4.51) and for the concentration in the active layer (4.52) describe an evolution at the same macroscopic time scale t. The equations for

the transport layer involving its density (4.53), momentum (4.54) and marked sand concentration (4.55) describe a process happening at the microscopic time scale $t_1 \ll t$, and hence their temporal derivative can be neglected with respect to the macroscopic time scale t.

The numerical approximation of this system can be developed with the same technique adopted in Sect.4.2.1. Besides the equation of evolution of the sand surface (4.29), we update the equation for the concentration in the active layer (4.52) with the explicit Euler method:

$$f_a^{n+1/2} = f_a^n + \frac{\Delta t}{\rho_{sand} L_a} \left(-\tilde{\Gamma}^n + f_I^n \Gamma^n \right) \qquad (4.56)$$

where the superscript $n + 1/2$ indicates that at this stage the sand surface, and hence the superficial concentration of marked sand, has not been relaxed by the avalanche process yet.

Since the evolution of the marked sand concentration in the active layer depends, through the interface concentration f_I, also on the exchange of sediments with the substrate, it is necessary to store the marked sand concentration in the substrate $f_b(x, z)$ during the computation. Assuming that at all times $H_{min} < h < H_{max}$, we consider a subdivision of the vertical domain $z \in (H_{\min}, H_{\max})$ in N_z intervals of equal size Δz. The midpoints $z_i = H_{\min} + (i - 0.5)\Delta z$, $i = 1, ..., N_z$ are the discretization points of the vertical domain. The whole domain $[0, L] \times [H_{\min}, H_{\max}]$ is therefore discretized in $N_x \times N_z$ rectangular cells where (x_i, z_j) are the coordinates of the center points. The substrate concentration is constant in each cell and its values are stored in a matrix $\mathbf{F}_b$ such that $[\mathbf{F}_b]_{ij} \simeq f_b(x_i, z_j)$.

During evolution, in the zones characterized by net erosion of sediments the interface concentration f_I^n is the substrate concentration $\mathbf{F}_b^n$ of the cell crossed by the interface. In the zones characterized by net deposition, the interface concentration f_I^n is the concentration in the active layer f_a^n, and the substrate concentration in the cells crossed by the interface has to be updated according to the scheme represented in Fig.4.12 because they incorporate new sediments from the active layer.

The exchange rate of marked sand between the sand surface and the transport layer $\tilde{\Gamma}^n$ is given by the stationary solution of equation:

$$(\rho f_t)_{t_1} + (\rho f_t u)_x = \tilde{\Gamma}, \qquad (4.57)$$

which is computed at the same sub-iteration steps used for the solution of system (4.33). Even in this case, the operator splitting algorithm introduced in Sect.4.2.1 is used. We here recall that the exchange rate of marked sand is given by Eq.(3.35) and that, thanks to the decoupling procedure, in the effective iterations of Eq.(4.57) the known value f_a^n is used.
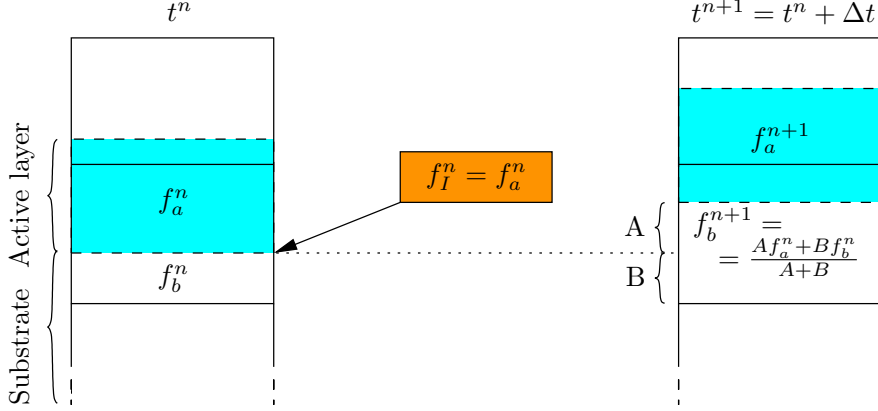
Figure 4.12: Substrate concentration update - Discrete technique for the passage of marked sand from the active layer to the substrate in the case of net deposition; the new substrate concentration is a weighted mean between the old substrate concentration and the active layer concentration.

4.3.1 Sand avalanches with marked sand

From Sect.4.1.2, we know how to relax a steep sand surface with an entrainment-deposition formulation: given $u^0 = h^{n+1/2}$, we iterate

$$u^{k+1} = u^k + \Delta t_{av} \left(\mathcal{D}^k - \mathcal{E}^k \right). \tag{4.58}$$

until the surface is effectively relaxed. The active layer formulation can be used to describe the avalanche process too. In particular, starting from $f_a^0 = f_a^{n+1/2}$ calculated in Eq.(4.56), we iterate together with Eq.(4.58) the equation:

$$f_a^{k+1} = f_a^k + \frac{\Delta t_{av}}{L_a} \left(\tilde{\mathcal{D}}^k - \tilde{\mathcal{E}}^k - f_I^k \left(\mathcal{D}^k - \mathcal{E}^k \right) \right),$$

where $\tilde{\mathcal{E}}^k = f_a^k \mathcal{E}^k$ is the entrainment rate of marked sand due to avalanches and $\tilde{\mathcal{D}}^k$, the deposition rate of marked sand due to avalanches, is calculated in each node of the grid i with the adapted version of Eq.(4.22)-(4.23):

$$\tilde{\mathcal{D}}_i^k = \sum_{j=0}^{N_x} \tilde{\mathcal{D}}_{i \leftarrow j}^k \qquad \text{with} \qquad \tilde{\mathcal{D}}_{i \leftarrow j}^k = \mathcal{S}_{i-j} \tilde{\mathcal{E}}_j^k = \mathcal{S}_{i-j} \mathcal{E}_j^k f_{a,j}^k.$$

Here we examine the behaviour of the model of sand avalanches with marked sand in a simplified test case.

Example 8 We consider the domain $x \in [0,2]$m subdivided in 200 equally spaced cells of width $\Delta x = 1$ cm and an initial sand pile with surface profile: $h(x,0) =$

$\max(\cos(\frac{\pi}{2}x), 0)$, which clearly exceeds the maximum admitted slope. We discretize the vertical domain $z \in (-0.1, \ 1.2)$ m in 130 intervals of height $\Delta z = 1$ cm. On this domain, we initialize the marked sand concentrations to the values $f_a(x, 0) = f_b(x, y, 0) = 1 - x$, as represented in Figure 4.13(a). We use an exponential p.d.f. $\mathcal{S}(r)$ for rolling grains with mean $\lambda = 5$ cm, and define the width of the active layer $L_a = 2.5$ mm, equal to 10 times the diameter of a sand grain. In Figure 4.13(b) we can note that the model reproduces a reasonable final sedimentary structure of the collapsed sandpile. In the final solution, the deeper layers of final sedimentary structure are made with sand which comes from the lower part of the initial sandpile, and this is noticeable by a lower concentration of marked sand. On the contrary, the upper layers of the collapsed sandpile come from the upper part of the initial sandpile.
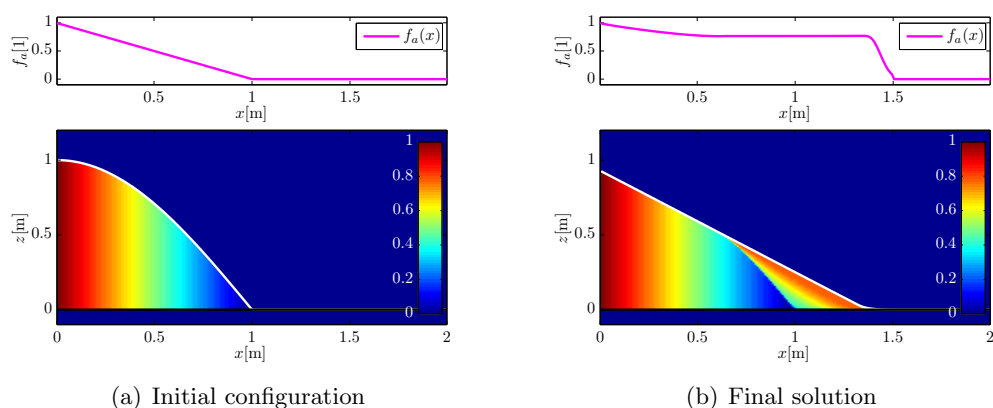

(a) Initial configuration   (b) Final solution

Figure 4.13: Simulation of the active layer model coupled with the avalanche model - In the upper part is reported the profile of the marked sand concentration in the active layer f_a, in the lower part the concentration of marked sand in the substrate $\mathbf{F}_b$.

The complete dynamics of the model of marked sand evolution in sand dunes can be now evaluated with a numerical example.

Example 9 We consider the initial symmetric profile given by Eq.(4.47) with initial height $H0 = 2$ m. The computational domain $(x, z) \in [0, 80]$ m $\times [-0.5, 3]$ m is discretized in $N_x \times N_y = 128 \times 240$ cells. The initial substrate concentration is

$$f_b(x, z, 0) = \begin{cases} 1 & \text{if } 5 \leq x \leq 20, \ 0 \leq z \leq h^0(x), \\ 0 & \text{otherwise,} \end{cases}$$

that is equal to 1 in the left half of the initial profile, see Fig.4.14. The initial active layer concentration is also given by:

$$f_a(x, 0) = \begin{cases} 1 & \text{if } 5 \leq x \leq 20, \\ 0 & \text{otherwise.} \end{cases}$$

The others parameters of the model are taken as specified in Example 6. The evolution of the surface profile hence will be equal to the graph shown in Fig.4.9(b), but now we simulate also the evolution of the concentration of marked sand inside the dune. The results are shown in Fig.4.14. The model is able to capture the sedimentary pattern formed during dune evolution. In the first stages of the simulation, the marked sand which forms the left half of the dune is deposited over the right half. Then, advancing with the evolution, the zones formed by non marked sand are uncovered, and the mixing between the two families of sediments takes place. At the final stages of the simulation, after one complete turnover of the dune, the two families of sands are well mixed, hence the final concentration of marked sand inside the dune is almost constant and equal to one half.
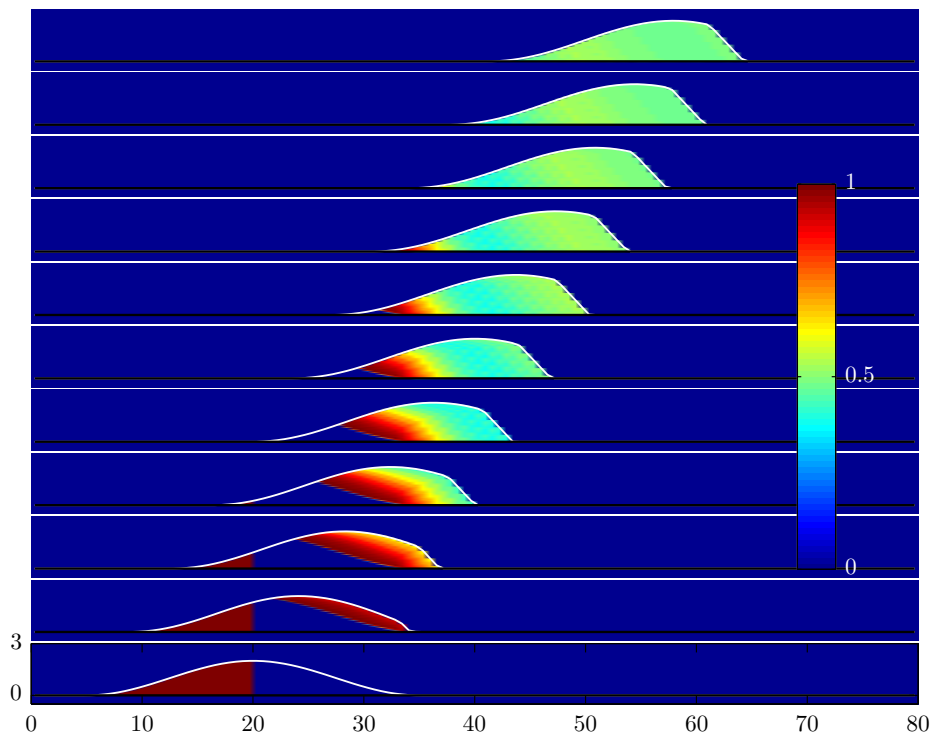

Figure 4.14: Evolution of a sand dune with marked sand - The left half of the initial profile is formed by marked sand. The advancement of the dune causes a mixing of the two families of sand, and the final concentration profile inside the dune is almost constant and equal to 0.5.

5

A simplified model for the evolution of two dimensional dunes

In this Chapter we develop a simplified model for the evolution of two dimensional dunes. With respect to the modelling of Chap.3, we propose a simplified version of the entrainment and deposition rates of sand due to saltation. This will lead to a computationally efficient numerical model, particularly adapt to the simulation of problems involving large spatial and temporal scales. The main feature of this simplified model are published in (Pischiutta *et al.*, 2011).

5.1 Sand transport and desert surface evolution

The sand surface elevation is described by a function $z = h(x, t)$, z being the vertical coordinate. In this Chapter we consider the evolution of a two-dimensional dune only. The evolution of the sand surface will be directly determined in function of the mass sand flux $q(x, t)$ of sand grain in saltation, that is the mass of sand that crosses the position x per unit time. Hence we will bypass the determination of the density ρ and velocity u of the sand flux.

The continuity equation which ensures mass conservation is obtained directly form Eq.(3.23)

$$\rho_{dune}\frac{\partial h}{\partial t} + \frac{\partial q}{\partial x} = 0, \qquad (5.1)$$

where ρ_{dune} is the density of the sand bed given by $\rho_{dune} = (1 - \lambda)\rho_{sand}$, where λ is the porosity of sand bed, here assumed constant. We need to express the flux $q(x, t)$ in terms of the height profile $h(x, t)$ and the action of external wind. As we have already seen in Sect.3.1, since the speed of evolution of the surface is very small compared to that of sand transport, the topography can be assumed to be stationary with respect to the wind and sand transport dynamics. This assumption allows us to calculate the stationary flux $q(x)$ by the following steps:

5. A SIMPLIFIED MODEL FOR THE EVOLUTION OF TWO DIMENSIONAL DUNES

1. calculate the stationary wind velocity above the given topography; more precisely we need the shear velocity $u_* = u_*(x)$ or equivalently the shear stress $\tau = \rho_{air} u_*^2$ exerted by the wind on the sand surface;

2. calculate the stationary sand flux $q(x)$ for a given $\tau(x)$.

5.1.1 Shear stress calculation

We have seen in Sect.3.1.1 that the determination of the shear stress $\tau(x)$ is a rather complex problem due to the complex fluid dynamics in the atmospheric boundary layer in presence of saltating sand grains, and to the possible presence of a recirculation zone in the downwind part of a dune profile. In the areas not interested by recirculation we assume that the presence of the relief $h(x)$ induces a perturbation of the shear stress exerted by the wind with respect to that of a horizontal surface $\tau_0 = \rho_{air} u_{*0}$. We introduce then $\hat{\tau}(x) \equiv \tau(x)/\tau_0 - 1$, and we first consider the case of a smooth sand bump without recirculating zone. The shear stress perturbation $\hat{\tau}$ can be calculated by adapting the result of the analytic theory of boundary layer perturbation given in Eq.(3.8) to the two dimensional case. Moreover, we can approximate the logarithmic term $\ln L|k| \approx \ln 1/4$ by the constant value that corresponds to the wave length $4L$ of the hill and obtain:

$$\mathcal{F}[\hat{\tau}](k_x) = (A|k_x| + iBk_x)\, \mathcal{F}[h](k_x) \tag{5.2}$$

where

$$A = \frac{2}{U^2(l)}\left(1 + \frac{2\ln 1/4 + 4\epsilon + 1}{\ln(l/z_0^{dune})}\right) \quad \text{and} \quad B = \frac{2}{U^2(l)}\frac{\pi}{\ln(l/z_0^{dune})}.$$

The result of Eq.(5.2) can be directly written in the spatial variable:

$$\hat{\tau}(x) = A\int_{\mathbb{R}} \frac{1}{\pi\chi}\partial_x h(x - \chi)\, \mathrm{d}\chi + B\partial_x h(x) = \hat{\tau}_A + \hat{\tau}_B. \tag{5.3}$$

Here the shear stress perturbation $\hat{\tau}$ depends only on the slope of the hill $\partial_x h$, reflecting the consideration that a turbulent flux is scale-invariant. The convolution integral is a non local term that depends on the whole shape of the dune. Its contribution is positive on bumps (negative curvature) and negative on hollows (positive curvature). The second term takes into account the slope effects, as the shear stress increases on positive slopes because of streamline compression. The combined effects of these two contributions leads to an asymmetric shear stress even on a symmetric sand surface profile; in particular, the maximum of $\tau(x)$ is always shifted upwind with respect to the maximum of $h(x)$, see Figure 5.1(a). The value of the coefficients A and B is found in the cited literature (Kroy *et al.*, 2002).

In the case of the atmospheric boundary layer, the scale invariance is broken by the existence of the superficial roughness z_0^{dune}, and the coefficients A and B of the model are not strictly constant but depend on $\ln(L/z_0^{dune})$, where L is the dune size. Notwithstanding, taking the coefficients as effective constant will not affect the overall behaviour

(a) $\hat{\tau}(x)$ on a symmetric bump

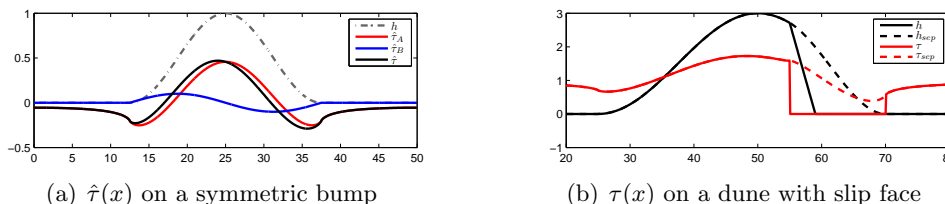(b) $\tau(x)$ on a dune with slip face

Figure 5.1: In (a), in black is represented the shear stress perturbation $\hat{\tau}$ on the profile h; in red $\hat{\tau}_A$, the non-local term expressed by the convolution integral, in blue the slope term $\hat{\tau}_B$. The values of the parameters are $A = 4$, $B = 1$. In (b), in black is represented the dune profile h; from the brink point, the separating streamline (dashed black line) is empirically built as a polynomial of 3rd degree. Then the shear stress (dashed red line) is calculated using equation (5.3) on the profile which includes the separating streamline, and finally it is set to zero in the recirculating zone (red line).

of the model; further consideration in this direction can be found in (Andreotti *et al.*, 2002a,b).

When the sand surface presents a slip face the wind flow separates at the brink of the dune and reattaches downwind. This phenomenon creates a recirculating zone in the lee side of the dune, which cannot be modelled by the analytical perturbation method. We have seen in Sect.3.1.1 that a simple way to model the effect of the recirculation bubble on the overall flux is to empirically reconstruct the separating streamline and to assume that the wind flow follows it as a solid surface. In the recirculation zone the shear stress is then assumed to be negligible, see Figure 5.1(b). Following Sauermann *et al.* (2001); Andreotti *et al.* (2002b), the separation streamline is written as a polynomial of 3rd degree with smooth C^1 junction at brink and reattachment point. The length of the separation bubble is determined by imposing the fixed maximum slope of $\tan 14°$ at the inflexion point.

This extremely simplified method for shear stress calculation can reproduce the overall behaviour of the wind flux over a sand dune, saving a lot of computational time with respect to other methods. Since computing the shear stress by a CFD code is rather expensive, in the following we will use the proposed analytical expression for the shear stress.

5.1.2 Sand flux calculation

Wind blowing over a surface covered by sand mobilizes sand grains laying on the surface. Those grains accelerate extracting momentum from the wind flow and entrain other grains when they impact on the sand bed. In this process, the wind velocity in the surface layer is reduced. This feedback mechanism establishes a relation between the shear velocity u_* and the sand flux q at equilibrium. A single empirical relation has been proposed by Bagnold (1941):

$$q_{sat} = C_B \frac{\rho_{air}}{g} u_*^3, \tag{5.4}$$

5. A SIMPLIFIED MODEL FOR THE EVOLUTION OF TWO DIMENSIONAL DUNES

where the index *sat* in Eq.(5.4) emphasizes that this relation is valid when the flux is saturated, *i.e.* it is equal to its equilibrium transport capacity. Here C_B is a constant parameter usually taken equal to 2 , ρ_{air} is the density of the air and g is the gravity acceleration. Many other laws have been discussed in the literature, mainly to include a threshold value for the shear velocity u_{th} in the formulation, indicating that below u_{th} the wind cannot mobilize the sand grains, but the scaling $q_{sat} \propto u_*^3$ is common to all models for u_* sufficiently far from the threshold value, see Fig.2.3.

In field conditions not all the ground is covered by sand, moreover we have the presence of sloped beds and reattachment points. Therefore q_{sat} depends on x because $u_* = u_*(x)$, and the sand flux q is not everywhere equal to its saturated value given in Eq.(5.4). In fact, the flux adapt to changes in external conditions with a characteristic space lag, called saturation length L_{sat}. This space lag can be described Andreotti *et al.* (2002b) by a charge equation of the form:

$$\frac{\partial q}{\partial x} = \frac{q_{sat} - q}{L_{sat}}. \tag{5.5}$$

The sand flux can increase only if some grains are available on the unerodible bed, *i.e.* if $h(x) > 0$. On the firm soil the flux cannot increase to become saturated and remains constant.

Among the possible physical mechanisms responsible for the saturation length proposed in the literature, the most accredited is the distance required by the wind to accelerate the grain expelled from the surface and the value of this distance is taken proportional to the diameter of the grain times the ratio between the density of sand and air (Andreotti *et al.*, 2002a): $L_{sat} = \xi \frac{\rho_{sand}}{\rho_{air}} d$. The value of the constant of proportionality $\xi \simeq 2$ was obtained recently (Andreotti *et al.*, 2010) by adapting the charge equation (5.5) to experimental measurements conducted in a wind tunnel and appears to be independent from the strength of the wind. Characteristic values are $\rho_{sand} = 2650 \, \text{kg/m}^3$, $\rho_{air} = 1.225 \, \text{kg/m}^3$, $d = 0.25 \, \text{mm}$, which lead to $L_{sat} = 1 \, \text{m}$.

The charge equation (5.5) can also be obtained from the complete modelling of Chap.2. In particular if we assume that the flux velocity is always equal to its saturated value u_{sat} given in Eq.(2.32), the stationary mass conservation equation (2.26) can be rewritten as:

$$\frac{\partial}{\partial x} q = \frac{q}{L_{sat}} \left(1 - \frac{q}{q_{sat}} \right), \tag{5.6}$$

with $q = \rho u_{sat}$, $q_{sat} = \rho_{sat} u_{sat}$ and $L_{sat} = T_{sat} u_{sat}$. The linear charge equation (5.5) is hence obtained from linearization of Eq.(5.6) near q_{sat}.

5.1.3 Numerical approximation

The basic mathematical model for sand dune evolution is finally formed by the following equations (Andreotti *et al.*, 2002b; Hersen, 2004)

$$
\begin{cases}
\rho_{dune}\dfrac{\partial h}{\partial t} + \dfrac{\partial q}{\partial x} = 0 \qquad \text{s.t.} \quad |\partial_x h| < \tan(\theta) \\[2ex]
\dfrac{u_*^2(x)}{U_*^2} = \dfrac{\tau(x)}{\tau_0} = 1 + A \displaystyle\int \dfrac{1}{\pi\chi}\partial_x h(x - \chi)d\chi + B\partial_x h(x) \\[2ex]
q_{sat}(x) = C_B \dfrac{\rho_{air}}{g} u_*^3(x) \\[2ex]
\dfrac{\partial q}{\partial x} = \dfrac{q_{sat} - q}{L_{sat}} \quad \text{where} \quad h > 0, \quad \dfrac{\partial q}{\partial x} = \min\left(\dfrac{q_{sat} - q}{L_{sat}}, 0\right) \quad \text{otherwise,}
\end{cases}
\tag{5.7}
$$

where in the first equation we impose that the slope of the sand surface cannot exceed the angle of repose $\theta = 34°$ during evolution.

Concerning the numerical solution of (5.7), an initial profile $h(x, 0)$ is imposed and the domain $\Omega = [0, L]$ is divided in N intervals of uniform length Δx. The algorithm for the evolution of the system reads:

1. if the sand surface presents a slip face, then reconstruct the separating streamline $s(x)$ using a 3rd order polynomial starting from the brink and reattaching downwind with a C^1 junction. The reattachment point is determined by imposing a slope at the inflection point of the streamline equal to $\tan 14°$, following (Kroy *et al.*, 2002; Andreotti *et al.*, 2002b).

2. Solve the equation (5.2) for $\tau(x)$, using the Fast Fourier Transform, over the profile $\max(h, s)$ which eventually includes the separating streamlines. Then set $\tau = 0$ in the recirculating zones and deduce the profile of $q_{sat}(x)$ from the profile of $\tau(x)$.

3. The charge equation for $q(x)$ is an o.d.e. in space which is solved with the Heun method (2nd order accurate explicit). An inflow boundary condition $q(0, t)$ must be provided.

4. For the temporal evolution of the surface, the time derivative is discretized with the forward Euler method, and the space derivative $\partial_x q$ with a WENO (Shu, 2009) derivation, as we want to limit oscillation induced by a numerical differentiation of the profile of $q(x)$, which is only C^0 at the brink points. The profile obtained at this stage is indicated as $h^{n+1/2}$.

5. The suffix $n+1/2$ is used to indicate that surface thus obtained is an intermediate solution as we still have to impose the constraint on the norm of the gradient. The solution that we adopted for this problem has been detailed in Sect.4.1.

The model can be applied to the evolution of an initial symmetric profile of sand to a moving dune with slip face as we are going to see in the following Section.

5.1.4 Simulations

We choose an initial surface profile of the form:

$$h(x,0) = \begin{cases} H_0 \cos^{5/3}\left(\dfrac{2\pi}{L_0}(x-C_0)\right) & \text{for } C_0 - \dfrac{L_0}{2} \le x \le C_0 + \dfrac{L_0}{2}, \\ 0 & \text{otherwise,} \end{cases} \tag{5.8}$$

where H_0 and L_0 are the height and the length of the initial profile. For $H_0 = 2\,\text{m}$ and $L_0 = 30\,\text{m}$, we report in Fig.5.2 the stationary sand flux obtained by varying the wind shear velocity, assuming a null inflow flux. We notice that, on such profiles without slip face, there is a non vanishing sand flux leaving the domain. To maintain the total mass of sand, we should impose periodic boundary conditions at the boundaries of the domain.
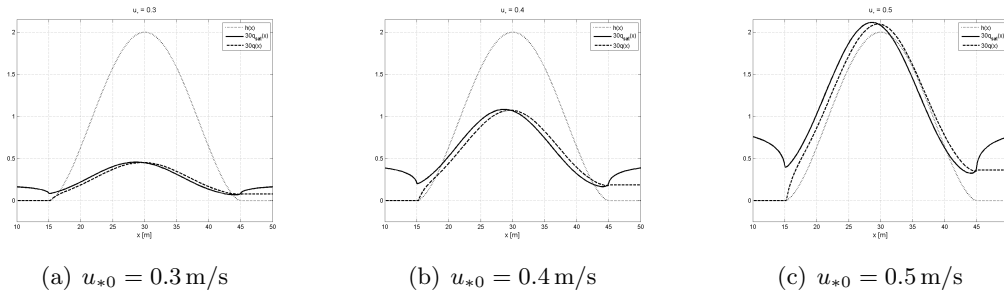

(a) $u_{*0} = 0.3\,\text{m/s}$ (b) $u_{*0} = 0.4\,\text{m/s}$ (c) $u_{*0} = 0.5\,\text{m/s}$

Figure 5.2: Sand flux for varying shear velocity u_{*0} - On the symmetric profile given by Eq.(5.8), the sand flux is calculated for different shear velocity and null inflow flux.

As $q_{sat} \propto u_*^3$, the maximum transport flux increases rapidly with u_*. This leads to different advancing velocities for the sand dune, as we can see in Fig.5.3. We observe that the initial surface first rises augmenting its slope, then develops the slip face and hence propagates like a standing wave. In the case of null inflow flux $q(0)$, the existence of the slip face is mandatory for the existence of the standing wave solution.
In Fig.5.4 we verify that, for constant shear velocity, by diminishing the initial height we first obtain a faster dune for $H_0 = 1.5\,\text{m}$, and then for $H_0 = 1\,\text{m}$ the slip face does not form and all the sand is eroded from the domain.

This result agrees with observation: in fact, a minimal size for sand dunes exists (Parteli *et al.*, 2007a; Andreotti & Claudin, 2007; Parteli *et al.*, 2007b). This is due to the saturation length L_{sat}: in fact, to have a standing wave solution, the maximum of $q(x)$ must coincide with the maximum of $h(x)$, so that the summit of the dune will not be eroded. But the maximum of the shear stress $\tau(x)$, and hence of the saturated sand flux $q_{sat}(x)$, is always shifted upwind with respect to the dune summit. This shift is proportional to the dune dimension, for the scale invariance of the shear stress. On

(a) $u_{*0} = 0.3 \, \text{m/s}$ (b) $u_{*0} = 0.4 \, \text{m/s}$ (c) $u_{*0} = 0.5 \, \text{m/s}$
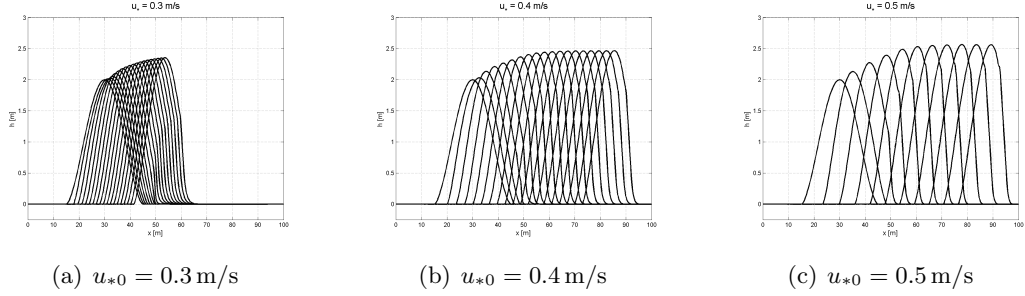
Figure 5.3: Dune evolution for varying shear velocity u_{*0} - The time lag between two images is 5 days.

(a) $H_0 = 2 \, \text{m}$ (b) $H_0 = 1.5 \, \text{m}$ (c) $H_0 = 1 \, \text{m}$
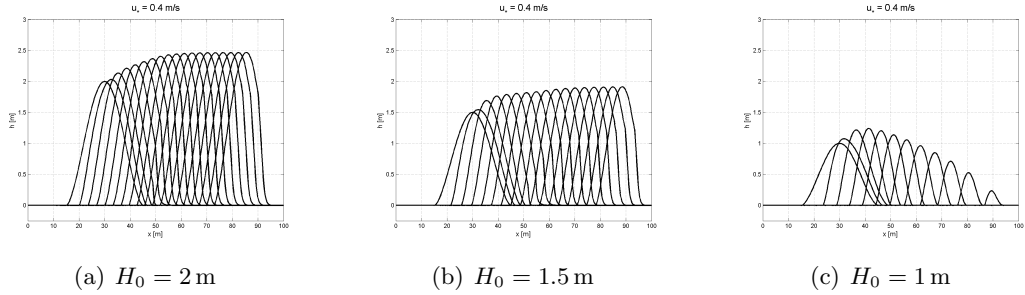
Figure 5.4: Dune evolution for varying initial height - Keeping the shear velocity $u_{*0} = 0.4 \, \text{m/s}$ constant, the evolutionary profiles depends on the initial height. The standing wave solution will not form for small initial height.

the other side, the charge equation implies that the sand flux $q(x)$ is shifted downwind with respect to $q_{sat}(x)$ with distance equal to L_{sat}. It results that, for too small dune, the sand flux profile is shifted downwind with respect to the height profile, see Fig.5.5, which implies the complete erosion of the dune.
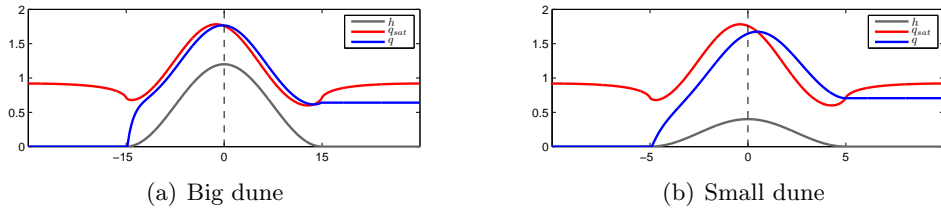

(a) Big dune   (b) Small dune

Figure 5.5: Effect of the saturation length - On two scale invariant surface profile (in grey), the profile of the saturated sand flux (in red) is equivalent (since the shear stress is scale invariant), but the saturation length adds a spatial delay which makes the evolution of a big dune (a) possible ($q(x)$ and $h(x)$ have a maximum at the same position) but is responsible for the complete erosion of the small sand dune (b) ($q(x)$ has a maximum shifted in the downwind part of the dune).

103

5.2 Marked sand dispersion

We are now interested in building a mathematical model for the dispersion of a mass of marked sand. Following the modelling framework of Sec.3.2, we adopt the active layer hypothesis. Defining with $\tilde{q}$ the flux of marked sand in saltation, the conservation equation of marked sand in the active layer reads:

$$\rho_{dune}\left[\frac{\partial(L_a f_a)}{\partial t} + f_I \frac{\partial(h - L_a)}{\partial t}\right] + \frac{\partial \tilde{q}}{\partial x} = 0. \tag{5.9}$$

where the interface concentration f_I is defined in Eq.(3.29) and, during deposition phenomena, the substrate concentration evolves through Eq.(3.31).
By assuming a constant active layer depth L_a, considering also Eq.(5.1), we rewrite Eq.(5.9) as:

$$\rho_{dune} L_a \frac{\partial f_a}{\partial t} - f_I \frac{\partial q}{\partial x} + \frac{\partial \tilde{q}}{\partial x} = 0. \tag{5.10}$$

At this point, we need an expression for the divergence of the flux of marked sand $\partial_x \tilde{q}$. As we have seen in Eqs.(3.32)-(3.33), this exchange term is equal to the balance between the entrainment and deposition rates of marked sand,

$$\frac{\partial \tilde{q}}{\partial x} = \tilde{E}(x) - \tilde{D}(x), \tag{5.11}$$

where $\tilde{E}(x)$ is the mass of marked sand that leaves a unit surface in the unit time to enter in the saltation flux and $\tilde{D}(x)$ is, conversely, the mass of marked sand that leaves the saltation flux and is deposited on the sand surface. In the next section we will provide some possible constitutive relationship for these rates.

5.2.1 Entrainment-deposition formulation

Let us come back to the total mass balance equation (5.1), which does not distinguish between marked and unmarked sand. It is however possible to replace the divergence of the sand flux with the balance between the total entrainment and deposition rates (respectively $E = E(x,t)$ and $D = D(x,t)$),

$$\frac{\partial q}{\partial x} = E - D,$$

so that the mass balance equation (5.1) will take the form:

$$\rho_{dune} \frac{\partial h}{\partial t} = D - E.$$

Because the time scale of transport dynamics is well separated from that of the evolution of the sand surface, it is possible to adopt a quasi-static formulation and assume that E and D adapt instantaneously to the changes of $h(x,t)$. To determine the relation linking the deposition to the entrainment we further assume that Parker *et al.* (2000); Ganti *et al.* (2010):

1. once entrained from the sand surface, a sand grain performs a step (eventually rebounding) of length r before depositing again on the surface;

2. the step length is probabilistic, with probability density function (p.d.f.) $s(r)$, with $r \in (0, +\infty)$.

With these hypotheses we may write:

$$D(x) = \int_{-\infty}^{x} E(y)s(x - y)\,\mathrm{d}y = \int_{0}^{+\infty} E(x - y)s(y)\,\mathrm{d}y. \qquad (5.12)$$

Now, the problem is switched to the characterization of the entrainment rate and the p.d.f. for step length. We should first point out that, to the best of our knowledge, this entrainment-deposition formulation has not jet been proposed in the aeolian literature; consequently, the problem of the characterization of the entrainment rate and the p.d.f. of step length have not been jet investigated, either from the theoretical, or from the experimental point of view.

Here we limit ourselves to propose an entrainment-deposition formulation that is consistent with the minimal model for sand dune evolution exposed in Sect.5.1.

We first recall a useful relation that links the entrainment rate and the sand flux:

Proposition 5.2.1 *Let $\lambda = \int_{0}^{+\infty} rs(r)\,\mathrm{d}r < \infty$ be the mean step length. We suppose that $q(0) = 0$ and consider a constant entrainment rate on the positive axis. Then, the saturated entrainment rate E_{sat} that leads to a saturated flux q_{sat} is*

$$E_{sat} = \frac{q_{sat}}{\lambda}$$

Proof 5.2.1 *We can define $q_{sat} = \lim_{x \to +\infty} q(x)$. Hence we can write*

$$
\begin{aligned}
q(x) &= \int_{0}^{x} \frac{\partial q}{\partial y}\,\mathrm{d}y = \int_{0}^{x} \left(E(y) - D(y) \right)\,\mathrm{d}y = \\
&= \int_{0}^{x} \left(E(y) - \int_{0}^{y} E(y - z)s(z)\,\mathrm{d}z \right)\,\mathrm{d}y = \\
&= E_{sat} \int_{0}^{x} \left(1 - \int_{0}^{y} s(z)\,\mathrm{d}z \right)\,\mathrm{d}y = \\
&= E_{sat} \left[\left(\int_{x}^{+\infty} s(z)\,\mathrm{d}z \right) x + \int_{0}^{x} s(y)y\,\mathrm{d}y \right],
\end{aligned}
$$

and when $x \to +\infty$ the first term vanishes and the second one is equal to the mean step length λ.

We now use this relation to propose a constitutive model for the entrainment rate E and for the p.d.f. for step length $s(r)$ consistent with the constitutive relations of the sand flux formulation (5.4)-(5.5).

Proposition 5.2.2 *If we suppose that:*

1. *the entrainment rate is always equal to its saturated value:*

$$E(x) = \frac{q_{sat}(x)}{\lambda}$$

2. *the probability density function for the step length is exponential:*

$$s(r) = \frac{1}{\lambda} e^{-\frac{r}{\lambda}}$$

then the entrainment-deposition formulation is equivalent to the linear charge equation for the sand flux (5.5) with $L_{sat} = \lambda$.

Proof 5.2.2 *It suffices to note that the analytical solution of the charge equation (5.5), for example with the boundary condition $q(-\infty) = 0$, is*

$$q(x) = \int_{-\infty}^{x} q_{sat}(y) \frac{1}{L_{sat}} e^{-\frac{x-y}{L_{sat}}} \, \mathrm{d}y.$$

Thus the convolution with an exponential is naturally embedded in the analytical solution of the linear charge equation. The equivalence between the two formulation is therefore assessed by recognizing that, using the given hypothesis,

$$\frac{\partial q}{\partial x} = E(x) - D(x) = \frac{q_{sat}(x)}{\lambda} - \int_{-\infty}^{x} \frac{q_{sat}(y)}{\lambda} \frac{1}{\lambda} e^{-\frac{x-y}{\lambda}} \, \mathrm{d}y$$
$$= \frac{q_{sat}(x) - q(x)}{\lambda}.$$

The proposed formulation reproduces the effect of saturation of the sand flux thanks to the space lag existing between the phenomena of erosion and deposition, predicting a saturation length equal to the mean step length for sand grains. In Section 2.2 we reported that in the aeolian literature the saturation length is often assumed equal to $L_{sat} = 1\,\mathrm{m}$. This value seems to be compatible with the mean step length of a sand grain (remember that the step may includes several rebounds), hence this value will be assumed as effective parameter in our model.

5.2.2 Application to the marked sand dispersion problem

We can now go back to the problem of marked sand dispersion. In equation (5.11) we decided to substitute the divergence of the sand flux of marked sediment with the imbalance between entrainment $\tilde{E}$ and deposition rates $\tilde{D}$ of marked sand. Once the total entrainment rate is known, the active layer hypothesis leads naturally to the following expressions for $\tilde{E}$ and $\tilde{D}$:

$$\tilde{E}(x) = f_a(x)E(x), \qquad \tilde{D}(x) = \int_{-\infty}^{x} f_a(y)E(y)s(x-y) \, \mathrm{d}y.$$

In the entrainment-deposition framework, Eq.(5.10) is conveniently rewritten in the form:

$$\rho_{dune}L_a\frac{\partial f_a}{\partial t} = \tilde{D} - \tilde{E} - f_I(D - E),$$

where the left hand side represents the temporal variation of mass of marked sand in the active layer, which is due on the one hand to the imbalance between superficial entrainment and deposition rates of marked sand $(\tilde{D} - \tilde{E})$ and on the other hand to the amount of mass of marked sand which leaves (enters) the active layer at the interface with the substrate if net deposition (erosion) locally occurs. In addition, the evolution of the substrate concentration is governed by equation (3.3), which we conveniently rewrite in equivalent form here below. The complete system of equations which compose the model of marked sand dispersion during sand surface evolution finally reads:

$$\begin{cases} \dfrac{u_*^2(x)}{U_*^2} = \dfrac{\tau(x)}{\tau_0} = 1 + A\displaystyle\int \dfrac{1}{\pi\chi}\partial_x h(x-\chi)d\chi + B\partial_x h(x) \\[3mm] \begin{cases} E(x) = C_B\dfrac{\rho_{air}}{g}\dfrac{u_*^3(x)}{\lambda}, \qquad D(x) = \displaystyle\int_{-\infty}^{x} E(y)s(x-y)dy \\[3mm] \rho_{dune}\dfrac{\partial h}{\partial t} = D - E \qquad \text{s.t.} \quad |\partial_x h| < \tan\gamma, \\[3mm] \tilde{E}(x) = E(x)f_a(x), \qquad \tilde{D}(x) = \displaystyle\int_{-\infty}^{x} E(y)f_a(y)s(x-y)dy \\[3mm] \rho_{dune}L_a\dfrac{\partial f_a}{\partial t} = \tilde{D} - \tilde{E} - f_I(D - E) \end{cases} \\[3mm] f_b(x, h(x,\bar{t}) - L_a) = f_a(x,\bar{t}) \quad \text{if} \quad \partial_t h > 0. \end{cases} \qquad (5.13)$$

In the zone characterized by net deposition of sediments, the substrate incorporates sediments from the active layer, so that we need a storage technique for the marked sand concentration in the sedimentary column during evolution. This technique has been discussed in Sect.4.3, see Fig.4.12.

In Sect.4.1.2 we also provided an entrainment-deposition model for sand avalanches. Its application in the evolutionary model of sand dune with marked sand has been discussed in Sect.4.3.1.

5.2.3 Numerical simulations

In this section we detail the discretization techniques that we adopted for the numerical resolution of the entrainment-deposition formulation for the evolution of sand dunes with marked sand. At the same time, we illustrate some numerical simulations, aiming at showing the potential fields of application of our research.

5. A SIMPLIFIED MODEL FOR THE EVOLUTION OF TWO DIMENSIONAL DUNES

The domain $x \in (0, L)$ is subdivided in N_x intervals of equal size $\Delta x = L/N_x$. The midpoints $x_i = (i - 0.5)\Delta x$, $i = 1, ..., N_x$ are the point where the variables are approximated using the standard notation $f_i \simeq f(x_i)$. We consider also a subdivision of the vertical domain $z \in (H_{\min}, H_{\max})$ in N_z intervals of equal size Δz. The midpoints $z_i = H_{\min} + (i - 0.5)\Delta z$, $i = 1, ..., N_z$ are the discretization points of the vertical domain. The whole domain $[0, L] \times [H_{\min}, H_{\max}]$ is therefore discretized in $N_x \times N_z$ rectangular cells where (x_i, z_j) are the coordinates of the center points. The substrate concentration is constant in each cell and its values are stored in a matrix $\mathbf{F}_b$ such that $[\mathbf{F}_b]_{ij} \simeq f_b(x_i, z_j)$. The time interval $t \in [0, T_{\max}]$ is subdivided in N_t subintervals of equal duration Δt, and $t^n = n\Delta t$, $n = 0, ..., N_t$ are the discrete instants where the variables are approximated using the standard superscript notation $f_j^n \simeq f(x_j, t^n)$. In the following, the compact notation f^n (without subscripts) indicates the set of discrete values f_j^n, $j = 1, \ldots, N_x$ at time t^n.

The exponential density function for jump distance $s(r)$ is approximated on the grid cells through:

$$S_0 = \int_0^{\Delta x/2} s(r)\,\mathrm{d}r, \quad S_i = \int_{(i-1/2)\Delta x}^{(i+1/2)\Delta x} s(r)\,\mathrm{d}r, \quad i = 1, \ldots, M - 1,$$

$$S_M = \int_{(M-1/2)\Delta x}^{+\infty} s(r)\,\mathrm{d}r,$$

where the discretized p.d.f. S has $M + 1$ entries such that $\sum_{i=0}^{M} S_i = 1$.

The numerical algorithm for the simulation of sand dunes evolution with marked sand is:

- Given the initial profile h^0, the initial active layer concentration f_a^0 and the substrate concentration $\mathbf{F}_b^0$, for $n = 0, 1..., N_t - 1$, being h^n, f_a^n and $\mathbf{F}_b^n$ known:

  1. calculate the wind shear stress τ^n and hence the entrainment rate E^n and $\tilde{E}^n = E^n f_a^n$;

  2. calculate the deposition rates D^n and $\tilde{D}^n$, where their components are computed with the discrete convolutions:

  $$D_i^n = \sum_{j=0}^{M} S_j E_{i-j}^n \qquad \tilde{D}_i^n = \sum_{j=0}^{M} S_j \tilde{E}_{i-j}^n$$

  3. update the sand surface, the active layer concentration:

  $$h^{n+1/2} = h^n + \frac{\Delta t}{\rho_{sand}}\left(D^n - E^n\right),$$

  $$f_a^{n+1/2} = f_a^n + \frac{\Delta t}{\rho_{sand}L_a}\left[\tilde{D}^n - \tilde{E}^n - f_I^n\left(D^n - E^n\right)\right],$$

  and, in the nodes where $D^n > E^n$, the substrate concentration $\mathbf{F}_b^{n+1/2}$ with scheme of Fig.4.12

4. set $u^0 = h^{n+1/2}$ and $f^0 = f_a^{n+1/2}$, iterate the avalanche model with marked sand of Sect.4.3.1:

   for $k = 0, 1, ...$ compute

$$u^{k+1} = u^k + \Delta t_{av} \left(\mathcal{D}^k - \mathcal{E}^k \right)$$

$$f^{k+1} = f^k + \frac{\Delta t_{av}}{L_a} \left[\tilde{\mathcal{D}}^k - \tilde{\mathcal{E}}^k - f_I^k (\mathcal{D}^k - \mathcal{E}^k) \right]$$

   updating also $\mathbf{F}_b^{k+1}$ where $\mathcal{D}^k > \mathcal{E}^k$, until convergence is reached.

5. set $h^{n+1} = u^{k+1}$, $f_a^{n+1} = f^{k+1}$ and $\mathbf{F}_b^{n+1} = \mathbf{F}_b^{k+1}$

In Fig.5.6 the typical profile of entrainment and deposition fluxes on a dune are shown. Starting from the foot of the dune, the entrainment rate grows with growing wind shear stress. Its maximum is located where the shear stress is maximum. The deposition rate follows the entrainment profile with a space lag due to the p.d.f. for jump length. In the recirculation zone, the entrainment rate is null and only deposition occurs.
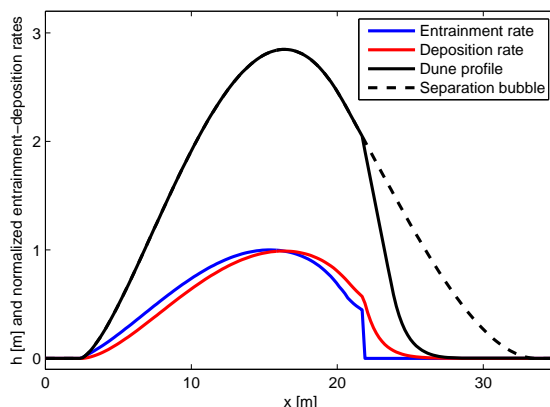

Figure 5.6: Entrainment and deposition profiles on a sand dune - We note that the deposition rate follows the profile of the entrainment rate with a shift given by the p.d.f. for step length. The entrainment rate is null in the recirculation zone, where only deposition occurs.

Dune collision We now propose an application of the model of dune evolution coupled with marked sand dispersion. We consider the domain $[0, 200] \times [-0.5, 5.5]$ discretized with 500×120 cells of $\Delta x = 40$ cm, $\Delta z = 5$ cm. We consider an input wind intensity $u_* = 0.5$ m/s on an initial surface formed by two symmetric bumps of sand, the first 20 m wide and 2 m high, the second 40 m wide and 4 m high. The volume ratio between the two initial bumps is chosen such that the two dunes collide forming a single dune (Diniega *et al.*, 2010). It is interesting to study how the sand of the first

dune redistributes during the collision. For this purpose, we assume that initially the smallest dune is formed by marked sand.

In this model the parameter L_a limits the choice of the Δt to use in the algorithm, for stability reasons. Since the time scales required to observe dune movement are of the order of $10^1 - 10^3$ days, we have taken a (large) value for L_a to limit the overall computational cost. In particular, we have chosen $L_a = 25$ mm (100 sand grain diameter) and $\Delta t = 6$ min, which is a quite reasonable value for the time scales considered. With these choices of the parameters, the evolution of the model is represented in Figure 5.7, where we can note the evolution of the marked sand concentration during the collision. At the end, a big dune with marked sand concentration $\simeq 0.2$ (that is the initial volume ratio of marked sand in the simulation) is formed.
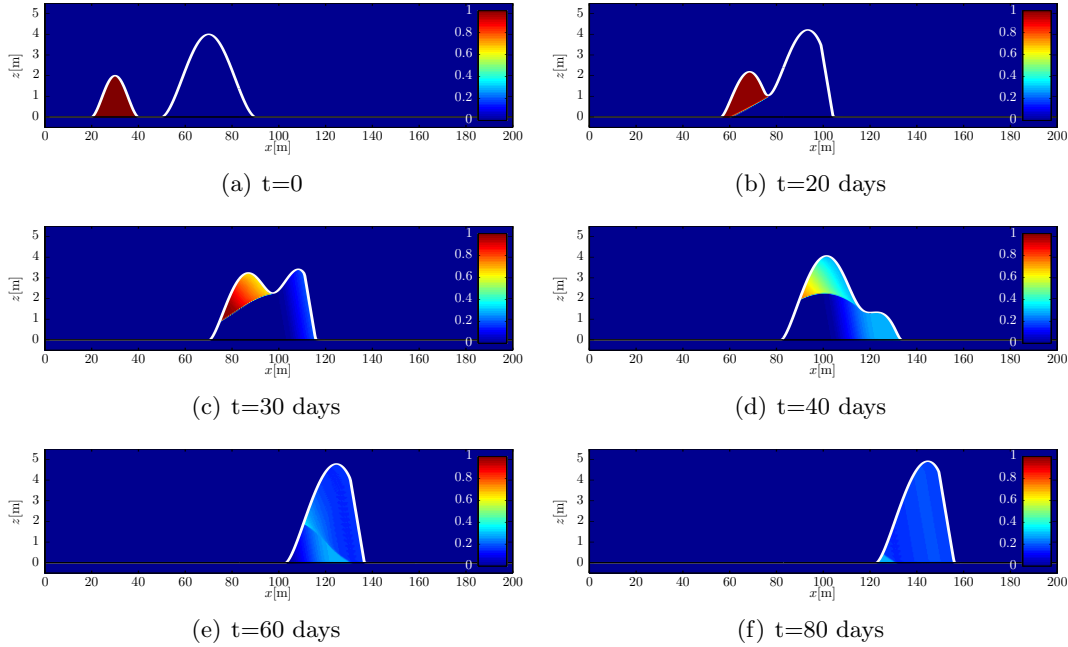

(a) t=0

(b) t=20 days

(c) t=30 days

(d) t=40 days

(e) t=60 days

(f) t=80 days

Figure 5.7: Dune collision between small and big dune - As initial condition, the first smaller dune is made of marked sand; as it's faster than the bigger, the two dune collides. At different time step, we see the marked sand concentration during dune collision.

By imposing a bigger left bump in the initial profile, *i.e.* 30 m wide and 3.5 m high, the resulting collision is completely different. The two dune interacts, as the downwind dune enters in the recirculation zone generated by the first one, but they do not coalesce. The left dune becomes smaller and, at a certain time, escapes from the interaction of the left dune. At final time, the left dune becomes 5 m high and the right dune 2 m high.
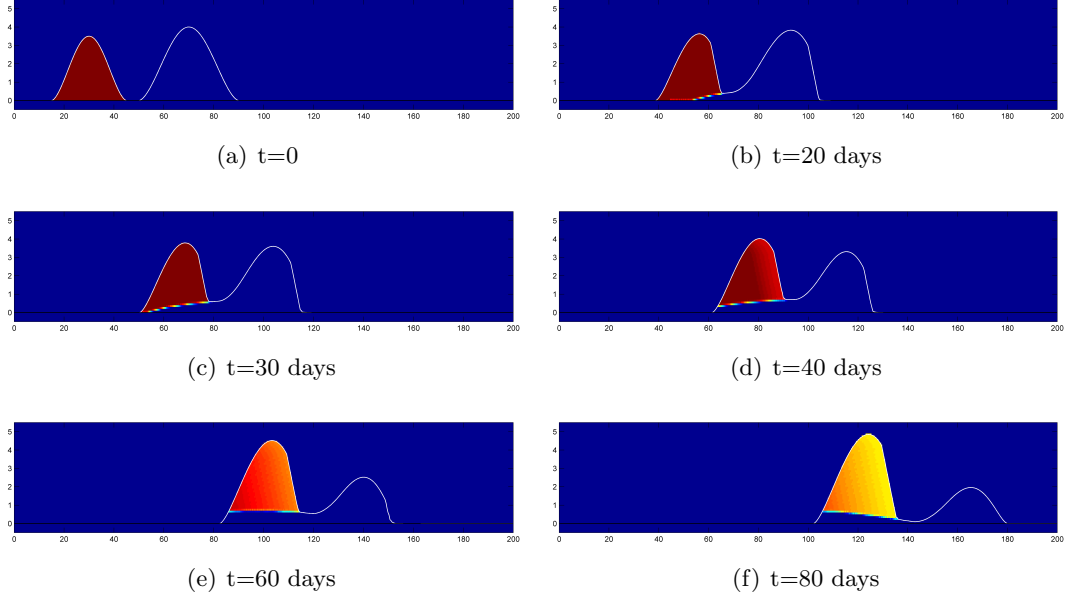
(a) t=0

(b) t=20 days

(c) t=30 days

(d) t=40 days

(e) t=60 days

(f) t=80 days

Figure 5.8: Dune collision between medium and big dune - The medium dune is made of marked sand. In this case the collision does not generate a single dune.

5.2.4 Coupling with a microseepage model

The description given so far allows us to include a model of generation of marked sand by hydrocarbon microseepage. If we assume that:

- in a given region of the horizontal domain exists a deep source of hydrocarbon microseepage;

- hydrocarbons generated from the deep source seep in vertical direction and with constant velocity along the whole sedimentary column;

- hydrocarbons which enter in contact with clean sand generate marked sand in a manner proportional to their concentration;

it is possible to model the generation of marked sand by the following system of differential equations:

$$
\begin{cases}
\dfrac{\partial f_g}{\partial t} + v\dfrac{\partial f_g}{\partial z} = -\gamma(\bar{f}_b - f_b)f_g \\[2ex]
\dfrac{\partial f_b}{\partial t} = \gamma(\bar{f}_b - f_b)f_g \\[2ex]
f_g(x, z, t) = g(x) \qquad \text{at} \quad z = z_{bottom}
\end{cases}
\tag{5.14}
$$

where $f_g = f_g(x, z, t)$ is the volume concentration of seeping hydrocarbons in the point (x, z) of the sedimentary column, $f_b = f_b(x, z, t)$ is the volume concentration of marked

5. A SIMPLIFIED MODEL FOR THE EVOLUTION OF TWO DIMENSIONAL DUNES

sand in the substrate, $\bar{f}_b$ is a parameter indicating the saturated value for f_b, v is the vertical speed of seeping gas and γ is a coefficient (dimensionally is a frequency) which regulates the generation of marked sand by the contact of seeping gas flow.

In the left side of the first equation we recognize the mathematical structure of the advection equation for the concentration f_g with constant vertical speed v. At the right hand side of the first equation there is an absorption term with absorption coefficient proportional to the difference $\bar{f}_b - f_b$, *i.e.* the absorbing reaction is more intense if the local concentration of marked sand is far from its saturation value.

For conservation of the total mass of gas, we find the same absorption term with the opposite sign in the right hand side of the second equation. This equation states that the temporal variation of marked sand concentration f_b is proportional to the local concentration of gas in microseepage f_g and to the gap from the saturation value $\bar{f}_b - f_b$.

This system is equipped with a boundary condition for the gas concentration at the bottom of the domain; typically the boundary value $g(x)$ is written in the form:

$$g(x) = \begin{cases} \bar{f}_g & \text{if } x \in (a, b) \\ 0 & \text{otherwise,} \end{cases}$$

where $\bar{f}_g$ is the maximum volumetric concentration of the seeping hydrocarbons which may be present in the considered sand and the interval $[a, b]$ defines the position of the source of hydrocarbon (*i.e.* the position of the deep reservoir).

The system (5.14) is coupled to the system (5.13) which describes the model of marked sand dispersion during sand surface evolution. The numerical approximation of (5.14) is performed by discretizing the time derivative with the explicit Euler method and the vertical derivative with a first order upwind (with respect to v) finite difference. The two system are hence solved at the same discrete instants $t^n = n\Delta t$.

Numerical simulation of a simplified case The geometry of the test case is reported in Fig.5.9. In a domain $2\,\mathrm{Km}$ long we set an initially flat sand basin extended for $1\,\mathrm{Km}$ and deep at maximum $10\,\mathrm{m}$. The source of hydrocarbon microseepage is placed at the bottom of the domain in the interval $x \in (200, 300)$ m. The vertical domain is $30\,\mathrm{m}$ high. The domain is discretized in cells of dimensions $\Delta x = 1\,\mathrm{m}$ and $\Delta z = 0.15\,\mathrm{m}$. We consider a constant undisturbed wind characterized by a shear velocity $u_* = 0.5\,\mathrm{m/s}$. The active layer depth is $L_a = 25\,\mathrm{mm}$. The vertical speed of seeping gas is $v = 50\,\mathrm{mm/h}$ and the absorption coefficient $\gamma = 1 \times 10^{-6}\,\mathrm{sec}^{-1}$. The time step is $\Delta t = 15\,\mathrm{min}$.

After $T = 50\,\mathrm{days}$, see Fig.5.10, the hydrocarbon microseepage has generated marked sand in the whole sedimentary column, reaching the free surface: the concentration of marked sand in the active layer increases. The free surface in the downwind portion of the domain with respect to hydrocarbon source has not developed sand dunes yet. Hence the marked sand grains which enters in the active layer can reach the right boundary of the domain without being captured in dune slipfaces. This is clearly seen
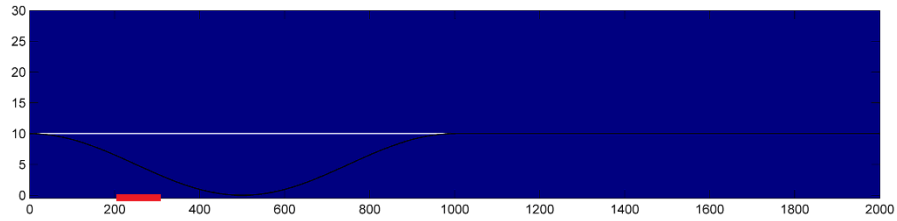
Figure 5.9: Initial condition for the microseepage test case - The domain is 2 Km long, with an erodible zone deep at maximum 10 m in the first Km, here represented in black. In white the sand surface, initially flat. The red segment denotes the position of the source of hydrocarbons.

at $T = 100$ days, where the whole domain has a concentration of marked sand in the active layer really high ($\approx 80\%$).

At $T = 150$ days we have dunes with slipface in downwind position with respect to the hydrocarbon source, hence the superficial flux of marked sediments towards the right boundary is interrupted. As a consequence, the active layer concentration in the downwind portion of the domain diminishes.
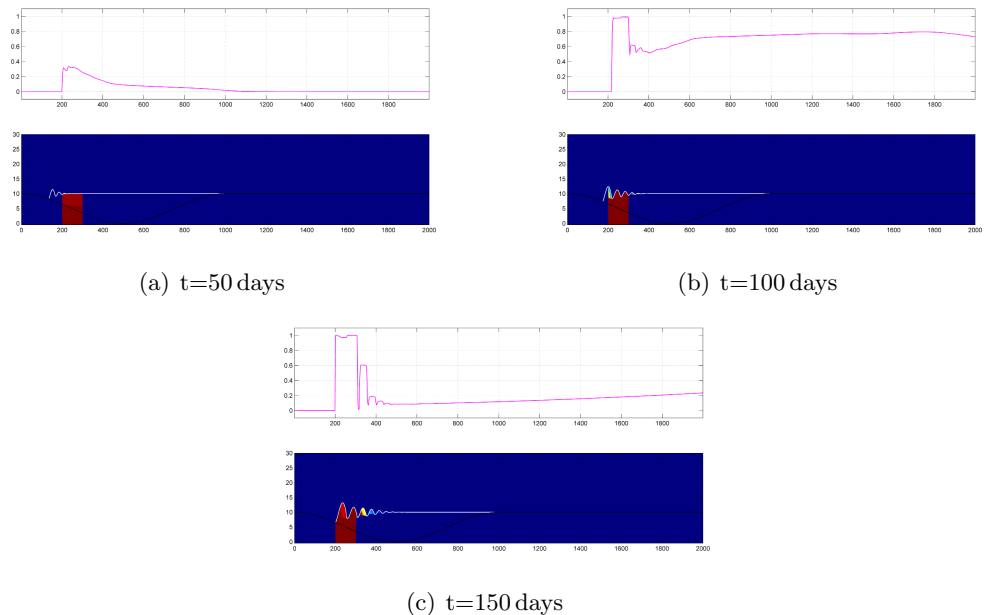

(a) t=50 days

(b) t=100 days

(c) t=150 days

Figure 5.10: Superficial and substrate concentration - For intermediate instants the dunes are not yet developed, hence the marked sediments can diffuse in the whole domain.

Finally, it is interesting to see what happens in long times: in Fig.5.11 we can observe

the simulation at $T = 450$ days, when all the sand has abandoned the zone over the
source of microseepage. We notice that each dune that is formed advances transporting
a well defined concentration of marked sand. Looking at the active layer concentration
profile, we notice that the superficial footprint of hydrocarbon microseepage shows an
effective dispersion in direction of the wind.

For $T = 1300$ days, the dunes are leaving the zone that was initially covered with sand.
As seen in the previous case, each dune transports a defined concentration of marked
sand. The last biggest dune has a concentration of marked sand $\approx 30\%$.

To conclude, in these conditions of simulation, in almost 4 years of constant unidirec-
tional wind, the superficial footprint of a microseepage source (*i.e.* the oil/gas reservoir)
wide 100 m moved ≈ 350 m in wind direction, loosing more than 70% of its initial in-
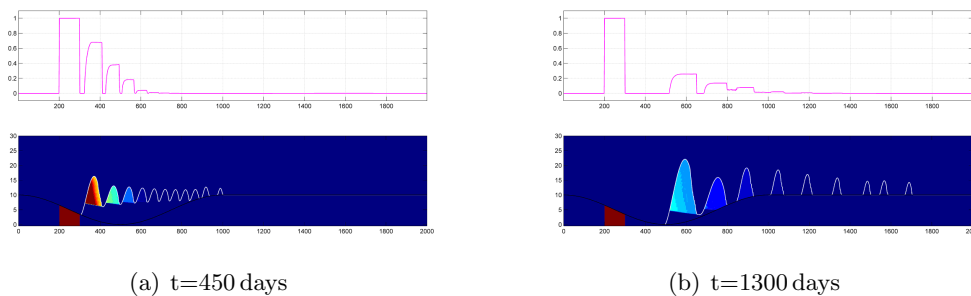tensity.

(a) t=450 days   (b) t=1300 days

Figure 5.11: Superficial and substrate concentration - For long time, the dunes are
well developed, and each dune transports a well defined concentration of marked sand.

6

Discussion and conclusions

In this work we developed an original mathematical model for the evolution of a mixture of sands in aeolian dunes. The mixture considered here is made of marked and clean sand, as this work is motivated by the industrial problem of dispersion of sand anomalies induced by hydrocarbon microseepage.

The original model formulated in Chap.3, based on the well established continuum saltation flux model reviewed in Chap.2, is valid in the general three dimensional case; however, the numerical approximation and the simulation results shown in Chap.4 are limited to the two dimensional case. Concerning the evolution of two dimensional dunes, the simplified entrainment-deposition model developed in Chap.5 constitute however a great simplification with tremendously higher computational efficiency and with limited drawbacks. However, the direct extension of this entrainment-deposition formulation to the three dimensional case is not feasible, since we would have to solve the convolution integral (5.12) for deposition calculation along the unknown trajectory of the three dimensional sand flux.

Hence, the three dimensional model based on the complete formulation detailed in Chap.3 have been studied in the last months of my Ph.D. studentship but, up to the date of manuscript writing, the numerical methods developed and the simulation results obtained are not completely satisfactory, hence they have not been included in this Ph.D. thesis.

Some preliminary results, such as the profile of the main physical quantities on a small stationary three dimensional dune, are however reported in Fig.6.1. Moreover, the improvement of the numerical model for three dimensional sand dune evolution will be topic of further investigations.

Disjointly from the sand dune evolution model, the original entrainment-deposition formulation for sand avalanches produces completely satisfactory results, as we have compared them with the ones obtained with the augmented Lagrangian formulation of Caboussat & Glowinski (2009). Once again, the advantage of our entrainment-deposition formulation relies in its limited computational costs and in the possible application to the problem of sand avalanches with marked sand, see Sect.4.3.1.

6. DISCUSSION AND CONCLUSIONS

One of the most interesting application of our model is the study of dunes collision. In fact, we can assume that one of the colliding dune is formed by marked sand, and follow the evolution of its concentration in the sedimentary column during dune collision. Naturally, the most interesting features of dune collision only appear in three dimensions (Durán *et al.*, 2005), but the results obtained in the two dimensional case stimulate us to refine the model and widen the possible fields of application.

The application of our model to the dispersion of sand marked by hydrocarbon microseepage anomalies, that is the industrial problem that motivated this Ph.D. work, demonstrates that the superficial footprint of the deep reservoir can effectively be displaced by wind action. However, the proposed model of generation of marked sand is very simple and need to be improved in the future, *e.g.* with a more realistic model for the motion of hydrocarbon in the sedimentary column and a detailed description of the mechanisms of absorption and retention of hydrocarbons at the sand grain level. Moreover, many of the new added parameters of the proposed model are subject to strong uncertainty, and need to be validated by theoretical considerations and experimental evidences.

Looking beyond, the proposed formulation can simulate the direct problem, *i.e.* we can obtain the superficial concentration of marked sand generated by a known microseepage source. For oil exploration, the more interesting problem is the inverse one, that is the determination of the position of the source of hydrocarbon microseepage from a given superficial map of marked sand. Since the mathematical modelling of the inverse problem necessitates a good model for the direct one, our work constitutes a fundamental step in that direction.
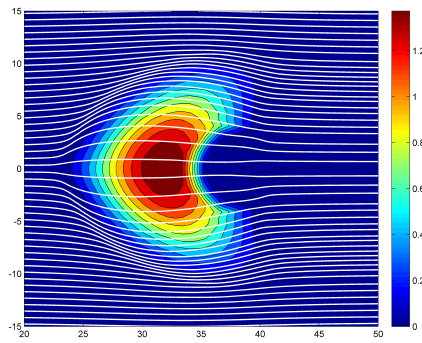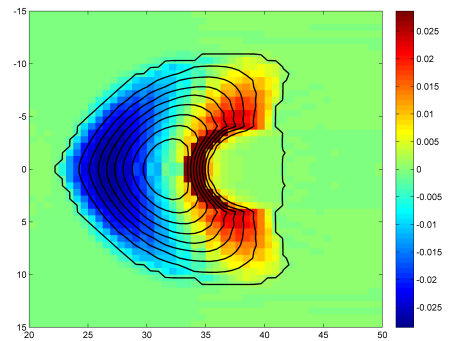
(a) Shear stress: $\boldsymbol{\tau}(x,y)$ streamlines
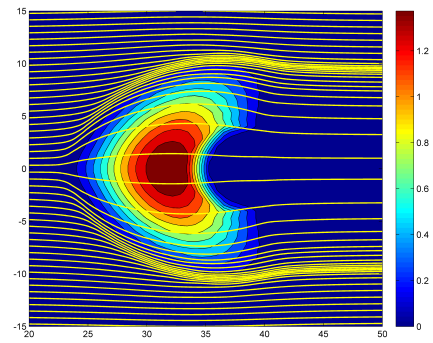
(b) Sand flux velocity: $\mathbf{u}(x,y)$ streamlines
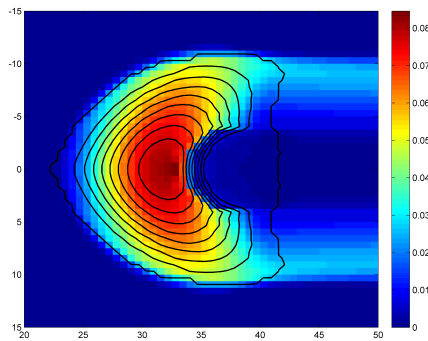
(c) Sand flux density: $\rho(x,y)$

(d) Deposition-Erosion: $-\Gamma(x,y)$

Figure 6.1: Preliminary three dimensional results - Main relevant physical quantities on a small three dimensional dune.

References

ALMEIDA, M.P., PARTELI, E.J.R., ANDRADE, J.S. & HERRMANN, H.J. (2008). Giant saltation on mars. *Proceedings of the National Academy of Sciences*, **105**, 6222–6226. 57

ANDERSON, R. (1987). A theoretical model for aeolian impact ripples. *Sedimentology*, **34**, 943–956. 17

ANDERSON, R. (1991). Wind modification and bed response during saltation of sand in air. *Acta Mechanica*, **Suppl.1**, 21–51. 25, 30

ANDERSON, R.S. & HAFF, P.K. (1988). Simulation of eolian saltation. *Science*, **241**, 820–823. 14, 30

ANDREOTTI, B. (2004). A two-species model of aeolian sand transport. *Journal of Fluid Mechanics*, **510**, 47–70. 32

ANDREOTTI, B. & CLAUDIN, P. (2007). Comment on "Minimal size of a barchan dune". *Physical Review E*, **76**, 063301. 102

ANDREOTTI, B., CLAUDIN, P. & DOUADY, S. (2002a). Selection of dune shapes and velocities part 1: Dynamics of sand, wind and barchans. *The European Physical Journal B*, **28**, 321–339. 99, 100

ANDREOTTI, B., CLAUDIN, P. & DOUADY, S. (2002b). Selection of dune shapes and velocities part 2: A two dimensional modelling. *The European Physical Journal B*, **28**, 341–352. 18, 99, 100, 101

ANDREOTTI, B., CLAUDIN, P. & POULIQUEN, O. (2010). Measurements of the aeolian sand transport saturation length. *Geomorphology*, **123**, 343 – 348. 18, 100

ARMANINI, A. (1995). Non-uniform sediment transport: Dynamics of the active layer. *Journal of Hydraulic Research*, **33**, 611–622. 20, 54

ARONSSON, G., EVANS, L. & WU, Y. (1996). Fast/slow diffusion and growing sand-piles. *Journal of Differential Equations*, **131**, 304–335. 19

BAGNOLD, R. (1936). The movement of desert sand. *Proceedings of the Royal Society of London. Series A, Mathematical and Physical Sciences*, **157**, 594–620. 14

REFERENCES

BAGNOLD, R. (1941). *The physics of blown sand and desert dunes*. Chapman and Hall, London. 12, 14, 15, 21, 22, 30, 31, 32, 99

BARNDORFF-NIELSEN, O. & CHRISTIANSEN, C. (1988). Erosion, deposition and size distributions of sand. *Proceedings of the Royal Society of London. A. Mathematical and Physical Sciences*, **417**, 335. 20

BERG, N. (1983). Field evaluation of some sand transport models. *Earth Surface Processes and Landforms*, **8**, 101–114. 20

BISHOP, S., MOMIJI, H., CARRETERO-GONZÁLEZ, R. & WARREN, A. (2002). Modelling desert dune fields based on discrete dynamics. *Discrete Dynamics in Nature and Society*, **7**, 7–17. 19

BLOM, A. & PARKER, G. (2004). Vertical sorting and the morphodynamics of bed form-dominated rivers: A modeling framework. *Journal of Geophysical Research*, **109**, F02007. 20

BRADLEY, D., TUCKER, G. & BENSON, D. (2010). Fractional dispersion in a sand bed river. *Journal of Geophysical Research*, **115**, F00A09. 20

BUTTERFIELD, G.R. (1993). Sand transport response to fluctuating wind velocity. In N.J. Clifford, J.R. French & J. Hardisty, eds., *Turbulence: Perspectives on Flow and Sediment Transport*, chap. 13, 305–335, John Wiley & Sons Ltd. 30

CABOUSSAT, A. & GLOWINSKI, R. (2009). A numerical method for a non-smooth advection-diffusion problem arising in sand mechanics. *Communications on Pure and Applied Analysis*, **8**, 161–178. 19, 62, 65, 66, 67, 70, 115

CABRERA, L. & ALONSO, I. (2010). Correlation of aeolian sediment transport measured by sand traps and fluorescent tracers. *Journal of Marine Systems*, **80**, 235–242. 20

CHEPIL, W. (1945). Dynamics of wind erosion: I. nature of movement of soil by wind. *Soil Science*, **60**, 305. 14

CREYSSELS, M., DUPONT, P., OULD EL MOCTAR, A., VALANCE, A., CANTAT, I., JENKINS, J., PASINI, J. & RASMUSSEN, K. (2009). Saltating particles in a turbulent boundary layer: experiment and theory. *Journal of Fluid Mechanics*, **625**, 47–74. 34

DINIEGA, S., GLASNER, K. & BYRNE, S. (2010). Long-time evolution of models of aeolian sand dune fields: Influence of dune formation and collision. *Geomorphology*, **121**, 55–68. 109

DURÁN, O. (2007). *Vegetated dunes and barchan dune fields*. Ph.D. thesis, Universität Stuttgart, Stuttgart, Germany. 30, 33, 46, 48

DURÁN, O. & HERRMANN, H. (2006a). Modelling of saturated sand flux. *Journal of Statistical Mechanics: Theory and Experiment*, **2006**, P07011. 26, 27, 30, 32

DURÁN, O. & HERRMANN, H.J. (2006b). Vegetation against dune mobility. *Physical Review Letters*, **97**, 188001. 41

DURÁN, O., SCHWÄMMLE, V. & HERRMANN, H. (2005). Breeding and solitary wave behavior of dunes. *Physical Review E*, **72**, 021308. 41, 116

DURÁN, O., PARTELI, E.J. & HERRMANN, H.J. (2010). A continuous model for sand dunes: Review, new developments and application to barchan dunes and barchan dune fields. *Earth Surface Processes and Landforms*, **35**, 1591–1600. 17, 19

DURÁN, O., CLAUDIN, P. & ANDREOTTI, B. (2011). On aeolian transport: Grain-scale interactions, dynamical mechanisms and scaling laws. *Aeolian Research*, **3**, 243–270. 34, 41, 43

EASTWOOD, E., NIELD, J., BAAS, A. & KOCURECK, G. (2011). Modelling controls on aeolian dune-field pattern evolution. *Sedimentology*, **58**, 1391–1406. 19

FALCONE, M. & FINZI VITA, S. (2007). A finite-difference approximation of a two-layer system for growing sandpiles. *SIAM Journal on Scientific Computing*, **28**, 1120. 74

FORTIN, M. & GLOWINSKI, R. (1983). *Augmented Lagrangian methods: Applications to the numerical solution of boundary-value problems*. North-Holland, Amsterdam. 68

FRYBERGER, S., AL-SARI, A., CLISHAM, T., RIZVI, S. & AL-HINAI, K. (1984). Wind sedimentation in the Jafurah sand sea, Saudi Arabia. *Sedimentology*, **31**, 413–431. 18

GANTI, V., MEERSCHAERT, M., FOUFOULA-GEORGIOU, E., VIPARELLI, E. & PARKER, G. (2010). Normal and anomalous diffusion of gravel tracer particles in rivers. *Journal of Geophysical Research*, **115**, F00A12. 20, 104

GLOWINSKI, R. (2008). *Numerical methods for nonlinear variational problems*. Springer Verlag. 62, 67, 68

GLOWINSKI, R. & LE TALLEC, P. (1989). *Augmented Lagrangian and operator-splitting methods in nonlinear mechanics*. SIAM, Philadelphia. 68

GORDON, M. & NEUMAN, C. (2009). A comparison of collisions of saltating grains with loose and consolidated silt surfaces. *Journal of Geophysical Research*, **114**, F04015. 19

HASSAN, M.A. & ERGENZINGER, P. (2005). Use of tracers in fluvial geomorphology. In G. Kondolf & H. Piégay, eds., *Tools in Fluvial Geomorphology*, chap. 14, 397–423, John Wiley & Sons, Ltd. 20

REFERENCES

HERRMANN, H., ANDRADE, J., JR., SCHATZ, V., SAUERMANN, G. & PARTELI, E. (2005). Calculation of the separation streamlines of barchans and transverse dunes. *Physica A: Statistical Mechanics and its Applications*, **357**, 44–49. 18

HERSEN, P. (2004). On the crescentic shape of barchan dunes. *The European Physical Journal B - Condensed Matter*, **37**, 507–514. 101

HOEY, T.B. & FERGUSON, R. (1994). Numerical simulation of downstream fining by selective transport in gravel bed rivers: model development and illustration. *Water Resources Research*, **30**, 2251–2260. 54

HUNT, J. & NALPANIS, P. (1985). Saltating and suspended particles over flat and sloping surfaces. I. Modelling concepts. In *Proceedings of the international workshop on the physics of blown sand*, vol. 8, 9–36. 13

HUNT, J., LEIBOVICH, S. & RICHARDS, K. (1988). Turbulent shear flows over low hills. *Quarterly Journal of the Royal Meteorological Society*, **114**, 1435–1470. 18, 44

INGLE, J. (1966). *The movement of beach sand: an analysis using fluorescent grains*, vol. 5 of *Developments in Sedimentology*. Elsevier. 20

IVERSEN, J. & RASMUSSEN, K. (1999). The effect of wind speed and bed slope on sand transport. *Sedimentology*, **46**, 723–731. 30, 32

JACKSON, P. & HUNT, J. (1975). Turbulent wind flow over a low hill. *Quarterly Journal of the Royal Meteorological Society*, **101**, 929–955. 18, 19, 44

JENSEN, J. & SØRENSEN, M. (1986). Estimation of some aeolian saltation transport parameters: a re-analysis of Williams' data. *Sedimentology*, **33**, 547–558. 14

JOLY, J. (1904). Formation of sand-ripples. In *The Scientific proceedings of the Royal Dublin Society*, vol. 10, 328–330. 14

JOUBERT, E., HARMS, T., MULLER, A., HIPONDOKA, M. & HENSCHEL, J. (2012). A CFD study of wind patterns over a desert dune and the effect on seed dispersion. *Environmental Fluid Mechanics*, **12**, 23–44. 18

KOCUREK, G. & EWING, R.C. (2005). Aeolian dune field self-organization - implications for the formation of simple versus complex dune-field patterns. *Geomorphology*, **72**, 94–105. 19

KROY, K., SAUERMANN, G. & HERRMANN, H.J. (2002). Minimal model for aeolian sand dunes. *Physical Review E*, **66**, 031302. 17, 18, 41, 44, 47, 98, 101

LETTAU, K. & LETTAU, H. (1978). Experimental and micrometeorological field studies of dune migration. In H.H. Lettau & K. Lettau, eds., *Exploring the world's driest climate*, Madison, Center for Climatic Research, University of Wisconsin. 31

LeVeque, R. (2002). *Finite volume methods for hyperbolic problems*, vol. 31. Cambridge University Press. 82, 83

Livingstone, I., Wiggs, G. & Weaver, C. (2007). Geomorphology of desert sand dunes: a review of recent progress. *Earth-Science Reviews*, **80**, 239–257. 18

Mason, P. & Sykes, R. (1979). Flow over an isolated hill of moderate slope. *Quarterly Journal of the Royal Meteorological Society*, **105**, 383–395. 44

McEwan, I. & Willetts, B. (1991). Numerical model of the saltation cloud. *Acta Mechanica*, **Suppl.1**, 53–66. 30

Momiji, H., Carretero-Gonzalez, R., Bishop, S. & Warren, A. (2000). Simulation of the effect of wind speedup in the formation of transverse dune fields. *Earth Surface Processes and Landforms*, **25**, 905–918. 19

Nalpanis, P. (1985). Saltating and suspended particles over flat and sloping surfaces. II. Experiments and numerical simulations. In *Proceedings of International Workshop on the physics of Blown Sand*, 37–66. 13

Narteau, C., Zhang, D., Rozier, O., Claudin, P. *et al.* (2009). Setting the length and time scales of a cellular automaton dune model from the analysis of superimposed bed forms. *Journal of Geophysical Research*, **114**, F03006. 19

Oberman, A. (2006). Convergent difference schemes for degenerate elliptic and parabolic equations: Hamilton-Jacobi equations and free boundary problems. *SIAM Journal on Numerical Analysis*, **44**, 879–895. 74

Ortiz, P. & Smolarkiewicz, P. (2006). Numerical simulation of sand dune evolution in severe winds. *International Journal for Numerical Methods in Fluids*, **50**, 1229–1246. 18

Ortiz, P. & Smolarkiewicz, P. (2009). Coupling the dynamics of boundary layers and evolutionary dunes. *Physical Review E*, **79**, 041307. 18

Owen, P. (1964). Saltation of uniform grains in air. *Journal of Fluid Mechanics*, **20**, 225–242. 14, 22, 24, 29, 30, 31, 32, 36

Owens, J. (1927). The movement of sand by wind. *Engineer*, **143**, 377. 14

Parker, G. (1991). Selective sorting and abrasion of river gravel. I. Theory. *Journal of Hydraulic Engineering*, **117**, 131–149. 20, 41, 54

Parker, G., Paola, C. & Leclair, S. (2000). Probabilistic Exner sediment continuity equation for mixtures with no active layer. *Journal of Hydraulic Engineering*, **126**, 818–826. 20, 41, 54, 104

REFERENCES

PARSONS, D., WALKER, I. & WIGGS, G. (2004). Numerical modelling of flow structures over idealized transverse aeolian dunes of varying geometry. *Geomorphology*, **59**, 149–164. 18

PARTELI, E. (2007). *Sand Dunes on Mars and on Earth*. Ph.D. thesis, Universität Stuttgart, Stuttgart, Germany. 30, 48

PARTELI, E., DURAN, O. & HERRMANN, H. (2007a). Minimal size of a barchan dune. *Physical Review E*, **75**, 011301. 102

PARTELI, E., DURÁN, O. & HERRMANN, H. (2007b). Reply to "Comment on "Minimal size of a barchan dune""". *Physical Review E*, **76**, 063302. 102

PARTELI, E., DURÁN, O., TSOAR, H., SCHWÄMMLE, V. & HERRMANN, H. (2009). Dune formation under bimodal winds. *Proceedings of the National Academy of Sciences*, **106**, 22085. 41, 46

PARTELI, E.J.R. & HERRMANN, H.J. (2007). Saltation transport on Mars. *Physical Review Letters*, **98**, 198001. 41

PELLETIER, J. (2009). Controls on the height and spacing of eolian ripples and transverse dunes: a numerical modeling investigation. *Geomorphology*, **105**, 322–333. 19

PISCHIUTTA, M., FORMAGGIA, L. & NOBILE, F. (2011). Mathematical modelling for the evolution of aeolian dunes formed by a mixture of sands: entrainment-deposition formulation. *Communications in Applied and Industrial Mathematics*, **2**. 97

PRIGOZHIN, L. (1993). A variational problem of bulk solids mechanics and free-surface segregation. *Chemical Engineering Science*, **48**, 3647–3656. 19

PRIGOZHIN, L. (1996). Variational model of sandpile growth. *European Journal of Applied Mathematics*, **7**, 225–236. 19

PRIGOZHIN, L. & ZALTZMAN, B. (2001). Two continuous models for the dynamics of sandpile surfaces. *Physical Review E*, **63**, 041505. 19

PYE, K. & TSOAR, H. (1990). *Aeolian Sand and Sand Dunes*. Springer. 13, 14, 15, 16, 30

RASMUSSEN, K., IVERSEN, J. & RAUTAHEMIO, P. (1996). Saltation and wind-flow interaction in a variable slope wind tunnel. *Geomorphology*, **17**, 19–28. 30

RIOUAL, F. (2002). *Etude de quelques aspects du transport éolien: processus de saltation et formation des rides*. Ph.D. thesis, Université de Rennes, Rennes, France. 58

SAUERMANN, G. (2001). *Modeling of Wind Blown Sand and Desert Dunes*. Ph.D. thesis, Universität Stuttgart, Stuttgart, Germany. 30, 48

SAUERMANN, G., KROY, K. & HERRMANN, H.J. (2001). Continuum saltation model for sand dunes. *Physical Review E*, **64**, 031305. 17, 18, 21, 23, 25, 27, 30, 36, 99

SAUERMANN, G., ANDRADE, J., MAIA, L., COSTA, U., ARAÚJO, A., HERRMANN, H. *et al.* (2003). Wind velocity and sand transport on a barchan dune. *Geomorphology*, **54**, 245–255. 17

SCHATZ, V. & HERRMANN, H. (2006). Flow separation in the lee side of transverse dunes: A numerical investigation. *Geomorphology*, **81**, 207–216. 18

SCHWÄMMLE, V. & HERRMANN, H. (2005). A model of barchan dunes including lateral shear stress. *The European Physical Journal E-Soft Matter*, **16**, 57–65. 41, 44

SCHWÄMMLE, V., HERRMANN, H. *et al.* (2003). Solitary wave behaviour of sand dunes. *Nature*, **426**, 619–620. 41

SETHIAN, J. (1999). Fast marching methods. *SIAM review*, **41**, 199–235. 74

SHU, C. (2009). High order weighted essentially non-oscillatory schemes for convection dominated problems. *SIAM review*, **51**, 82–126. 101

SØRENSEN, M. (1988). *Radioactive tracer studies of grain progress in aeolian sand transport: a statistical analysis*. Afdelingen for Teoretisk Statistik, Matematisk Institut, Aarhus Universitet. 20

SØRENSEN, M. (2004). On the rate of aeolian sand transport. *Geomorphology*, **59**, 53–62. 26, 30, 31, 32

STAM, J. (1997). On the modeling of two-dimensional aeolian dunes. *Sedimentology*, **44**, 127–141. 17, 18

SYKES, R. (1980). An asymptotic theory of incompressible turbulent boundarylayer flow over a small hump. *Journal of Fluid Mechanics*, **101**, 647–670. 44

TORO, E. (2009). *Riemann solvers and numerical methods for fluid dynamics: a practical introduction*. Springer Verlag. 82

TSOAR, H. & YAALON, D. (1983). Deflection of sand movement on a sinuous longitudinal (seif) dune: use of fluorescent dye as tracer. *Sedimentary Geology*, **36**, 25–39. 20

UNGAR, J. & HAFF, P. (1987). Steady state saltation in air. *Sedimentology*, **34**, 289–299. 14

VAN DIJK, P., ARENS, S. & VAN BOXEL, J. (1999). Aeolian processes across transverse dunes. ii: modelling the sediment transport and profile development. *Earth Surface Processes and Landforms*, **24**, 319–333. 17, 18

REFERENCES

WENG, W., HUNT, J., CARRUTHERS, D., WARREN, A., WIGGS, G., LIVINGSTONE, I. & CASTRO, I. (1991). Air flow and sand transport over sand-dunes. *Acta Mechanica*, **Suppl. 2**, 1–22. 18, 44

WERNER, B. (1995). Eolian dunes: computer simulations and attractor interpretation. *Geology*, **23**, 1107. 17, 19

WERNER, B. & HAFF, P. (1988). The impact process in aeolian saltation: two-dimensional simulations. *Sedimentology*, **35**, 189–196. 14

WERNER, B. & KOCUREK, G. (1997). Bed-form dynamics: Does the tail wag the dog? *Geology*, **25**, 771. 19

WERNER, B. & KOCUREK, G. (1999). Bedform spacing from defect dynamics. *Geology*, **27**, 727. 19

WIGGS, G. (2001). Desert dune processes and dynamics. *Progress in physical geography*, **25**, 53. 18

WIGGS, G.F.S., LIVINGSTONE, I. & WARREN, A. (1996). The role of streamline curvature in sand dune dynamics: evidence from field and wind tunnel measurements. *Geomorphology*, **17**, 29 – 46. 18

WILLETTS, B. & RICE, M. (1988). Particle dislodgement from a flat sand bed by wind. *Earth Surface Processes and Landforms*, **13**, 717–728. 14, 20, 59, 60, 61, 89, 91, 92

WIPPERMANN, F. & GROSS, G. (1986). The wind-induced shaping and migration of an isolated dune: a numerical experiment. *Boundary-Layer Meteorology*, **36**, 319–334. 17, 18

ZEMAN, O. & JENSEN, N. (1987). Modification of turbulence characteristics in flow over hills. *Quarterly Journal of the Royal Meteorological Society*, **113**, 55–80. 44

ZEMAN, O. & JENSEN, N. (1988). Progress report on modeling permanent form sand dunes. *Technical Report M-2738, Risø National Laboratory*. 17, 18

ZHANG, D., NARTEAU, C. & ROZIER, O. (2010). Morphodynamics of barchan and transverse dunes using a cellular automaton model. *Journal of Geophysical Research*, **115**, F03041. 19

ZHENG, X., BO, T. & ZHU, W. (2009). A scale-coupled method for simulation of the formation and evolution of aeolian dune field. *International Journal of Nonlinear Sciences and Numerical Simulation*, **10**, 387–396. 19